Politecnico di Milano
Dipartimento di Energia
Doctoral Programme in
Energy and Nuclear Science and Technology

Development of nanostructured rhodium films for diagnostic mirrors employed in nuclear fusion systems

Doctoral Dissertation of:
Andrea Uccello

Supervisors:
Dr. Matteo Passoni, Dr. David Dellasega

Tutor:
Dr. Lelio Luzzi

The Chair of the Doctoral Program:
Prof. Carlo E. Bottani

Year 2014 – Cycle XXVI

Abstract

Plasma diagnostics system will be essential for the success of the nuclear fusion system ITER. It will provide the means to control the nuclear fusion process, together with the protection of the machine. Many diagnostics will exploit the use of the thermonuclear plasma light which will reach the measurement apparatuses by complex mirrors labyrinths. The first elements of these diagnostics will be metallic mirrors called "First Mirrors" (FMs). Among the main effects of ITER extreme environment on FMs, erosion by energetic particles coming from the plasma and re-deposition of sputtered ITER chamber material transported in the plasma onto their surface could lead to a dramatic decrease of FMs specular reflectivity, thus compromising the operation of the entire diagnostics. One of the principal technological solutions for ITER FMs consists in high reflective rhodium (Rh) coatings deposited on suitable substrates. This Ph.D thesis had a twofold goal. Firstly, the production of Rh coatings for ITER FMs by means of Pulsed Laser Deposition (PLD) was considered. By suitably changing the process parameters, PLD allows morphology and nanostructure control of the growing film. This peculiar feature could in principle determine a potential improvement of Rh films behaviour under ITER plasma erosion. The second objective of this Ph.D was focused on a first study of the laser cleaning technique as a potential method to mitigate ITER FMs re-deposition. The main goal was to develop a novel approach to the process of Rh films production-contamination-cleaning, in which the same laser system is exploited to experimentally investigate this topic with laboratory-scale facilities.

Premessa

Le diagnostiche di plasma saranno essenziali per il successo del dispositivo a fusione nucleare ITER. Tali sistemi dovranno garantire sia il controllo del processo di fusione nucleare che la sicurezza dell'intera macchina. Molte diagnostiche utilizzeranno la luce proveniente dal plasma che verrà trasmessa agli strumenti di analisi tramite complessi labirinti di specchi. I primi elementi saranno specchi metallici, chiamati "First Mirrors" (FMs). Tra i principali effetti dell'ambiente estremo di ITER sui FMs, l'erosione da parte delle particelle provenienti dal plasma e la ri-deposizione sulla loro superficie del materiale eroso dalla camera di ITER, potrebbero determinare un netta decrescita della riflettività dei FMs, compromettendo il funzionamento delle diagnostiche. Una delle principali soluzioni per la produzione di FMs consiste nella deposizione di film di rodio (Rh) su opportuni substrati. Questa tesi ha un duplice obiettivo. Innanzitutto è stata affrontata la produzione di rivestimenti in Rh altamente riflettenti per FMs tramite Pulsed Laser Deposition (PLD). Modificando opportunamente i parametri di processo, la PLD permette di controllare la morfologia e la nanostruttura del film depositato. Questa caratteristica peculiare potrebbe migliorare il comportamento dei film di Rh erosi dal plasma di ITER. Il secondo obiettivo di questo Dottorato consiste nello studio della tecnica del laser cleaning come metodo per contrastare il fenomeno della ri-deposizione sui FMs. In particolare, è stato sviluppato un approccio innovativo al processo di produzione-contaminazione-pulizia di film di Rh, in cui lo stesso laser viene impiegato per investigare sperimentalmente questa tematica in ambito di laboratorio.

Contents

Introduction

Nuclear fusion constitutes a potential and attractive alternative to the resources exploited up to now to meet human energy requirements in the future energy scenario. It owns the potential capability to produce energy on a large scale, using largely available fuels and releasing no carbon dioxide or other greenhouse gases. The fundamental idea driving the research in nuclear fusion is to produce on earth what makes the stars shine. Basically, nuclear fusion is the process by which 2 nuclei join together to form a larger nucleus. This reaction is accompanied by a release of other particles and great amounts of kinetic energy, according to the Einstein equivalence between mass and energy. However, a substantial energy barrier, arising from the mutual Coulomb repulsion between the reactant positively charged nuclei, needs to be overcome in order to make nuclear fusion possible. The most accessible fusion reactions occur among isotopes of hydrogen. Indeed they only have one single positive charge, thus reducing the height of the Coulomb barrier. In particular, thanks to its favourable physical features, the first generation of nuclear fusion power plants foresees the exploitation of the deuterium tritium reaction. To overcome the repulsive force between deuterium (D) and tritium (T) nuclei, it is necessary to supply them with a sufficient amount of kinetic energy, at least on the order of keV. Energetic particles can be obtained by heating the D-T fuel until temperatures at which the thermal agitation of the components is enough to permit a sufficient number of D-T nuclear fusion reactions to release net available energy while balancing at the same time energy loss in the system. The required tem-

peratures are extremely high, on the order of tens-hundreds of millions K. At these conditions, atoms and molecules are completely ionized into nuclei and electrons, thus reaching the plasma state. In order to achieve a net energy gain from nuclear fusion reactions, it is necessary to maintain the required conditions for sufficiently long times, to effectively confine the plasma. Since plasma is constituted by electrically charged particles, it is capable to interact with external electromagnetic fields. One potential solution to confine the thermonuclear plasma is thus to use suitable magnetic fields. In this frame, the so-called tokamak configuration is, among several types of magnetic confinement devices, the most-researched candidate for producing controlled thermonuclear fusion power. The concept was invented in the 1950s by Soviet physicists Igor Tamm and Andrei Sakharov, inspired by an original idea of Oleg Lavrentiev [1]. The word tokamak has therefore Russian origin: it stands for *to*roidalny *ka*mera *mak*ina, due to its peculiar toroidal geometry. The most advanced tokamak experiment is ITER ("the way" in Latin) [2], currently under construction. It aims to make a major step in the long-awaited transition from experimental studies of plasma physics to full-scale electricity-producing fusion power plants.

The physical, engineering and technological complexity of the ITER project, makes it one of the greatest challenges in human history. Plasma diagnostics will be essential for its success. They will play the crucial role of controlling the nuclear fusion process, ensuring at the same time the integrity of the ITER toroidal chamber. Since the extreme temperatures in ITER ($\sim 10^8$ K) will make a direct contact between the thermonuclear plasma and material probes almost impossible, many diagnostics (about 30) will involve the use of the electromagnetic radiation emitted, reflected or diffused by the thermonuclear plasma, which will reach the measurement apparatuses by complex mirrors labyrinths [3]. Some of their most critical components will be the mirrors placed on the first-wall of the ITER toroidal chamber, called First Mirrors (FMs). They will endure severe conditions in terms of intense thermal loads (up to 500 kW/m^2), strong radiation fields (up to 2×10^3 Gy/s) and high particles fluxes (neutron flux up to 3×10^{18} neutrons m^{-2} s^{-1}) [4]. Among the effects of this harsh environment on FMs, erosion by energetic particles coming from the hot plasma and re-deposition of sputtered material transported from the first-wall onto their surface constitute topical issues. These phenomena could lead indeed to a dramatic decrease of FMs specular reflectivity, posing a serious threat on the operation of the entire diagnostics [5].

One of the principal materials investigated for ITER FMs production is

rhodium (Rh), thanks to its high reflectivity in a wide wavelength range, acceptable sputtering yield and melting point (1966 °C) [6]. The high cost of Rh as a raw material, together with the potential interest towards FMs solutions based on thin film technology, suggests its use as a high reflective coating deposited on a suitable substrate.

The thesis subject of this Ph.D in Energy and Nuclear Science and Technology (STEN) at Politecnico di Milano (Polimi) deals with the study and the development of nanostructured rhodium films functional for ITER FMs. This Ph.D work was mainly experimental. The emphasis was put on basic material science aspects in order to establish new useful knowledge for the development of suitable solutions for realistic mirror devices. This Ph.D project had a twofold goal. Firstly, the production of Rh coatings functional for FMs by means of Pulsed Laser Deposition (PLD) was addressed. By suitably changing the process parameters, PLD allows morphology and nanostructure control of the growing film in a peculiar manner with respect to the other deposition techniques, like electrodeposition and magnetron sputtering. This feature could in principle determine a potential improvement of Rh films response to the phenomenon of ITER plasma erosion. The second objective of this Ph.D thesis consisted in a first study of the laser cleaning technique as a potential method to mitigate the re-deposition of first-wall eroded materials onto FMs. The main goal was to develop a novel approach to the process of Rh films production-contamination-cleaning, in which the same laser system is exploited to experimentally investigate ITER FMs re-deposition topic with laboratory-scale facilities.

The present dissertation has been organized following the above described logical path. A brief description of the contents for each chapter is given below.

Part I: First mirrors for nuclear fusion diagnostic systems: state of the art

Chapter 1 In this first chapter of the thesis the general scientific background is reported. After an introduction on the basic principles of nuclear fusion, the attention is focused on the different methods currently under investigation to confine the nuclear fusion energy. The tokamak solution is afterwards described and the ITER device is finally introduced.

Chapter 2 An up-to-date state of the art of ITER diagnostics and first

mirrors is here reported. First of all, a survey of some of the main diagnostics foreseen to be installed in ITER is reported. As an example, the Thomson scattering core light detection and ranging diagnostic is discussed in detail, with the twofold aim of giving further insight on the big challenges that the ITER community has still to face and also to introduce the specific topic of this Ph.D thesis: First Mirrors (FMs). The main open issues of erosion and re-deposition associated to these components are then carefully described. Finally, the specific objectives of this Ph.D work, together with the experimental methods used in order to accomplish them, are presented.

Part II: Production and investigation of rhodium films

Chapter 3 The advances achieved in this thesis on the deposition by Pulsed Laser Deposition (PLD) of rhodium (Rh) films with suitable properties for ITER first mirrors production are here described. In particular, the technological solutions employed to overcome the main intrinsic PLD drawbacks, such as the achievable dimensions, mechanical behaviour of films and the quality of their surface required to obtain the highest specular reflectivity, are discussed.

Chapter 4 In order to demonstrate the effectiveness of PLD towards the improvement of Rh films response to ITER plasma erosion, this chapter reports an experimental investigation of the performance of Rh films exposed to a laboratory pure deuterium plasma with qualifying features relative to the ITER peripheral plasma facing first mirrors. This campaign was developed at the Physics Department of Basel University in collaboration with the Nanolino group.

Part III: Laser cleaning from "tokamak-like" contaminants of rhodium films

Chapter 5 Here a novel approach to the process of Rh films production-contamination-cleaning, in which the same laser system is employed to investigate ITER FMs re-deposition issues with laboratory-scale facilities, is developed. Particular emphasis is given to the production of "tokamak-like" contaminants by PLD. Afterwards, the preliminary attempts of applying the laser cleaning technique with the goal of removing PLD re-deposits from PLD Rh films thus restoring their initial optical properties, are reported.

Chapter 6 The main results obtained during a three months period at the Joint European Torus (JET) tokamak, located in Culham (Oxfordshire, United Kingdom), in the frame of post-mortem characterization of JET first-wall components, or tiles, extracted after 2011-2012 experimental campaign are discussed here. The activity fits to the subject of this Ph.D thesis in the perspective of acquiring realistic information about tokamak re-deposits with the potential goal of producing them faithfully in laboratory by PLD. Considering the main post-mortem characterization techniques, the development and application of an interpretative tool (i.e. MatLab routine) for tiles profiling measurements are deeply described.

The original contents of this PhD thesis have led to the publication of the following peer-reviewed papers, ordered by year:

- A. Uccello, D. Dellasega, S. Perissinotto, N. Lecis, M. Passoni. Nanostructured rhodium films for advanced mirrors produced by Pulsed Laser Deposition. *Journal of Nuclear Materials*, 432(1-3):261–265, 2013.
- A. Uccello, A. Maffini, D. Dellasega, M. Passoni. Laser cleaning of pulsed laser deposited rhodium films for fusion diagnostic mirrors. *Fusion Engineering and Design*, 88(6-8):1347–1351, 2013.
- A. Uccello, B. Eren, L. Marot, D. Dellasega, A. Maffini, R. Steiner, D. Mathys, E. Meyer, M. Passoni. Deuterium plasma exposure of rhodium films: role of morphology and crystal structure. *Journal of Nuclear Materials*, 446(1-3):106–112, 2014.
- A. Maffini, A. Uccello, et al. Laser cleaning of diagnostic mirrors from tokamak-like carbon contaminants. In preparation.

The subject of this Ph.D thesis was presented by myself in different International Conferences, ordered by year:

- M. Passoni, D. Dellasega, G. Merlo, A. Uccello, G. Grosso, M.C. Ubaldi, C.E. Bottani. Nanostructured Rhodium Films for Advanced Diagnostic Mirrors Produced by Pulsed Laser Deposition. 13th International Workshop on Plasma-Facing Materials and Components

for Fusion Applications & 1st International Conference on Fusion Energy Materials Science (PFMC-13 Workshop / FEMaS-1 Conference), Rosenheim, Germany, 9-13 May 2011. Poster presentation.

- A. Uccello, D. Dellasega, S. Perissinotto, N. Lecis, M. Passoni. Nanostructured Rhodium Films for Advanced Mirrors Produced by Pulsed Laser Deposition. 16th International Conference on Solid Films and Surfaces (icsfs16), Genoa, Italy 1-6 July 2012. Oral presentation.

- A. Uccello, A. Maffini, D. Dellasega, M. Passoni. Laser Cleaning of Pulsed Laser Deposited Rh Films for Fusion Diagnostic Mirrors. 27th Symposium of Fusion Technology (SOFT 2012), Liège, Belgium, 24-28 September 2012. Poster presentation.

- A. Uccello, A. Maffini, D. Dellasega, M. Passoni. Laser Cleaning of Pulsed Laser Deposited Rhodium Films from Tokamak-like Contaminants. The 12th International Conference on Laser Ablation (COLA 2013), Ischia, Italy, 6-11 October 2013. Poster presentation.

The subject of this Ph.D thesis was also presented in other International Conferences, ordered by year:

- M. Passoni, A. Uccello, D. Dellasega, S. Perissinotto, B. Eren, L. Marot, E. Meyer. Nanostructured Rhodium Films for Advanced Mirrors Produced by Pulsed Laser Deposition. 27th Symposium of Fusion Technology (SOFT 2012), Liège, Belgium, 24-28 September 2012. Poster presentation.

- A. Maffini, A. Uccello, D. Dellasega, S. Perissinotto, B. Eren, L. Marot, E. Meyer, M. Passoni. Nanostructured Rhodium Films for Advanced Mirrors Produced by Pulsed Laser Deposition: Erosion and Redeposition Concerns. 14th International Conference on Plasma-Facing Materials and Components for Fusion Applications (PFMC-14), Juelich, Germany, 13-17 May, 2013. Poster presentation.

- D. Dellasega, A. Uccello, A. Pezzoli, A. Maffini, C. Conti, M. Passoni. Permeation and Erosion Properties of Amorphous-like Metallic Films Deposited by Pulsed Laser Deposition. The 12th International Conference on Laser Ablation (COLA 2013), Ischia, Italy, 6-11 October 2013. Poster presentation.

Part I

First mirrors for nuclear fusion diagnostic systems: state of the art

1 Magnetic nuclear fusion: a short introduction

In this chapter the general topic under which this thesis is developed, the magnetic confinement nuclear fusion, will be introduced. In section 1.1 the basic principles of nuclear fusion will be described. Secondly, in section 1.2 a brief analysis of the advantages and issues of the most studied nuclear fusion reactions from the energy production point of view will be reported. The physical conditions for generating net energy from nuclear fusion reactions, together with the different methods currently under investigation to confine the nuclear fusion energy in order to exploit it, will be presented in section 1.3. The magnetic confinement and the different implementation approaches will be shown in section 1.4. Among them, the tokamak solution will be more deeply described in section 1.5. Then, the main features and the storyline of the currently building world's largest tokamak ITER will be reported in section 1.6. Particular emphasis will be given to the different components of the ITER first-wall and to the materials selected for producing them.

1.1 Basic principles

The release of energy by means of nuclear reactions could be achieved following two different ways: the fusion of two light nuclei or the fission of two heavy nuclei. Figure 1.1 shows the graph of the binding energy per nucleon (expressed in MeV) as a function of the mass number (A). For light nuclei, it increases with A: the aggregation of two light nuclei determines

the formation of a more stable nucleus, together with the release of a significant amount of energy. The situation for a heavy nucleus is dual: the binding energy per nucleon increases lowering A. The disruption of a heavy nucleus brings to two lighter nuclei and again a relevant quantity of energy.

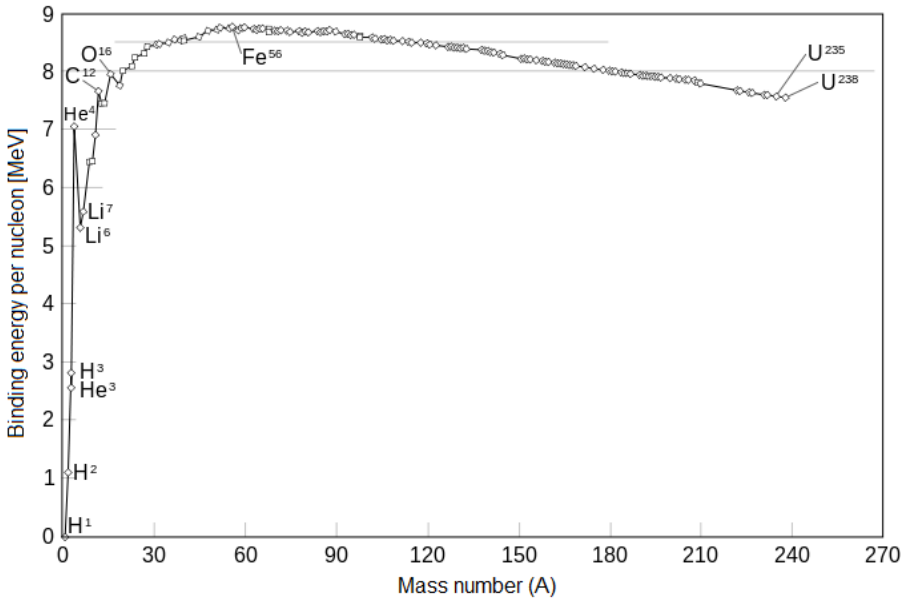

Figure 1.1: *Binding energy per nucleon (MeV) as a function of the mass number (A).*

As a source of energy, fusion presents evident advantages with respect to fission: light nuclei are abundant and largely available in nature, the energy per nucleon released is 5-6 MeV on average against 0.8 MeV for the usual fission reaction of ^{235}U, the reaction products are in general nonradioactive nuclei. Nonetheless, fusion has a remarkable drawback: to establish a fusion reaction, the two reactant nuclei, which are electrically charged, need to overcome the repulsive Coulomb force in order to approach each other to a distance on the order of 10^{-15} m, i.e. the nuclear force range. Since a fission reaction is triggered by neutrons, it does not present this relevant concern.

The researches on the topic of nuclear fusion widely spread after the second world war, mainly because of its potential use for military purposes (hydrogen bomb, 1952). However, the scientific community was soon aware of the outstanding engineering and technological issues underneath the project of a full-scale electricity-producing fusion reactor plant [7].

1.2 Fusion reactions

Over a hundred of nuclear fusion reactions between light nuclei has been studied so far. The simplest one is the reaction between two hydrogen nuclei, which however cannot be realized on the earth. It requires indeed the development of a complex reaction chain that occurs on a long temporal scale. Moreover, this chain of exothermal reactions takes place in the sun and in the other stars, permitting them to shine. The most interesting nuclear reactions for application on the earth, involve the heavier isotopes of hydrogen: deuterium (D) and tritium (T). Deuterium is a stable isotope contained in water with an abundance of 0.015%: it is therefore nearly inexhaustible. On the other hand, tritium is unstable and it is therefore necessary to be artificially produced. The principal fusion reactions which involve deuterium and/or tritium are:

$$\begin{aligned} \mathrm{D} + \mathrm{D} &\rightarrow \mathrm{T} + {}^{1}\mathrm{H} + 4.03\ \mathrm{MeV} \\ \mathrm{D} + \mathrm{D} &\rightarrow {}^{3}\mathrm{He} + \mathrm{n} + 3.27\ \mathrm{MeV} \\ \mathrm{D} + {}^{3}\mathrm{He} &\rightarrow {}^{4}\mathrm{He} + {}^{1}\mathrm{H} + 18.3\ \mathrm{MeV} \\ \mathrm{D} + \mathrm{T} &\rightarrow {}^{4}\mathrm{He} + \mathrm{n} + 17.6\ \mathrm{MeV} \end{aligned}$$

It is now interesting to briefly examine the advantages and drawbacks of each reaction, considering the energy production.

With the aim of highlighting the most relevant parameters of the nuclear fusion process, consider a system constituted by two populations of elements A and B. Indicate with $\mathrm{n_A}$ and $\mathrm{n_B}$ the corresponding number of particles per unit volume and with $\mathrm{n} = \mathrm{n_A} + \mathrm{n_B}$ the total number density. The number of nuclear reactions per unit volume and time is $\mathrm{n_A n_B} \sigma \mathrm{v}$, where σ is the total cross section of nuclear fusion among elements A and B, and v is the relative velocity between the reactant particles. For the sake of simplicity, suppose that $\mathrm{n_A} = \mathrm{n_B} = \mathrm{n}/2$. Labeling with $\mathrm{E_{AB}}$ the energy released by the reaction, the power per unit volume achieved from the nuclear process is

$$\mathrm{P_f} = \frac{\mathrm{n}^2}{4} \overline{\sigma \mathrm{v}} \mathrm{E_{AB}} \tag{1.1}$$

where the average $\overline{\sigma \mathrm{v}}$ is calculated over the velocity distribution of the particles. This expression points out that the energy released by the reaction, $\mathrm{E_{AB}}$, and the reaction rate, $\overline{\sigma \mathrm{v}}$, are the two physical parameters to be considered in order to evaluate the goodness of a nuclear fusion reaction from the energy production point of view. In particular, the quantity $\overline{\sigma \mathrm{v}}$ for a Maxwell velocity distribution and the nuclear fusion reactions of interest is shown in figure 1.2.

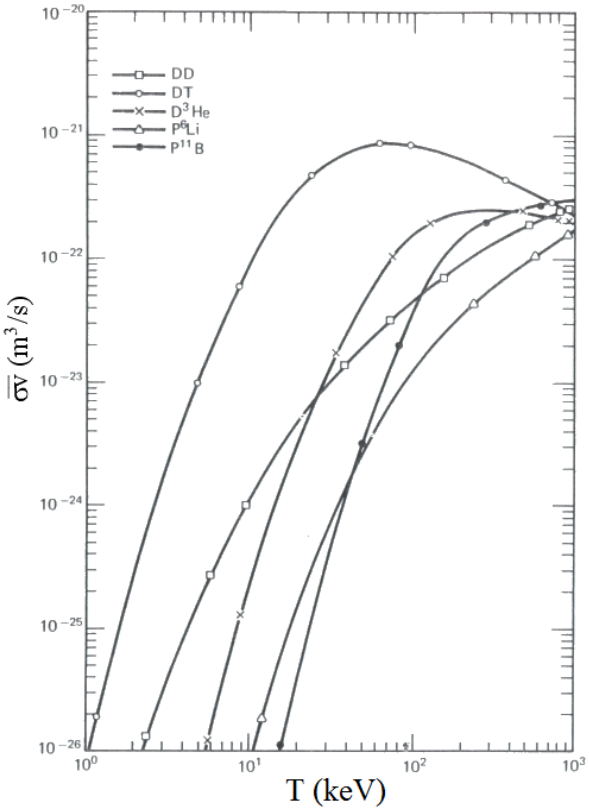

Figure 1.2: *Reaction rate $\overline{\sigma v}$, averaged on a Maxwell velocity distribution for the reactant particles, as a function of temperature T, for the nuclear fusion reactions of interest.*

The first two reactions (D-D reactions) involve only deuterium nuclei thus exhibiting the striking advantage of employing an element nonradioactive, abundant, and easily achievable by means of isotopic separation and successive electrolysis of the obtained heavy water. On the other hand, the release of energy from both the reaction channels (which are approximately equally probable) and the reaction rate are lower than those of the other nuclear fusion reactions. The realization of a nuclear fusion power plant based on D-D reactions is therefore more complex.

The reaction D-^{3}He shows some favourable properties: the release of energy from a reaction is significant and moreover there are no neutrons among the reaction products (it is otherwise necessary to minimize the D-D reactions that could also verify). The latter would avoid the activation concern and the structural damage induced by neutron bombardment on

the reactor materials. Furthermore, the presence of electrically charged products rises the possibility of developing systems for the direct conversion of nuclear fusion energy into electric energy, without employing thermodynamic cycles. However, even in this case, D-^{3}He is characterized by a low reaction rate. Moreover, the ^{3}He isotope is extremely rare on the earth (isotopic abundance 0.000137%).

The D-T reaction is characterized by a significant reaction rate, together with a great release of energy. The energy gain coming from a single reaction is the highest among all the potential solutions considered so far. The D-T reaction thus constitutes the starting point for the nuclear fusion researches. Nonetheless, it presents some important issues. The energy produced by the fusion reaction, 17.6 MeV, is released as kinetic energy of the reaction products. The alpha particle and the neutron have a kinetic energy of 3.5 MeV and 14.1 MeV, respectively. The fast neutrons of 14.1 MeV induce serious damage and activate the structural materials which need to be frequently substituted by remote handling. Furthermore, tritium is a radioactive element ($T_{1/2}$ = 12.33 y) and it is artificially produced. The main mechanism exploited to produce T is the neutron absorption by one of the two stable lithium (Li) isotopes, according to the following reactions

$$^6\mathrm{Li} + \mathrm{n} \rightarrow \mathrm{T} + {}^4\mathrm{He} + 4.8 \text{ MeV}$$
$$^7\mathrm{Li} + \mathrm{n} \rightarrow \mathrm{T} + {}^4\mathrm{He} - 2.5 \text{ MeV}$$

The former (latter) is exothermic (endothermic) and it is most probable for thermal (fast) neutrons. The neutron necessary for these reactions could come from the D-T reaction: it is possible, in principle, to establish a regenerative cycle into the nuclear fusion device (similar to that used by the fast nuclear fission reactors).

Thanks to its favourable physical features, the first generation of nuclear fusion power plants foresees the exploitation of the D-T reaction. The knowledge acquired after the realization of this class of reactors should bring to the development of D-D power plants. Due to the low values for the two physical parameters E_{AB} and $\overline{\sigma v}$, the underneath technology will be clearly more complex than that of the D-T reactors. However, this solution is very attractive and promising as D-D power plants would significantly reduce tritium and radioactive waste issues.

As previously observed, since nuclear fusion reactions involve electrically charged particles, it is necessary to supply them with a sufficient amount of kinetic energy, at least on the order of keV, in order to overcome the repulsive Coulomb barrier. Energetic particles can be obtained

by heating the system until temperatures at which the thermal agitation of the components is enough to permit nuclear fusion reactions. The required temperatures are very high, on the order of some millions of Kelvin. At these conditions, atoms and molecules are completely ionized into nuclei and electrons thus reaching the fourth state of the matter: the plasma state. Since the constituents of this system are electrically charged, they interact in a complex way through Coulomb collisions and collective modes by means of auto-generated electromagnetic fields. Moreover, a plasma can interact with external electric end magnetic fields.

The development of a nuclear fusion power plant needs to fulfill two main goals. Firstly, it is necessary to create a hot plasma and to maintain it for a sufficient time to achieve a net energy gain. Secondly, the actual power plant, that is a system able to convert thermal energy into cost-effective electric energy, needs to be realized. As an example, the functional scheme of a nuclear fusion power plant based on the D-T reaction is reported in figure 1.3.

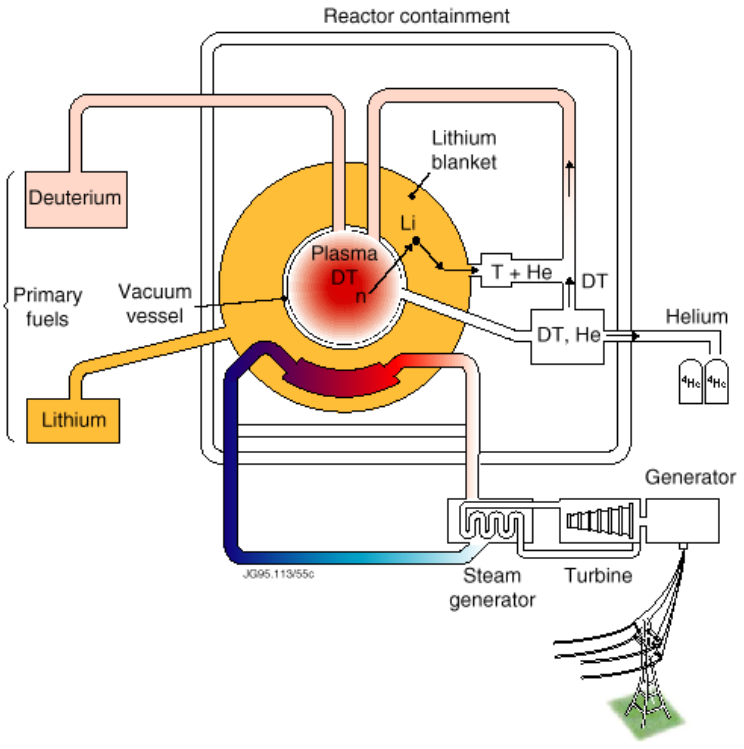

Figure 1.3: *Functional scheme of a D-T nuclear power plant.*

1.3 Thermonuclear plasma confinement and ignition

In order to create and maintain the thermonuclear plasma, it is necessary that the thermal energy associated to the fuel particles is enough to give rise to nuclear fusion reactions with a net energy gain. This aspect constitutes the main drawback of the nuclear fusion research. First of all, the plasma needs to be heated up to temperatures on the order of millions of Kelvin. It is afterwards essential to confine the plasma in these conditions, avoiding its expansion due to the thermal energy, which would be lost too rapidly. Considering the stars, this confinement is realized by the huge gravitational field. On the earth, this solution is not accessible and other confinement mechanisms are required. The confinement issue is made more complex by a great variety of plasma instabilities resulting from the electromagnetic interaction between its constituents, which could bring to the plasma switching off before the fulfillment of the nuclear fusion conditions. Finally, with the aim of obtaining a net energy gain, it is necessary to take into account the significant plasma energy loss due to radiation emission. As a matter of fact, plasma electrons waste their energy emitting Bremsstrahlung radiation as a consequence of their continuous acceleration and deceleration due to interaction with ions. At the typical plasma temperatures, the Bremsstrahlung radiation is mainly constituted by X-rays which are not recovered. However the total power per unit volume of the nuclear fusion reactions rises with the temperature faster than the power per unit volume lost for Bremsstrahlung emission. The ideal ignition temperature is the temperature at which the two powers per unit volume equalize. As an example, the ideal ignition temperature for the D-T reaction is 4.4 keV (about 34 millions of Kelvin).

To realize a favourable energetic system, the achievement of the ideal ignition temperature constitutes only a necessary condition. Beyond the Bremsstrahlung emission, thermal mechanisms (e.g. particles diffusion and thermal conduction) as well as the fraction of the nuclear fusion energy transported by neutrons away form the plasma, contribute indeed to the plasma energy losses.

In order to reach the ignition condition, it is mandatory to balance the plasma energy losses (due to radiation emission and thermal mechanisms) with a portion of the nuclear fusion energy. If the system confinement properties (i.e. confinement time, plasma density and temperature) are not enough to achieve this regime, it is necessary to supply the nuclear fusion process with an external energy source. The equilibrium condition, also called break-even, is reached when the power generated by the nuclear

fusion reactions equalizes the input power. This constitutes the requisite to be satisfied in order to design a null-power reactor. The break-even achievement depends on the particles density, n, of the confined plasma portion and on the energy confinement time, τ_E. The requirements to be fulfilled can be quantified in short by a simple energy balance. Considering the D-T reaction, at temperatures on the order of that of the ideal ignition, this balance can be expressed as follows:

$$n\tau_E > 10^{14} \text{ s/cm}^3 \quad \text{(Lawson's criterion)} \tag{1.2}$$

The final goal of the nuclear fusion research consists in realizing a system at ignition, that is a system in which the fusion process is auto-sustained by a fraction of the nuclear fusion energy transferred to the plasma by the electrically charged products which are capable to interact with it. Once the ignition is reached, it is no more necessary to introduce energy into the system: the plasma energy losses are indeed replaced by a fraction of the energy released by the nuclear fusion reactions. In the case of the D-T reaction, albeit the 14.1 MeV neutrons escape from the system, the power associated to the 3.5 MeV alpha particles can be transferred to the plasma through collisional and collective scattering. The ignition conditions are reached when the power supplied by the alpha particles equalizes the total power losses. Of course, it is necessary to obtain temperatures higher than the ideal ignition temperature and $n\tau_E$ values greater than the Lawson's criterion. Considering again the D-T reaction, the ignition condition requires temperatures on the order of 100 millions of Kelvin and $n\tau_E$ higher than 10^{15} s/cm^3. Introducing the fusion energy gain factor Q:

$$Q = \frac{\text{nuclear fusion power}}{\text{input power}} \tag{1.3}$$

it is possible to express the break-even and ignition conditions as

$$Q \begin{cases} = 1, & \text{break-even} \\ \to \infty, & \text{ignition} \end{cases} \tag{1.4}$$

Because of the high temperatures, the plasma confinement cannot be achieved by material walls. It is mandatory to avoid any contact between thermonuclear plasma and physical surfaces in order to prevent its contamination and energy dissipation through different loss mechanisms (e.g. radiative phenomena and conduction).

Nuclear fusion researches have identified two different approaches for plasma confinement: magnetic confinement and inertial confinement. The

former solution has the aim of confining a low-density plasma (on the order of 10^{14} nuclei/cm^3) on a time lapse on the order of seconds, whereas the latter has the goal to compress the plasma to a very high density (on the order of 10^{24} nuclei/cm^3) in a way that τ_E equalizes the characteristic expansion time associated to the particles inertia (nanoseconds). The physical and technological issues underneath these two processes are really different. However, since the general topic of this thesis is the magnetic confinement fusion, only the basic aspects of this approach will be described in the follows.

1.4 Magnetic confinement

As previously mentioned, the plasma is capable to interact with external electric and magnetic fields. One potential solution thus consists in confining it by suitable electromagnetic fields.

In the case of a plasma in a spatial uniform magnetic field, as that produced by a solenoid or by a system of coils placed along an axis, since the charged particles follow helicoidal trajectories wrapping around the magnetic field lines (cyclotron or Larmor motion), a transversal confinement is achieved, as shown in figure 1.4. However, by means of this approach, particles are freely to move along the axis. Therefore the axial confinement is not achieved.

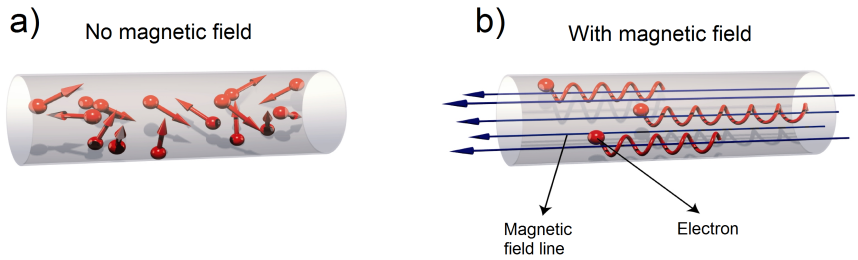

Figure 1.4: *Scheme of free charged particles (a) and with a uniform axial magnetic field (b).*

To obtain the longitudinal confinement, two solutions have been investigated so far. In the former, magnetic field intensity increases at the edges of the system (figure 1.5a). Particles are subjected to the magnetic mirror phenomenon: due to the conservation of particles energy and magnetic momentum, a fraction of particles, once they reach the system boundary, is forced to invert its motion towards the low magnetic field zones. This

approach brought to the development of the so-called mirror machines. However, the concerns related to an incomplete particles confinement and to the complexity of the magnetic field configuration, mandatory to avoid magnetohydrodynamic instabilities, revealed hardly solvable.

A completely different approach consists of closing the solenoid: the plasma has a torus shape being subjected to a toroidal magnetic field created by the coils in which a poloidal current flows (figure 1.5b). The

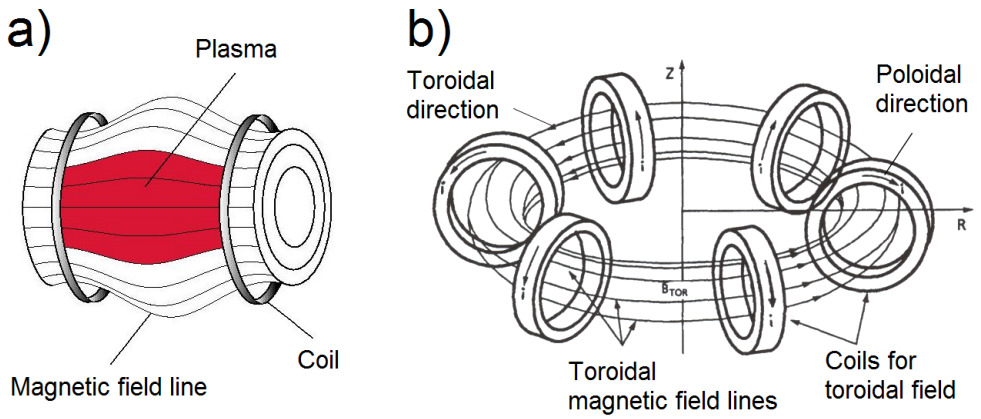

Figure 1.5: *Mirror machine configuration (a) and toroidal configuration (b).*

magnetic field is curved and no more uniform as a consequence of the Ampére's law. With this configuration, the particles own the usual Larmor motion around the magnetic field lines plus a drift motion transverse to them which brings to particles loss. It is thus necessary to introduce a poloidal magnetic field component. In this way the magnetic field lines helicoidally wrap the torus (figure 1.6), generating closed magnetic surfaces and the total particles motion makes the confinement achievable. The poloidal field could be produced by a toroidal current which flows along the plasma: the nuclear fusion device which exploits this solution is called *tokamak*. This world has a Russian origin (from *to*roidalny *ka*mera *mak*ina) since the first machine was developed in the Soviet Union at the end of the fifties. Another approach to generate the poloidal magnetic field component is through suitable helicoidal coils, as it happens in the *Stellarator*.

Since this thesis deals with tokamak diagnostics the next section will give a brief description of tokamak main components and issues.

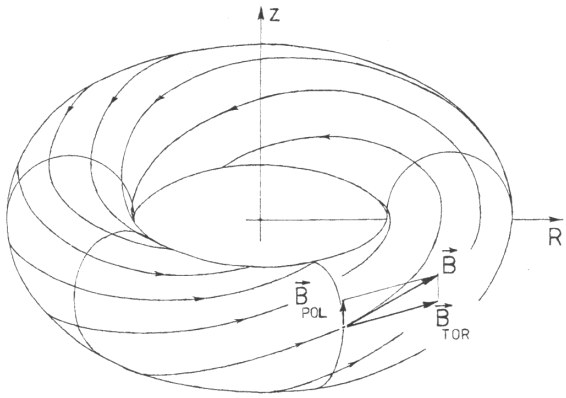

Figure 1.6: *Helicoidal magnetic field resulted from the composition of the toroidal and poloidal magnetic fields.*

1.5 The tokamak configuration

Tokamak is the most studied nuclear fusion device which gives the most promising results. First of all, the general tokamak structure foresees the toroidal vacuum chamber in which the nuclear fusion fuel is injected. The wall which directly faces the thermonuclear plasma, also called first-wall, is one of the most critical tokamak components (figure 1.7). It endures an

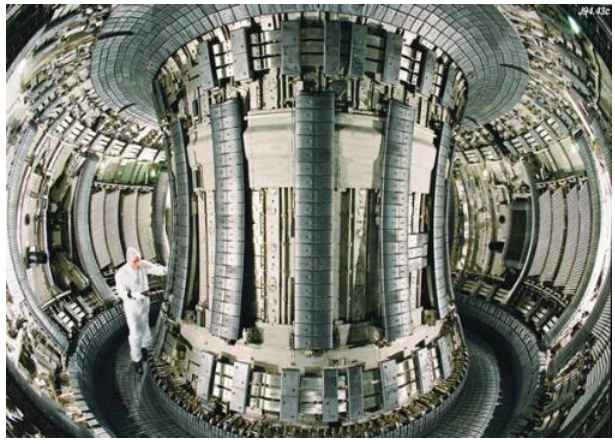

Figure 1.7: *Joint European Torus (JET, Culham, Oxfordshire, United Kingdom) tokamak first-wall before 2010 (carbon first-wall).*

intense radiation flux coming from the plasma which comprises of: electromagnetic radiation, particles escaped from the magnetic confinement

(eroding the first-wall through the sputtering phenomenon) and especially the 14.1 MeV neutron flux. The maximum bearable heat flux determines a superior limit to the fusion power per unit volume and thus to the maximum plasma density. By virtue of the Lawson's criterion (expression 1.2) an inferior limit to the energy confinement time τ_E is set. From the operational point of view, it is fundamental that the possible interaction between the plasma and the first-wall does not introduce a significant amount of impurity nuclei with a high atomic number (Z) in the plasma itself, which would bring to an unacceptable power loss due to radiation emission (Bremsstrahlung radiation significantly increases with the plasma effective nuclear charge). Accordingly, first-wall materials should be low-Z materials capable to withstand to the tokamak harsh environment, thus minimizing their substitution (this is a really complex operation which requires remote handling). Beryllium and graphite are two of the most studied tokamak first-wall materials. The crucial issue of the choice of first-wall materials, including the several diagnostics for plasma monitoring, represents a fundamental part of this thesis and it will be widely described in the next chapter.

Tokamak intense confinement magnetic field is produced by a complex set of coils and transformers. Poloidal coils are exploited to generate the toroidal magnetic field. They should be able to create high magnetic fields, from some teslas to 12-13 teslas. Currents on the order of some megaamperes are thus necessary. To avoid significant energy losses for Joule effect, superconductive coils cooled with liquid helium are employed. In order to prevent poloidal coils damage and heating over the critical temperature of the superconductive material exploited, it is mandatory to protect them with a suitable screens system.

It is evident that tokamak operation requires to simultaneously reach the highest (10^8 K) and lowest (some Kelvin) temperatures ever achieved by man, in a range of some meters. Beyond the design and realization problems, also the thermal insulation of the different tokamak regions has therefore a high-priority.

With the goal of producing the plasma current for the generation of the poloidal magnetic field, tokamak technology foresees a system of transformers, usually with an iron core. The functional principle is straightforward: the toroidal chamber, together with the thermonuclear plasma, is concatenated with the flux produced by the transformer primary winding. The flux variation induces a current in the plasma, which thus constitutes the transformer secondary winding. For this reason, tokamak is an intrinsic pulsed device. Once the gaseous fuel is injected into the toroidal

chamber, this transformers system produces a discharge in order to generate the plasma. Tokamak magnetic field inhomogeneities determine the expansion of the plasma spire. To control the plasma configuration, tokamaks foresee another coils system responsible for the generation of a vertical magnetic field which couples with the plasma current, thus producing a Lorentz force directed towards the axis which opposes to the plasma expansion. The main tokamak coils systems (except for those of the vertical magnetic field), currents and magnetic fields are represented in figure 1.8.

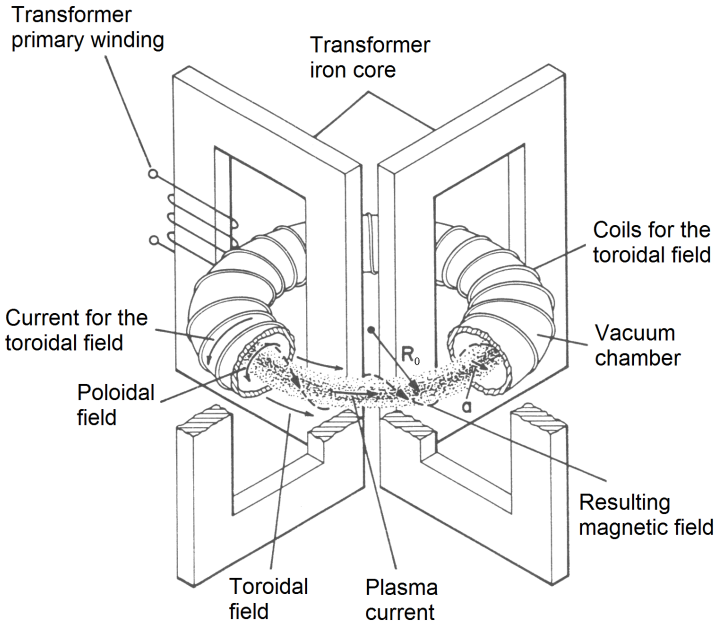

Figure 1.8: *Scheme of the tokamak coils system for the confinement helicoidal magnetic field.*

The magnetic field ability to confine the plasma thermal energy is expressed by means of the parameter β which is the ratio between the plasma kinetic pressure, p, and the magnetic pressure, p_{mag}. The former is defined by the relation

$$p = nT \tag{1.5}$$

Considering 10^{15} cm^{-3} and 10 keV as typical ignition values for n and T, p is equal to 16 bar. The magnetic pressure is given by the symmetric part of the Maxwell magnetic stress tensor which describes the electrodynamic force acting on the plasma, generated by the coupling between the

magnetic field and the plasma current

$$p_{mag} = \frac{B^2}{8\pi} \quad \text{in Gaussian units} \tag{1.6}$$

The parameter β is therefore

$$\beta = \frac{8\pi nT}{B^2} \tag{1.7}$$

which is comprised between 0 (non-confinement) and 1 (for $\beta > 1$, p_{mag} is not able to equalize the plasma kinetic pressure and it is impossible to obtain the confinement). The goal is to achieve β values as close as possible to 1 in order to efficiently confine the plasma and to reduce the dimension of the overall system. However, tokamak magnetohydrodynamic stability analysis shows that low β values ($\sim 10^{-2}$) correspond to more stable equilibrium configurations. Theoretical investigations have revealed high β (~ 0.2) stable regimes achievable shaping the plasma in a way that its elongation and triangularity are different from zero (figures 1.9a,b). In this cases, tokamak poloidal section is elliptical and/or has a D-shape (figure 1.9c). It is clear that tokamaks foresee further coils systems which generate additional magnetic fields for plasma shaping and for controlling plasma equilibrium and magnetohydrodynamic stability.

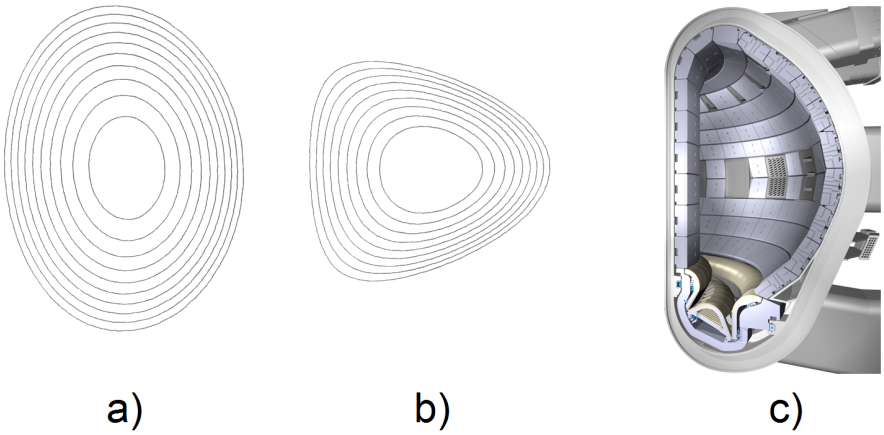

Figure 1.9: *Tokamak poloidal section with elongation different from zero (a) and triangularity different from zero (b). Typical tokamaks D-shape with finite elongation and triangularity (c) [2].*

Beyond the poloidal magnetic field generation, the toroidal plasma current in a tokamak is also responsible for its heating, which occurs by Joule

effect. However, the Ohmic heating presents an intrinsic issue: plasma electric resistivity reduces increasing the temperature. Plasma behaviour, during heating, actually tends to that of an ideal conductor. In order to achieve thermonuclear plasma conditions, it is therefore necessary to exploit further heating mechanisms. Two techniques have been investigated so far. In the former, heating is obtained through the non-collisional absorption of radio-frequency electromagnetic waves generated by suitable sources. The dispersive behaviour of the plasma makes the resonant coupling with electromagnetic waves at different characteristic frequencies possible. The different most-studied solutions are: the Electron Cyclotron Radio-frequency Heating (ECRH, which exploits the electron cyclotron frequency), the Ion Cyclotron Radio-frequency Heating (ICRH, which exploits the ion cyclotron frequency) and the Lower Hybrid Radio-frequency Heating (LHRH, which exploits the so-called inferior hybrid frequency). The other mechanism exploited to heat the plasma foresees the injection of high-energy nonionized atoms (neutrals), of the same plasma elements, into the plasma. The name of this technique is Neutral Beam Injection (NBI). The fast neutrals are generated from a beam which is ionized, accelerated in a vacuum chamber and again neutralized. Once the neutrals reach the plasma, they make charge exchange reactions with the plasma nuclei, thus introducing fast ions into the system. By means of these two approaches, it is possible to achieve heating powers on the order of several megawatts.

As described in section 1.4, tokamak thermonuclear plasma, due to its toroidal configuration, is confined in closed magnetic surfaces, whose shape is determined by the tokamak magnetic fields structure. The last magnetic surface is also called Last Closed Flux Surface (LCFS) [8]. It plays a crucial role in the frame of the interaction between the plasma and the first-wall components. The LCFS permits to distinguish two plasma regions: the hot core, in which the nuclear fusion reactions happen, and the plasma boundary, characterized by a lower temperature and density. LCFS position and shape can be also controlled adopting specific tools during tokamak chamber design phase. The two most investigated solutions are the limiter and the divertor. Beyond the effect on the global performance of the confinement, they permit to control plasma-material interactions in a tokamak.

The limiter is the simplest and most intuitive way to guarantee the protection of the tokamak vacuum chamber towards the plasma interaction. It consists in a material ring in direct contact with the plasma. The interaction is thus localized onto a suitably designed component which

could be eventually changed. Two limiter types have been used so far. The former, also called poloidal limiter (figure 1.10a), is an annular component which wraps the plasma, ensuring the protection of the first-wall. The latter, known as toroidal limiter (figure 1.10b), is a toroidal ring at half-height of the tokamak chamber which protrudes towards the plasma.

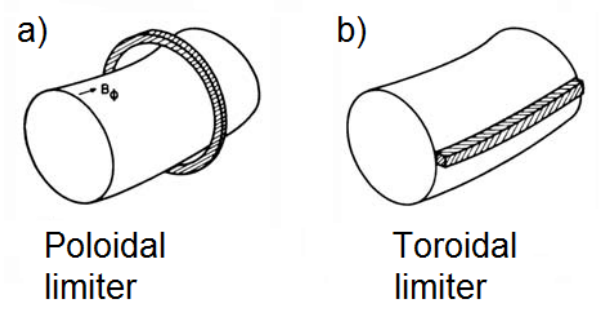

Figure 1.10: *Poloidal (a) and toroidal (b) limiters [8].*

With the aim of further reducing the first-wall issues and improving the performance of the machine, another component has been investigated. It is called divertor and it is capable of removing the plasma impurity and controlling the exhausted low-energy helium population (helium ash), produced by the D-T reactions. As just mentioned, the removal of these elements with Z higher than that of the hydrogen isotopes is necessary to reduce the energy loss due to Bremsstrahlung emission, thus facilitating the maintenance of the ignition conditions. The divertor functional principle is based on the production, in correspondence of the plasma boundary, of one or more regions with open magnetic field force lines directed towards specific divertor components, know as divertor targets. The external part of the plasma, which contains the lower energy particles and the major fraction of impurities, is thus divided from the internal hot region and is guided to the divertor targets where extractor devices can be introduced. The magnetic field structure for the divertor configuration is realized by means of a further coils system. The conceptual scheme is analogous to that of the magnetic field produced by two wires carrying current in the same direction: the first wire corresponds to the plasma current and the second to the divertor coils system (figure 1.11). The divertor targets have to withstand to a really high energy load (several MW/m^2) and particles fluxes. It is therefore one of the most critical tokamak components. From figure 1.11a, a point characterized by a null poloidal magnetic field, also

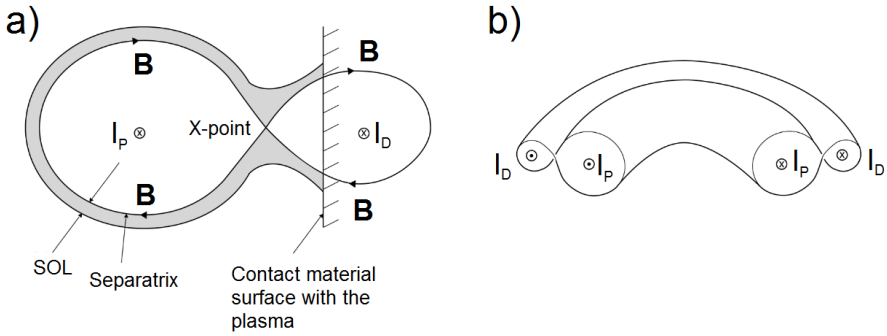

Figure 1.11: *Bi- (a) and three-dimensional (b) sketches of the divertor configuration.*

called X-point, is visible. The magnetic surface passing through the X-point is known as magnetic separatrix, since it divides the hot plasma from the boundary plasma. It is clear that the magnetic separatrix coincides with the LCFS. Another schematic representation of the divertor plasma configuration is shown in figure 1.12a. The plasma underneath the X-point and above the separatrix is called private plasma. It is due to the transversal transport in the plasma boundary. Figure 1.12b displays the divertor design of the tokamak ITER, currently under construction (see section 1.6).

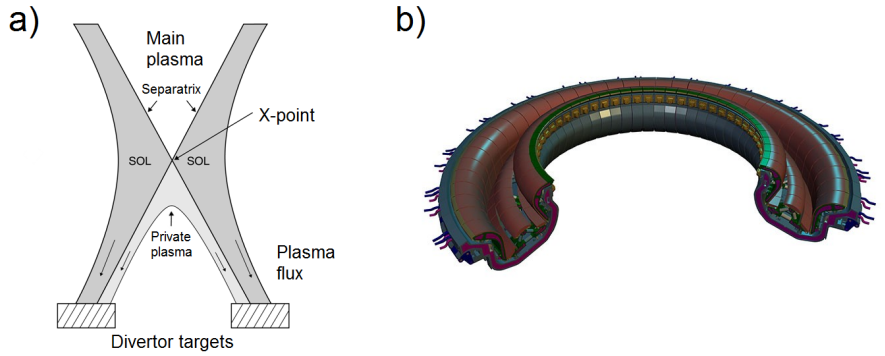

Figure 1.12: *(a) Plasma configuration in correspondence of the divertor region [8]. (b) ITER divertor design [2].*

Both with limiter and divertor configurations, the plasma region beyond the LCFS is also known as Scrape-Off-Layer (SOL). Considering the Joint European Torus (JET, Culham, Oxfordshire, United Kingdom) tokamak, the comparison between the magnetic field structure for limiter

and divertor configurations is shown in figure 1.13.

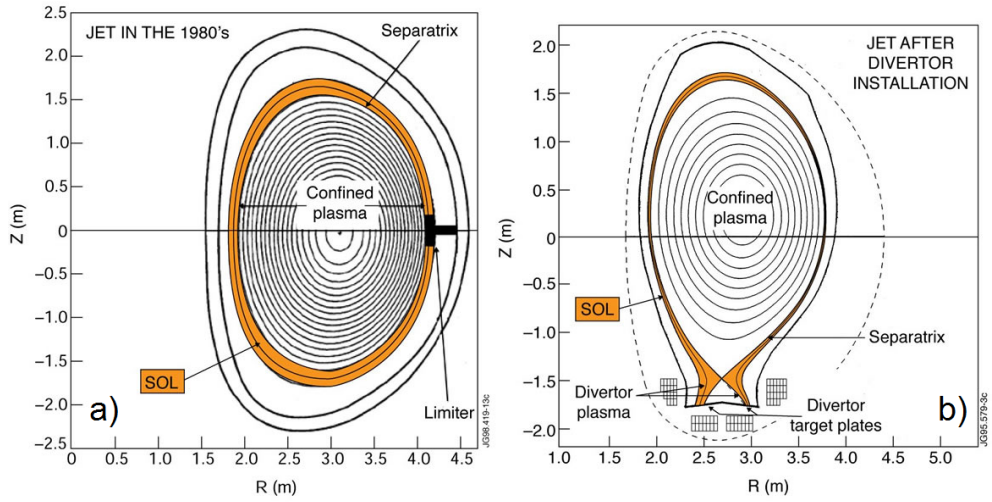

Figure 1.13: *JET magnetic field structure for limiter (a) and divertor (b) configurations.*

1.6 ITER

Most of the nowadays tokamaks operate with deuterium fueled discharges to avoid the safety constraints relative to the use of tritium. However, two large tokamaks, the Tokamak Fusion Test Reactor (TFTR, Princeton, New Jersey, USA) and JET, were designed for pioneering studies of plasma scenarios with a D-T fuel. Using a 1:1 ratio of deuterium to tritium, they both produced a significant amount of fusion power [9]. 10.7 MW of fusion power with a fusion energy gain factor of Q$\sim$0.27 were generated in TFTR during 1994 [10]. An extended D-T phase was carried out at JET in 1997 during which 16.1 MW from fusion reactions were produced, for a corresponding fusion energy gain factor of Q$\sim$0.62 [11]. Although these results represented a real breakthrough in the field of magnetic confinement nuclear fusion, the Q ratios obtained during these experiments were not sufficient to reach the break-even condition. They were therefore very far from what would be necessary for a commercial power plant. Experimental scaling laws have shown the strict dependence of the energy confinement time τ_E to the tokamak dimension and aspect ratio [12]. The production of energy from fusion at an industrial scale thus requires a significant jump in terms of machine performance. To

this end, ITER ("the way" in Latin) is currently under construction adjacent to the CEA Cadarache research centre in the Southern France (seven participants: European Union plus Switzerland, the USA, Japan, China, Russia, India, South Korea; First Plasma: November 2020). The main goal of ITER is to demonstrate the scientific and technological feasibility of producing net energy by means of fusion reactions. ITER should achieve this objective by proving high power amplification (at least 500 MW of fusion power starting from 50 MW of input power, $Q \geq 10$) with a D-T plasma, over a long time period (500 s).

The key role of ITER in the success of the magnetic confinement nuclear fusion is noticeable. Both the ambition and the complexity of this project produce an interesting and intricate storyline [2] which deserves a brief description.

1.6.1 Milestones in the history of the ITER project

At the Geneva (Italy) Superpower Summit in November 1985, US President Ronald Reagan and Soviet Secretary-General Mikhaïl Gorbachev met for the first time and, within the discussion devoted to scientific and technological challenges for the future decades, agreed on an international effort to develop fusion energy *"as an inexhaustible source of energy for the benefit of mankind"*. At the Reykjavik (Iceland) US-USSR Summit on 11-12 October 1986, an agreement was reached between the European Union (Euratom), Japan, the Soviet Union and the USA to jointly pursue the design for a large international fusion facility, the "International Thermonuclear Experimental Reactor" (ITER). Its project began with the Conceptual Design Activities (CDA) process during April 1988. The CDA took place in Garching (Germany) at the Max Planck Institut für Plasmaphysik (IPP). Some 50 professional staff representing all the ITER project Parties met together for six months each year until 1990 under the aegis of the International Atomic Energy Agency (IAEA). CDA had the goals of selecting the technical characteristics of the ITER device and validating the resources needed. It also carried out a safety and environmental analysis of the design and defined the construction site technical characteristics. CDA was successfully completed in December 1990. Afterwards the Parties entered into negotiations on how ITER should have proceeded. On the 21st of July 1992 in Washington DC (USA), the ITER Engineering Design Activities (EDA) was signed by representatives of the four Parties: the Russian Federation (heir of the role initially played by USSR), the USA, Europe and Japan. Joint Work Sites were set up at three locations: San

Diego (USA), Garching (Euratom) and Naka (Japan). Canada and Kazakhstan (also formerly part of USSR) became involved by association with Euratom and Russia, respectively. Six years of international collaborative work within the framework of the ITER EDA Agreement culminated in the approval by the ITER Council, in June 1998, of the ITER Final Design Report (figure 1.14a). Despite the existence of previous designs [13,14], it was the first of a fusion reactor based on well-established physics and technology. Its design fulfilled the overall programmatic objective of ITER and complied with the detailed technical objectives and approaches adopted by the ITER Parties at the start of the EDA. The main parameters of the ITER EDA project are reported in the second column of table 1.1. However, during December 1998, concerns about the projected cost of the programme led the USA to end participation in ITER. The San Diego Joint Work Site closed.

A new design, named "ITER-FEAT" (figure 1.14b), was produced for ITER, and was approved by the ITER Council in July 2001. It maintained the overall programmatic objectives of the project, while integrating cost-cutting measures. Symbolically, the meaning of ITER was changed. ITER was no longer an acronym for International Thermonuclear Experimental Reactor, but the Latin word "iter" which means "the way". The main parameters of the ITER-FEAT project are listed in the third column of table 1.1.

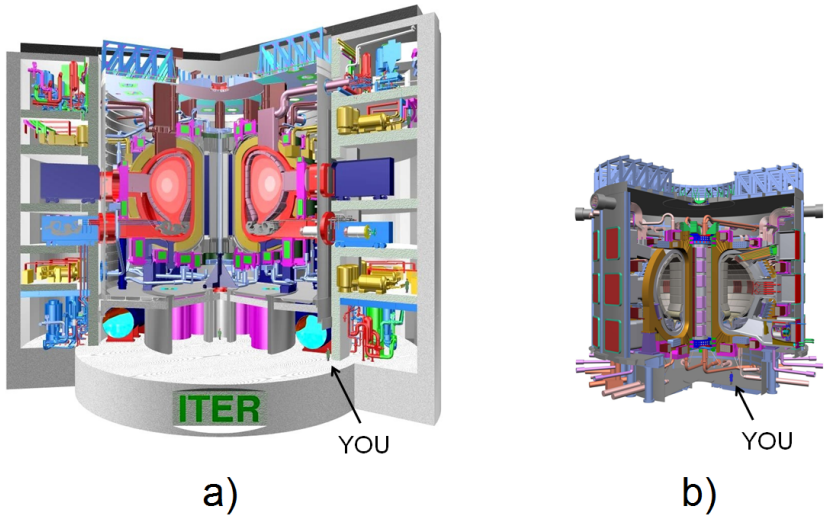

Figure 1.14: *Comparison between ITER EDA design (a) and ITER-FEAT design (b).*

	ITER EDA	ITER-FEAT
Total fusion power	1.5 GW	500 MW *(700 MW)*
Average 14.1 MeV neutron wall loading	$\sim$1 MW/m^2	0.57 MW/m^2 *(0.8 MW/m^2)*
Plasma ignition time	$\geq$ 1000 s	$\geq$ 300 s
Plasma major radius (R)	8.14 m	6.2 m
Plasma minor radius (a)	2.80 m	2.0 m
Plasma current	21 MA	15 MA *(17 MA)*
Toroidal field	5.68 T @ 8.14 m radius	5.3 T @ 6.2 m radius
Plasma volume	$\sim$2000 m^3	873 m^3
Plasma surface	$\sim$1200 m^2	678 m^2
Available auxiliary heating power	100-150 MW	73 MW *(100 MW)*

Table 1.1: *Main ITER EDA [12] vs. ITER-FEAT [15] parameters.*

Following preparatory meetings in Vienna (Austria) and Moscow (Russia), where new partner Canada presented its bid to host the ITER project (Clarington, Ontario), delegations from the Parties convened in Toronto on the 8$^{\text{th}}$ of November 2001. The Toronto negotiations were the first in a series that would have led to an agreement on the joint implementation of ITER.

China presented a formal request to join ITER on the 10$^{\text{th}}$ of January 2003. Twenty days later (30$^{\text{th}}$ of January 2003) the USA announced its return to the ITER project. The 2$^{\text{nd}}$ of July of the same year, the ITER Parties officially accepted South Korea's application for participation in the project. In this way ITER had acquired a truly global dimension.

In parallel, during June 2003, Japan proposed Rokkasho-Mura, located in Aomori Prefecture, as the ITER site. Europe initially hesitated between Vandellòs (Spain) and Chadarache (France) until the 26$^{\text{th}}$ of November 2003 when the 25 European Ministers of Science and Research unanimously agreed to propose Cadarache. It was also decided that Spain would have hosted the future ITER European Agency ("Fusion For Energy", F4E). In light of the competitive proposals submitted by Europe and Japan for the ITER location, ITER-Canada, the private-sector consortium that developed the offer to locate ITER in Clarington, announced its withdraw from the ITER negotiations on the 23$^{\text{rd}}$ of December 2003.

On the 5$^{\text{th}}$ of February 2005 in Tokyo, the Minister for Foreign Affairs of Japan, Mr. Taro Aso, and the Ambassador of the Delegation of the European Commission to Japan, Mr. Hugh Richardson, signed the Agreement for the Joint Implementation of the "Broader Approach Activities" in the Field of Fusion Energy Research. The Broader Approach was defined as a privileged and equal partnership between the European Union and Japan to complement the ITER project and to carry out R&D and advanced technology development for the "next-step" device, the future

DEMOnstration power reactor (DEMO). After a period of high-level political negotiations, the decision to locate ITER in Cadarache was reached on the 28th of June 2005 at a ministerial-level meeting in Moscow. The decision was based on a bilateral agreement between Europe and Japan over cost sharing and the Broader Approach complementary development projects to be located in Japan in support of ITER and the next-step device DEMO. Ambassador Kaname Ikeda, former Japanese Deputy Minister for Science and Technology and "Director Nominee" for the future ITER Organization (IO), inaugurated the "Joint Work Site" at Cadarache on the 15th of December 2005.

During the same month, India joined ITER, bringing Member Parties to seven. Thirty-three nations and more than a half of the world's population were involved in ITER.

The signing of the ITER Agreement took place on Tuesday, 21st of November 2006 at the Élysée Palace, in Paris. French President Jacques Chirac, European Commission President José Manuel Barroso and some 400 invited guests including high level representatives from the ITER Parties and European Member States were present.

During January 2007, site preparation at Chadarache began, representing an important milestone on the road of building ITER.

On the 24th of October 2007, following ratification by all Parties, the ITER Agreement entered into force and the IO was formally established.

The work of the IO is supervised by its top body, the ITER Council (IC), which has the authority to appoint senior staff, amend regulations, decide on budget issues, and allow additional states or organizations to participate in ITER. The IC comprises of four representatives per ITER Member. The Chair and Vice-Chair of the Council are elected from amongst the Members and can remain in charge for up to four years. Meetings of the IC are held at least twice a year. The first of them was organized at Cadarache on the 27th of November 2007. The IC has been convened thirteen times up to now.

The construction work on ITER began in 2010 and is expected to come to an end in 2019. A commissioning phase will follow. It will ensure the correct operation of ITER and prepare the machine for the achievement of the First Plasma in November 2020. ITER's operational phase is expected to last 20 years. First, a several-year period of operation in pure hydrogen is planned during which ITER will remain accessible for repairs. In parallel, the most promising physics regimes will be tested. This phase will be followed by operation in deuterium with a small amount of tritium to test wall-shielding provisions, towards the end of 2027. Finally, a third phase

with increasingly frequent operation with an equal mixture of deuterium and tritium, at full fusion power, will be launched.

1.6.2 Materials choice for ITER

One of the main topical issues that the ITER community has to address consists in the choice of the Plasma Facing Components (PFCs) which, as remarked in section 1.5, will endure extreme conditions in terms of intense thermal loads, strong radiation fields and high particle fluxes. PFCs include the main chamber and divertor, the heating systems and the diagnostics. Since ITER diagnostics, and in particular first mirrors, constitute the specific subject of this Ph.D thesis, they will be introduced and described in chapter 2. The choice of materials for ITER PFCs has to meet different and not easily compatible goals: maximizing plasma performance, ensuring PFCs long lifetime, reducing safety issues like tritium retention, etc. The completion of the ITER engineering design with the ITER-FEAT project in 2001 has brought to an innovative choice of materials for main chamber and divertor [16]. The ITER poloidal section is shown in figure 1.15.

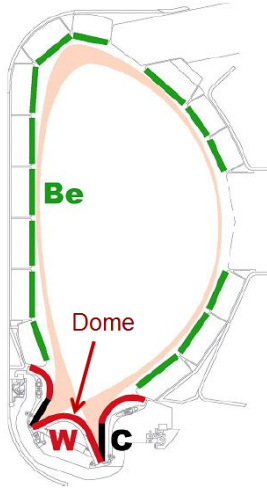

Figure 1.15: *Cutaway of ITER which shows the layout of plasma-facing materials.*

Beryllium (Be) will be used to cover the main toroidal chamber (total area $\sim$700 m^2) because it has the advantage of being a low-Z material with a good thermal conductivity and a strong affinity for oxygen (free energy for oxide formation -581 kJ/mol) making it a very good oxygen getter [17].

Its main drawbacks are a high sputtering yield and a relatively low melting point (1560 K), which limit its power handling capability. Be in the form of dust is also toxic, although the safety precautions to be taken will be similar to those due to the presence of tritium in the vacuum vessel.

Tungsten (W) as a high-Z material with a low sputtering yield and a high melting point (3695 K) will be used for the baffle regions of the divertor targets and for the surface of the divertor dome (total area $\sim$100 m^2). Finally, Carbon Fibre Composite (CFC) was initially chosen for the divertor targets as a result of its high thermal shock resistance owing to its lack of a melting phase at the interested pressures, making it extremely resistant under the strong transient heat loads expected during ITER plasma instabilities. However, carbon (C) has a significant hydrogen retention and, since the nuclear license limits the T-inventory in ITER to 350 g for safety reasons [16], removal techniques should have been employed to recover the trapped tritium. Moreover CFC materials endure severe degradation of their thermo-mechanical properties under high fluence neutrons irradiation at fusion neutron energies [18]. These concerns, together with budget issues, brought the ITER Council during the 13^{th} meeting at Saint Paul-lez-Durance (France), on 20-21 November 2013, to the choice of a full-W divertor for ITER [2].

2

Diagnostics and first mirrors in ITER

This chapter deals with the topic of the ITER diagnostics. They will have to guarantee the control of the nuclear fusion process together with the integrity of the vacuum vessel and thus the safety of the entire system. In section 2.1 a survey of some of the main diagnostics foreseen to be installed in ITER will be described. As an example, the Thomson scattering core light detection and ranging diagnostic, which will measure the electron temperature and density in the core region of ITER plasma, will be discussed in more detail in section 2.2, both to give further insight on the big challenges that the ITER community has still to address and also to introduce the specific topic of this Ph.D thesis: diagnostic first mirrors. As it will become clear later, they will be very important components in the frame of the correct operation of most of the ITER diagnostics based on the measurement of the electromagnetic radiation coming from the plasma. The main open issues associated to first mirrors, i.e. mirrors erosion by energetic particles coming from the ITER plasma and re-deposition of eroded first-wall material transported in the plasma onto their surface, will be presented in section 2.3. Based on this introduction, the specific objectives of this thesis and the experimental methods used to accomplish them, will be discussed in section 2.4.

2.1 ITER diagnostic challenges

Diagnostics will be a crucial part of the operation of ITER [19]. They will provide the means to observe, control and sustain the plasma performance over long timescales and in different plasma scenarios, and to prevent off-

normal events that could otherwise lead to the damage of the machine. This brings to the following classifications of the measurement parameters (and related diagnostics): those required to support the normal operation of ITER (ELMy, where ELM stands for Edge Localized Mode, H-mode operation), those required to support more advanced scenarios and those for the machine protection. Measurements of these parameters will also provide data to be used in the planned physics studies in the ITER research programme. As a general remark, the specifications of measurements for physics studies are frequently more demanding (e.g. in terms of spatial and time resolution) than those needed for the control and machine protection functions. Furthermore, additional parameters have sometimes to be measured solely for physics purposes.

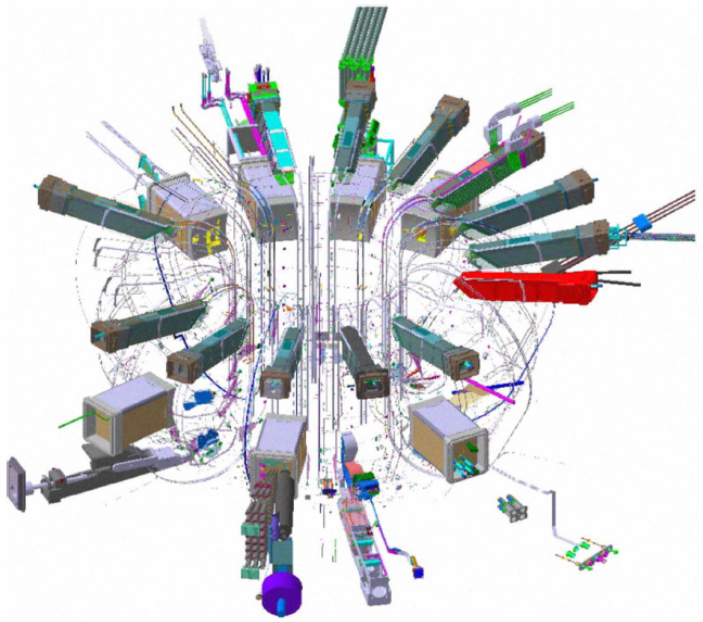

Figure 2.1: *An overview of the diagnostics installed in ITER [19].*

Considering the different diagnostics, in some cases these systems are well developed in current tokamaks (interferometry, spectroscopy, Thomson scattering, etc.) while in other cases, they will cover new ground (e.g. alpha particles systems). The diagnostics implementation in ITER is however a new domain in both operating space and environment and it provides many challenges in terms of physics and engineering perspectives. The set of diagnostics in ITER will include approximately 45 different measurement systems. The diagnostics can be broadly classified into the

following categories: Magnetic, Optical, Bolometric, neutron and particle, spectroscopic and Edge systems.

The integration of the different diagnostics into ITER requires an unprecedented level of coordination with all the other parts of the machine design process. Diagnostics will be installed both in-vessel and ex-vessel (figure 2.1) and the transmission systems will follow paths from the vacuum vessel all the way to the diagnostics building [20, 21]. Diagnostics components will be placed in several Upper, Equatorial and Lower ports. Their integration into the ports plugs will be facilitated by following a design integration procedure. Let us consider a specific example. Equatorial 11 is one of the ports which will benefit from this procedure. It will contain several diagnostics including neutral particle analyzer, residual gas analyzer, radial and divertor viewing, vacuum ultraviolet spectrometers, radial X-ray survey spectrometer, low field reflectometry as well as Balmer-alpha and impurity viewing systems. The integrated view of Equatorial port 11 is shown in figure 2.2.

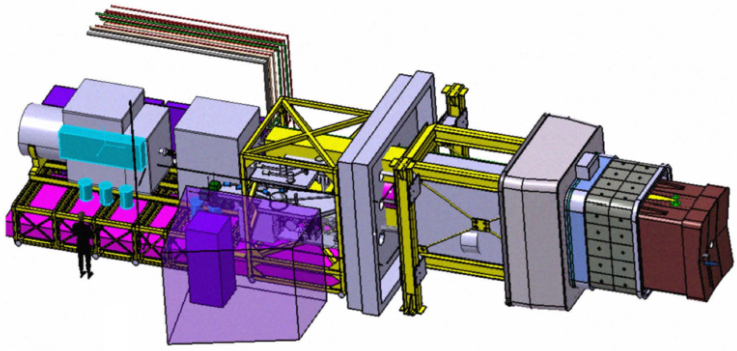

Figure 2.2: *Integration of Equatorial port 11 [19].*

Access to diagnostics in the area of the ITER tokamak will be generally quite limited and in some cases will be impossible after the initial assembly. This constitutes a key constrain in the design of the diagnostics. A high degree of diagnostics redundancy and reliability is therefore mandatory.

Together with these general issues, the design of each ITER diagnostic has to face additional specific problems depending on its functional principle, its required accuracy and its position with respect to the plasma. Considering optical diagnostics, i.e. those which will collect the radiation emitted, reflected and diffused by the ITER plasma, first mirrors constitute a relevant issue. Due to the high level of neutron and electromagnetic radiation in ITER, the solution of viewing the plasma by means of optical

windows or fibers is impossible (see section 2.3). It has been therefore decided to recess these components transmitting the light from the plasma by metallic mirror optics located in labyrinths embedded in the shielding material.

To give further insight on the importance of the main ITER diagnostics, their specific objectives and distinctive features will be briefly described in the following subsections. In particular, they will be classified in terms of the parameters to be measured. Moreover, since first mirrors constitute the core of this Ph.D thesis, their principal characteristics for some of the optical diagnostics discussed, will be underlined.

2.1.1 Measurements of electron temperature and density

Thomson scattering systems [22] (in particular, the LIDAR typology will be discussed in detail in section 2.2) and Electron Cyclotron Emission (ECE) systems will have the primary aim to measure the electron temperature with good spatial and temporal resolution [23]. From the ITER measurement requirements, the electron temperature profile should be determined with a resolution of about 70 mm and an accuracy of 10% in the plasma core, for the temperature range 0.5-40 keV, and with a spatial resolution of 5 mm in the boundary regions. The instruments to analyze the ECE from the ITER thermonuclear plasma will be Michelson interferometries and heterodyne radiometers. In detail, the electron cyclotron radiation will comprise of Ordinary, or O-, modes with frequencies between 122-230 GHz, and eXtraordinary, or X-, modes with frequencies between 244-355 GHz, for a toroidal magnetic field in the range 2-5.3 T. Since Thomson scattering and ECE systems are optical diagnostics, first mirrors issue needs to be carefully considered in order to guarantee their correct operation. In the case of the Thomson scattering system placed in ITER divertor, the first mirror foreseen is a rhodium or dielectric mirror with an area of 430×270 mm^2 working in the wavelength (λ) range 800-1060 nm [3].

The reflectometry systems will allow to measure the core and edge plasma density profiles, as well as other peculiar plasma features. Some of the reflectometry systems will have interfaces with the vacuum vessel. The in-vessel waveguides will be directly welded on the vacuum vessel surface and will be protected by the blanket from the plasma side. The antennas are designed to view the plasma through the cut-outs in the blanket and first-wall. Therefore, the in-vessel waveguides supports and welds should withstand to the mechanical stresses caused by the electromagnetic loads

during off-normal events, and the antennas should be made of a material capable to resist to intense thermal and neutron heating fluxes.

2.1.2 In-vessel dust, tritium and erosion measurements

For both the safe operation and meeting the nuclear regulatory requirements, an accurate inventory of the tritium and dust (originated from first-wall erosion by thermonuclear plasma) inside the ITER vacuum vessel will be mandatory. Furthermore, a precise assessment of the erosion, especially in correspondence of the divertor region will be required [24]. With the aim of accomplishing all these tasks, an active and passive dust monitor and a tritium wall retention monitor will be installed. A crucial aspect of the dust handling programme consists in measuring the hot dust in the vessel, that is dust on surfaces that become hot (T > 400 °C). An evaluation of the hot dust critical threshold is necessary. The latter is calculated from the maximum pressure allowed for ITER (2 Bar). The pressure increase could be due indeed to a hypothetical hydrogen explosion (hydrogen being produced by hot dust reacting with steam during a Loss-of-Coolant Accident, LOCA, scenario). The main proposal for this measurement will consist of evaluating the chemical reactivity inside the tokamak with a controlled injection of water (steam) during the baking phase. This technique could be complemented qualitatively by passive study of infrared emissivity of key surfaces or quantitatively by active laser illumination.

2.1.3 Measurements of impurities

Impurities could be intrinsically produced in the plasma as fusion reaction ash, they could be generated by plasma-wall interaction on the solid surfaces surrounding the discharge or they could be injected or puffed into the plasma for performance optimization or diagnostic purposes. Impurities could play an important role in all regions of ITER tokamak from the core plasma to the SOL and the divertor plasma. Measurements of their concentration, ionization and kinetic state in the discharge could be performed by passive and active spectroscopy of continuum and line radiation, in a wavelength domain ranging approximately from 0.05 to 1000 nm.

Let us consider a specific example. Charge eXchange Recombination Spectroscopy (CXRS) will be based on the injection of a dedicated diagnostic neutral hydrogen beam (100 keV, 36 A) interacting with fully

stripped plasma ions. A fan of poloidal and toroidal lines-of-sight covering the beam path from plasma edge to magnetic axis (figure 2.3) will measure the emission spectra of fully stripped ions following the charge capture from the neutral beam. The first mirror of this diagnostic will

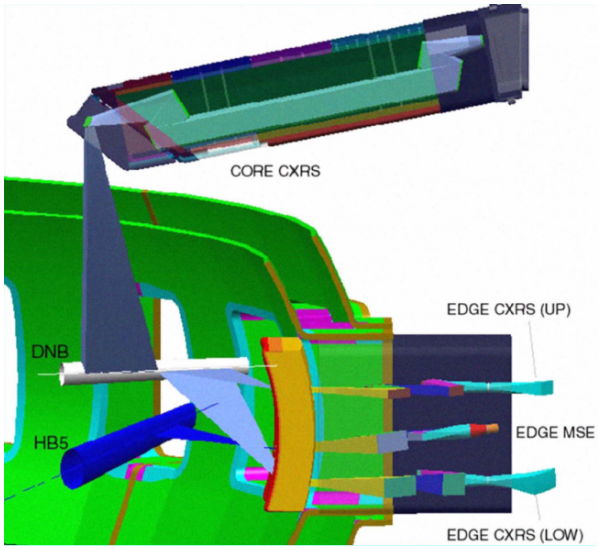

Figure 2.3: *Schematic assembly of active beam spectroscopy on ITER making use of a radially injected diagnostic neutral beam and one U-port and E-port periscopes [19].*

work in the λ range 468-1012 nm and will have 200×200 mm^2 dimension. However, its material has still to be decided [3].

2.1.4 Fusion power measurements

The measurement of the fusion power, in terms of the total neutron emission, will play a key role for achieving ITER goals, in particular a value of 10 for the fusion energy gain factor Q. The neutron rate in ITER will span over seven decades from 10^{14} up to almost 10^{21} n/s corresponding to 100 kW up to 1.5 GW. ITER neutrons diagnostics will have to provide the measurement of the neutron rate within an accuracy of 10% and a temporal resolution of 1 ms. Several monitors with different sensitivity will have to be used for covering such a wide neutron emission range. The layout of the neutrons diagnostics in ITER is reported in figure 2.4. Fission chambers with different uranium content will be used as the detectors and will be positioned in various locations inside ITER. These will include the diagnostics ports, the divertor and the vacuum vessel wall. ITER high neutron flux (up to 10^{14} n cm^{-2} s^{-1} with 14.1 MeV neutron energy), tem-

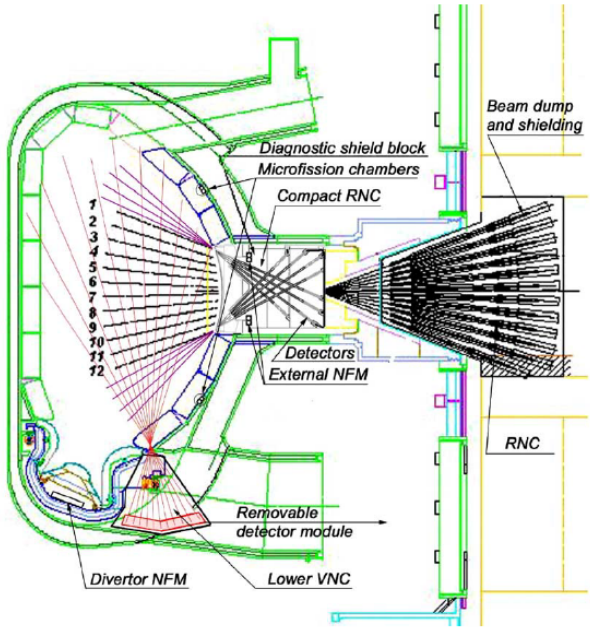

Figure 2.4: *The layout of the ITER neutrons diagnostics system [4].*

peratures, magnetic fields and electromagnetic induced noise, will make the assessment of the unperturbed neutron spectrum, and hence the fusion power measurement, really complex. Moreover, many technical challenges also characterize each neutron diagnostic. In particular, their calibration will be very important in order to determine the relationship between neutrons sensors output and the total neutron emission from the whole plasma, taking into account the features of an extended neutron volume source, the neutron scattering contribution as well as neutron moderating effect due to the structures surrounding the sensors. To achieve the accuracy target of 10% on total neutron emission measurement it will be necessary to ensure: functional linkage between the various neutrons diagnostics, *in-situ* absolute neutrons calibrations obtained with accuracy much better than 10% and precise transport calculation [25].

2.1.5 ITER first-wall monitoring

The infrared and visible viewing systems in ITER will be required to study the device boundary during operation. An example of these systems is reported in figure 2.5. The viewing systems will be impacted by the choice of the first-wall materials. As described in subsection 1.6.2, ITER main

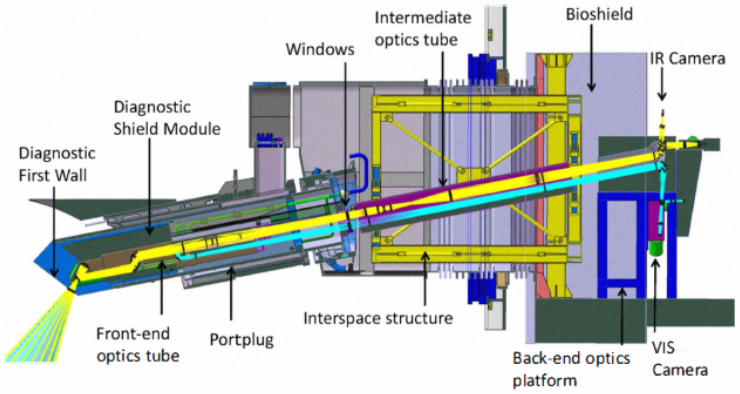

Figure 2.5: *Scheme of a system aims to view the divertor in both the infrared and visible wavelength regions. The light is relayed from the machine and guided beyond the bioshield for viewing by the camera systems [19].*

toroidal chamber will be covered by Be. The use of this material will provide a much more reflective inner vessel wall with respect to those of the operating C-wall tokamaks. This feature should be considered in the frame of the evaluation of the ITER first-wall temperature [26]. In particular, special measurements and calibrations need to be developed. Nowadays, the Axially Symmetric Divertor EXperiment Upgrade (ASDEX-U) tokamak (Garching, Germany) is able to explore metallic environment working with an all-W wall, and the JET tokamak has recently adopted the same materials configuration as ITER for the first-wall (in the frame of the ITER-Like-Wall project, ILW [27], see section 6.1).

Considering the ITER infrared viewing system, it will rely on a first mirror made of a rhodium film deposited onto a copper substrate with a diameter of 120 mm operating in the wavelength range 0.4-5 μm [3].

2.1.6 Measurements of neutral gas composition

One of the operational parameters in the ITER measurement requirements is the neutral gas composition during plasma operation. This quantity will be essential to assess the divertor performance in removing He ash and impurities from the plasma. To fulfill this task, two Residual Gas Analyzer (RGA) diagnostics will be implemented inside one of the divertor level pumping ducts (figure 2.6) and at one of the Equatorial ports, respectively. Albeit conventional vacuum systems analyze the residual gas by means of Mass Spectrometers (MS), which ionize the gas molecules and successively discriminate the mass-to-charge ratio applying suitable elec-

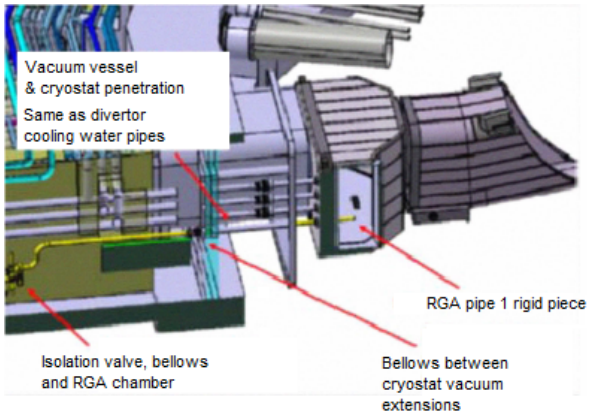

Figure 2.6: *Residual gas analyzer installed at the divertor level [19].*

tric and magnetic fields, this technique is not consistent with the strong magnetic fields inside the ITER tokamak. With the aim of exploiting this technology, the ITER RGAs are configured to draw the gas into differentially pumped gas analysis chambers through sample tubes 7 m long, in the case of the RGA of the divertor, and 10 m long, in the case of the RGA at the Equatorial port, respectively. The pipes diameter and the differential pump size are chosen to minimize the time for the gas to reach the analyzer to about 1 s. With the MS chamber in a region of relatively weak magnetic field, it is possible to consider turbomolecular pumps over cryopumps, the latter having a disadvantage in that the accumulation of gas on the pump raises a hydrogen deflagration issue. The turbopumps will nevertheless require magnetic shielding to limit the eddy currents drag in the rotating parts.

Since the MS cannot easily discriminate He and D_2 molecules, an Optical Gas Analyzer (OGA) will be also incorporated in the RGA diagnostics. The OGA comprises of a Penning discharge, the light from which is analyzed with a spectrometer.

2.2 ITER Thomson scattering core light detection and ranging diagnostic

In order to give further insight on the big challenges that the ITER community has still to address, especially from first mirrors point of view, in this section the attention is focused on a specific optical diagnostic:

the Thomson scattering core light detection and ranging. After a general overview of the technique, collection optics technological solutions proposed in the frame of the methodology reported in [28] will be discussed.

As mentioned in subsection 2.1.1, Thomson Scattering (TS) diagnostics will be used in ITER to evaluate the electron temperature with good spatial and temporal resolution. In Thomson scattering, the radiation from a high power laser is injected into the plasma and the radiation scattered incoherently by the electrons is collected and spectroscopically analyzed [29]. The measurements of the spectral width and intensity of the scattered signal allow electron temperature T_e and density n_e to be respectively determined. The chosen approach for ITER is known as LIght Detection And Ranging (LIDAR) technique [22, 30]. In this case, the spatial distributions of T_e and n_e are obtained by the Time Of Flight (TOF) principle. The current section describes the TS-LIDAR diagnostic proposed for measuring T_e and n_e in the core region of the ITER plasma [28] (figure 2.7).

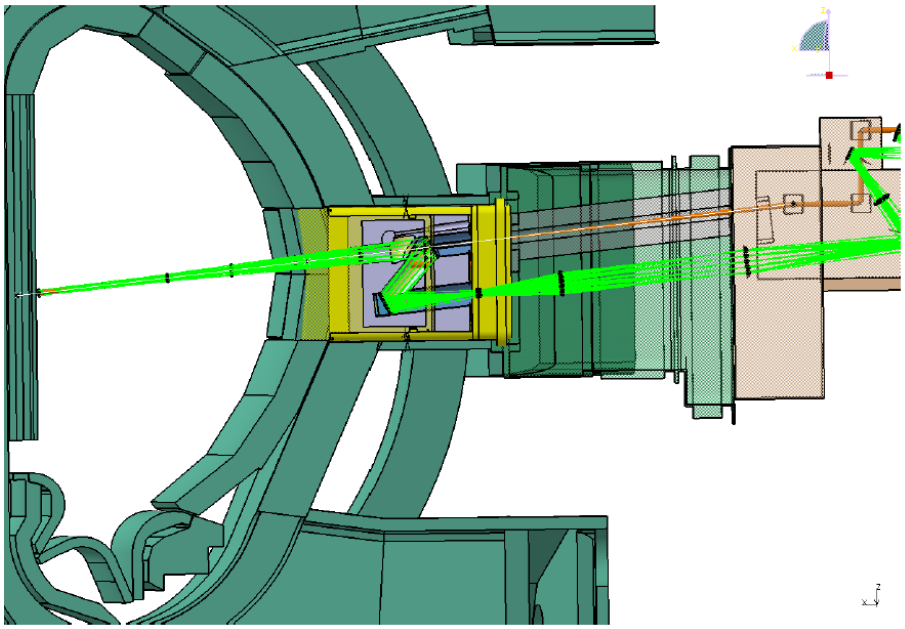

Figure 2.7: *ITER vacuum vessel and core TS-LIDAR diagnostic port plug showing injection of the probe laser beam (red lines) and collection of Thomson scattered light (green lines) [28].*

As introduced so far, the ITER required spatial resolution for T_e and n_e profiles in the plasma core is about 70 mm. Core TS-LIDAR diagnostic

should resolve temperatures in the range from 0.5 keV to 40 keV and densities in the interval from 3×10^{19} m^{-3} to 3×10^{20} m^{-3}. The ITER harsh environment limits the proximity of the light collection optics and their dimension. Due to the low TS cross section of the electrons as well as the low collected solid angle, the signal detected will be very weak, demanding the use of a high energy laser. Moreover, together with the Thomson scattered light signal, there will be a significant amount of light pollution received from plasma background light. The latter will come from Bremsstrahlung in the centre of the plasma and fluorescent emission from the its edge (where the temperature will be sufficiently low to permit some electrons to recombine). The plasma temperature will be determined from the Doppler broadening of the scattered light. The light is also heavily blue shifted at high plasma temperatures [22, 30, 31]. A laser operating with a wavelength in the infrared region, at around 1 μm, will be used and the scattered light will be detected at the shorter wavelengths side. The scattered light will be measured using interference filter spectrometers [32] around 1 μm at the lower core temperatures and extending down to 300 nm for the highest core temperatures. The detectors will have a very fast pulse response ($<$ 200 ps rise time, $<$ 330 ps Full Width at Half Maximum, FWHM) in order to achieve the required spatial resolution by TOF. The scattered light will be also collected from a significant range of depths within the plasma and will have to be delivered to spectrometers some 30 m away from the vacuum vessel. The longitudinally extended scattering source will give rise to a relatively high etendue of the light to be relayed to the spectrometers. This implies that the relay optics will be large and that the detectors will be large as well as fast. In the frame of the methodology proposed in [28], which aims to satisfy all these demanding requirements, at least to some extent, the core TS-LIDAR diagnostic is divided into seven modules: laser source, laser beam delivery optics, beam dump, collection optics, spectrometers, detectors and calibration. Since the main topic of this Ph.D thesis is constituted by first mirrors, the attention is now focused on the technological solutions investigated for the block of the collection optics (figure 2.8).

The view of the ITER plasma will be limited by the availability of space in the port plugs. The LIDAR configuration will minimize the area of the diagnostic, collecting the scattered light at 180°. The first optical component of the collection system is clearly the first mirror (component M1 in figure 2.8), which will require to be protected from the ITER harsh environment in order to maintain acceptable performance during tokamak operation. The first mirror will be then behind a limited size aperture in

the plasma wall blanket. A diameter of around 360 mm has been chosen. With the aim of minimizing the erosion of the first mirror surface by the energetic particles coming from the plasma, it will be of a low sputtering metal such as rhodium or molybdenum. The succeeding optical relay system will be optimized in order to ensure that as much of the light reflected by the first mirror will be transmitted towards the spectrometers located 30 m away in the laser room. By using radiation resistant multi-layers coatings, the second (component M2 in figure 2.8) and subsequent mirrors could be high reflective dielectric mirrors to reduce the transmission losses. In order to determine T_e and n_e over the full operating temperature range of the ITER plasma (up to 40 keV), these coatings must have a high reflectivity over the range 300÷1070 nm.

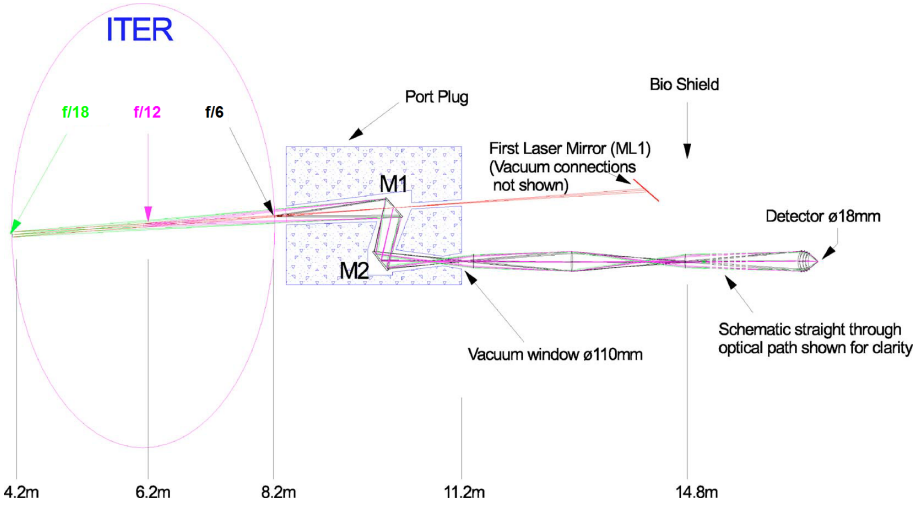

Figure 2.8: *Scheme of the light collection line of ITER TS-LIDAR diagnostic [22].*

The light scattered from the plasma will represent a distributed source which has some transverse extent and a very large longitudinal dimension, requiring the use of relatively large optics. In particular, the recommended diameter for the first mirror is 350 mm [3]. The employment of an axicon optical element would allow to operate with smaller optical elements following the axicon, or at grater separation. A converging axicon would be placed slightly after the focus of the extreme outboard scattering position to be analyzed or alternatively a diverging axicon could be used just before the focus of the extreme inboard scattering location. A further advantage of exploiting an axicon would be that smaller interference filters and area detectors may be used in the spectrometer. As well as being beneficial on

cost grounds, this also would lead to a reduction in the collection of background light at the detector and to a consequent improvement in signal to noise ratio.

2.3 First mirrors for diagnostic systems in ITER

As it is described in sections 2.1 and 2.2, ITER optical diagnostics will involve the use of the electromagnetic radiation emitted, reflected or diffused by the thermonuclear plasma, to evaluate its main features. In nowadays tokamaks, most of these systems view the plasma through optical windows or fibers. Considering the design and expected performances of ITER, fast neutron fluxes of $\sim 3 \times 10^{13}$ and $\sim 2 \times 10^{13}$ n m^{-2} s^{-1} are expected at the first-wall and just outside the ports, respectively [33]. In addition, strong γ fields up to 10^4 Gy/s and intense ultraviolet and X-ray radiations up to 500 kW/m^2 are expected. Silica-based windows are sensitive to Radiation-Induced Absorbtion (RIA), which determines a decrease of their transmittance for $\lambda < 800$ nm [34]. Materials with superior radiation tolerance (i.e. sapphire) suffer the Radiation-Induced Luminescence (RIL) after high γ radiation fluences [35]. As just discussed in the previous sections, and in particular in the case of the core TS-LIDAR diagnostic, for mitigating these problems and their effects on the diagnostic signals, it was proposed that the light from the plasma should have to be transmitted by mirror optics through labyrinths embedded in the shielding material. This solution has the advantage of recessing the vacuum windows or the optical fibers at the end of the mirrors chains some metres away from the region of intense radiation. Another beneficial consequence consists in the significant reduction of a factor of 10^4 of the level of neutrons with respect to the first-wall [36].

As it is also evident from the specific examples reported in sections 2.1 and 2.2, the first components of the mirrors labyrinths, different for each optical diagnostic, will be metallic mirrors. They are called First Mirrors (FMs). Being the closest elements to the thermonuclear plasma, most of them will be directly located on the first-wall of ITER, they will suffer the intense neutron and electromagnetic radiations mentioned so far, together with strong energetic ions and neutrals fluxes.

The International Tokamak Physics Activity (ITPA) Topical Group on Diagnostics through a Specialist Working Group (SWG) on first mirrors leads and coordinates the investigation of the FMs issue towards the development of optimal and robust solutions for ITER diagnostics system [37].

One of the most important decisions that the ITPA-SWG endorsed is the position of the ITER optical diagnostics around the tokamak and thus the corresponding location of the approximately 80 FMs. ITER poloidal section and FMs locations are represented in figure 2.9 [3]. Depending on the diagnostic requirements, the area of the first mirrors may vary between 2×2 cm^2 to 31.6×47.4 cm^2. With the goal of identifying the other optimal features for each FM (i.e. chemical and crystallographic nature, thickness, etc.) it is necessary to consider different aspects: the working wavelength range, the distance and orientation with respect to the plasma and the levels of radiation and particles fluxes under which it will operate. Furthermore, it is mandatory to take in account the effects of the interaction between ITER first-wall and plasma onto them, more specifically, the erosion and re-deposition phenomena (deeply described in the following) [37].

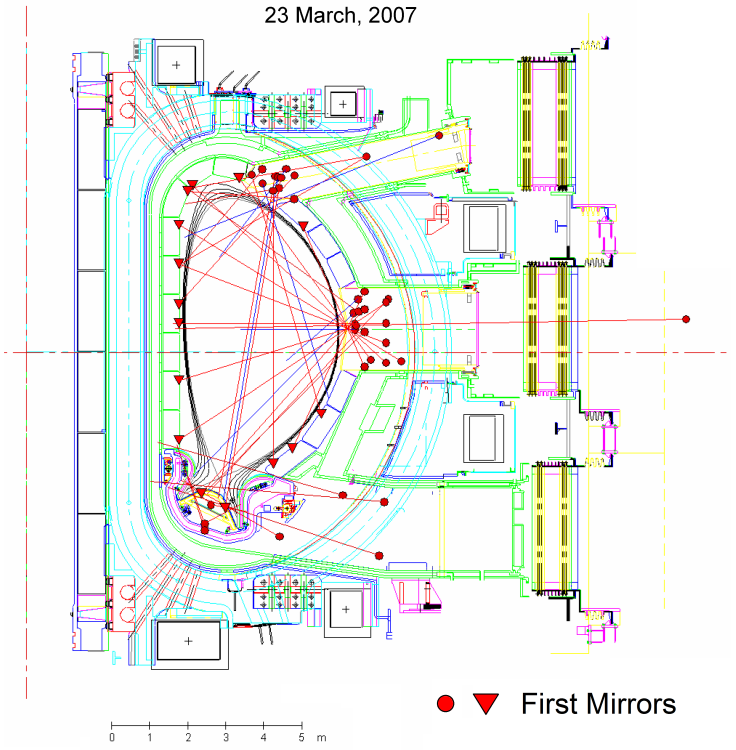

Figure 2.9: *Poloidal section of ITER showing the locations of the first mirrors in the vacuum vessel [3].*

The investigation of the different interaction mechanisms between thermonuclear plasma and first-wall (Plasma-Wall Interaction, PWI) is one of the most important and complex concerns in the frame of the development of nuclear fusion magnetic confinement systems. In particular, it is necessary to face different phenomena and to combine various research fields like plasma physics, atomic physics, chemistry, engineering. The complexity and extent of the PWI topic require a multitasking approach through theoretical studies and dedicated experimental campaigns. A complete dissertation about PWI concerns is out of the scope of this thesis and can be found in [38]. Since they will deeply influence FMs performances during ITER operation, only the PWI mechanisms of erosion and re-deposition will be now introduced.

2.3.1 Erosion by sputtering of plasma facing components

The erosion by sputtering is one of the well-know and most studied PWI phenomenon. Sputtering consists in the removal of atoms from the surface of a solid due to the impact of ions or atoms. When particles leave the surface as a result of receiving momentum from the collision cascade induced by the incident radiation, the process is called "physical sputtering". If the incoming radiation induces chemical reactions which lead to the subsequent desorption of particles, the process could be classified as "chemical sputtering".

Physical sputtering

Physical sputtering takes place when the collision cascade results in a surface atom receiving sufficient energy to overcome the surface binding energy of the solid. In this case, the sputtering yield Y (the number of atoms ejected per incident particle) is proportional to the energy deposited in elastic collisions within a near-surface layer. Physical sputtering is therefore a threshold process: at low incident particles energy, where the energy transferred to the solid surface atoms is comparable with the surface binding energy, Y decreases strongly and becomes zero below a threshold energy E_{th}.

The physical sputtering yield for the main ITER plasma-facing materials as a function of the energy of deuterium ions impinging with normal incidence shows a common trend [39]. Y increases, reaches a maximum and then diminishes at high energies. This decrease is due to the collision cascade taking place deeper in the solid so that the probability for the

surface atoms to receive a sufficient amount of energy to be sputtered is lower.

Considering the physical sputtering, Y increases with the angle of incidence described by the incoming radiation and the normal to the surface, since a higher angle of incidence means a higher amount of energy deposited within the near-surface layer [40]. Surface roughness determines a reduction of Y and of its pronounced behaviour with the angle of incidence [41]. Y of a given material depends also on its crystallographic structure. In particular, the sputtering yield associated to individual crystallites with different crystallographic orientations can vary by a factor of 2 on a broad energy range [42]. This phenomenon is particularly relevant for polycrystalline materials which are composed by crystallites with different orientations and therefore it clearly affects the choice of the manufacturing process for the FMs (see subsection 2.3.3).

In most of the nowadays tokamaks and in ITER, the typical impurity ions expected to leave the confined plasma are multi-charged Be, C, W ions which may thus impact the surrounding materials with a relevant energy. Moreover, tokamak magnetic field configuration, together with the ions Larmor motion, implies that ions hit the PFCs with a non-normal angle of incidence.

Another important contribution to physical sputtering in ITER will arise from Charge-eXchange Neutrals (CXN). These particles are neutrals, originated further to PWIs, which have been subjected to charge-exchange reactions with plasma ions, yielding neutrals with the local ion temperature. Since they are not influenced by the magnetic field, they can deeply penetrate into the confined plasma region (where the ion temperature is high) and experience a succession of charge-exchange reactions. This process thus transforms a fraction of neutrals with energy of a few eV into very energetic particles. Evidences of the damage of PFCs by CXN have been found in JET [43] and ASDEX-U [44]. In ITER, the fluxes of CXN will be much higher than in current tokamaks. Furthermore, numerical simulations predict that their energy distribution will have a high energy tail which will reach several keV [45].

Since ITER FMs will not be in direct line-of-sight of the plasma, erosion by CXN is expected to be the main physical sputtering effect.

Chemical sputtering

Carbon is currently used in most of the present operating tokamaks as a first-wall material due to its promising properties reported in subsec-

tion 1.6.2. Graphite was firstly considered to be employed for the divertor targets of ITER. In the case of C, not only physical sputtering but also chemical sputtering contributes to the global erosion under hydrogen (or hydrogen isotopes) ions bombardment. Specifically, chemical reactions between carbon atoms and incident hydrogen ions lead to the formation of volatile hydrocarbon molecules or to loosely bond hydrocarbon precursors which would be physically sputtered with a much lower threshold energy [46]. For W and Be, chemical sputtering is instead much less important.

2.3.2 Re-deposition of eroded plasma facing components

All the eroded materials have eventually to be re-deposited somewhere else in the ITER chamber. This mechanism constitutes the process of material migration. Re-deposition of eroded material may occur close to the erosion source or at remote areas. Material migration depends on eroded material properties, plasma configuration, transport properties, tokamak geometry, etc. For example, in limiter tokamaks, the erosion of limiters is the main impurity source. Most of the eroded material is re-deposited on the limiters surface due to the proximity to the confined plasma. On the other hand, in divertor tokamaks like ITER, atoms sputtered from the divertor target plates are ionized and either promptly re-deposited or transported through the divertor plasma [39], primarily under the influence of the ion temperature gradient force which drives the impurities outside of the divertor. Successively the friction with the flow of deuterium into the divertor returns the eroded material to the plates. Prompt re-deposition typically occurs for high-Z impurities which are easily ionized and have a significant Larmor radius. For these reasons they are re-deposited within the first Larmor rotation, thus reducing the gross erosion rate [47] and limiting the possibility of long-range migration of high-Z impurities. The situation is more complex in the case of C. The potential formation of neutral hydrocarbons through chemical sputtering leads to migration over long distances.

In most operating tokamaks, significant effort is devoted to understand the migration phenomenon and its implications. Among them, the retention of tritium in the re-deposited layers constitutes one of the most important concerns from the radioactive point of view. A common feature of several divertor tokamaks, and very likely of ITER, is the strong asymmetry between the inner and outer divertor legs [48,49]. The inner (outer) divertor is a region of net-deposition (net-erosion or neutral erosion/depo-

sition). Most probably the re-deposits found in the inner divertor are due to the erosion of the main chamber wall or the outer divertor and driven to the inner divertor by the large SOL flows (measured by means of Mach probes [39, 50]).

Another striking feature of many tokamaks is the relevant re-deposition of carbon and deuterium in regions shaded from ion flux but close to C surfaces which are subjected to a high ion flux [51]. Since ions cannot reach the shadowed regions, this C re-deposition can only be due to carbon (or hydrocarbon) neutrals produced by chemical erosion followed by molecular dissociation [48]. The same mechanism would not verify for metals, and hence in ITER, since they are preferentially eroded by physical sputtering as atoms which are then ionized and re-deposited on surfaces intersecting the magnetic field lines.

2.3.3 Concerns associated to first mirrors

The location of the first mirrors and the corresponding distance from the thermonuclear plasma primarily determine whether they will face erosion or re-deposition during ITER discharges. Both these phenomena will potentially lead to a dramatic decrease of FMs specular reflectivity (see appendix A.1 for basic notions of optics), posing a serious threat on the operation of the entire diagnostics [5].

Erosion of FMs by CXN or plasma ions results in an increase of their surface roughness and thereby a decrease of the corresponding specular reflectivity. A qualitative evaluation of the relation between the surface roughness of a material and its specular reflectivity at normal incidence is given by the Bennett's formula [52]:

$$R_{Spec} = R_0 \exp\left[-(4\pi R_{rms})^2/\lambda^2\right] \tag{2.1}$$

where R_{Spec} is the measured specular reflectivity, R_0 is the reflectivity of an ideally smooth surface of the same material, R_{rms} is the surface root-mean-square Roughness (expressed in nanometers) and λ is the wavelength of the incident light (in nanometers). This relation determines both a technological requirement (for the manufacturing of the FM) and a limit to FM surface roughening the diagnostic could cope with. For example, in order to guarantee that FM specular reflectivity loss does not exceed 5% of the initial specular reflectivity, a necessary condition is that R_{rms} remains lower than $\lambda/50$. It is also evident from the Bennett's formula that this limit is more restrictive in the ultraviolet (UV) and visible (vis) region of

the electromagnetic spectrum, while the specular reflectivity appears less sensitive to the surface roughness for infrared (IR) λ.

Investigations of the effect of surface roughening due to deuterium ion bombardment on the specular reflectivity of mirrors of different candidate materials (see subsection 2.3.4) were made in laboratory experiments [53, 54]. The main results are summarized in figure 2.10 [55]. The

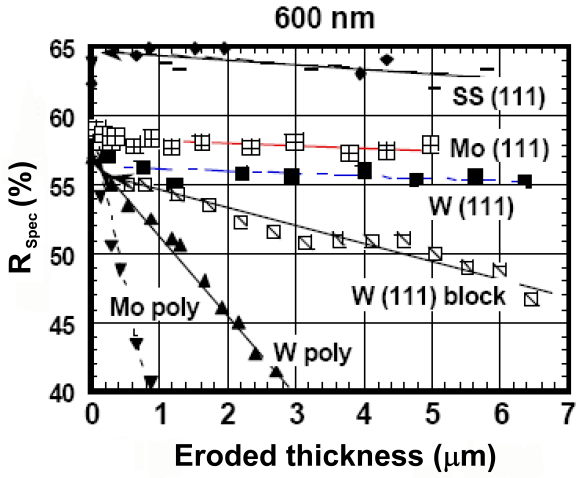

Figure 2.10: *Specular reflectivity of various first mirrors materials with different crystallographic structures at λ = 600 nm as a function of the thickness of the layer eroded by the deuterium ions [55].*

degradation of the specular reflectivity appears to be a linear function of the eroded thickness. Moreover, R_{Spec} decreasing rate (and thus the roughening increasing rate) strongly depends on the material type and its crystallographic form. In particular, polycrystalline materials exhibit a very pronounced degradation of R_{Spec} under ion bombardment. This behaviour has been attributed to the difference of the physical sputtering yield of crystallites oriented differently with respect to the surface (subsection 2.3.1). Under ion exposure the initially polished surface is transformed into a complex step relief pattern [56, 57], which reveals the morphology of the different crystallites. On the other hand, R_{Spec} degradation rate of monocrystalline mirrors is much lower, "fingerprint" of a more homogeneous sputter of the surface during ion bombardment.

If the energy of the particles impinging on the FMs surface will be below the physical sputtering threshold, FMs could become coated by a film composed by materials eroded from PFCs. As the erosion issue, also re-deposition onto FMs has been investigated by dedicated experimental

campaigns, both in tokamaks [58–63] and with suitable devices [54,64,65]. The main result is that even a re-deposited layer of few nanometers can deeply modify FM optical properties. In particular, FM reflectivity is driven by that of the contaminant film and the FM surface becomes actually invisible to the light. It is evident how relevant the re-deposition concern is in the frame of diagnostics operation of ITER. For all these reasons, the ITPA-SWG puts great efforts in order to face FMs re-deposition concern by means of active (shutters, gas blows in front of FMs, introduction of special diagnostic duct geometries, etc.) and passive (plasma cleaning, laser cleaning, etc.) mitigation techniques [19]. Albeit all these methods would permit to recover a relevant fraction of the initial specular reflectivity of FMs, their effectiveness, robustness and reliability are not yet demonstrated (see subsection 2.3.5).

2.3.4 First mirrors in ITER: materials and configurations choice

Since its establishment during 2000s, the ITPA-SWG has given high priority to the choice of ITER FMs materials and configurations [37]. Following the previous considerations, the main requirements that a material has to satisfy to be considered as a candidate for FMs production are:

- high specular reflectivity in the operational wavelength range,
- chemical stability in the specific ITER environment,
- stability under high neutron fluxes (i.e. no transmutation),
- high thermal conductivity (for efficient cooling),
- low sputtering yield Y,

together, of course, with an adequate workability and low price. The set of materials which, at least to some extent, match all these features is really narrow. The most studied options are: copper (Cu), stainless steel (SS), tungsten (W), molybdenum (Mo) and rhodium (Rh). Their total reflectivity in the λ range of 250-2000 nm, calculated using the optical constants indicated in [6], is shown in figure 2.11. Each of these materials owns interesting advantages and drawbacks. SS is a relatively well-know material with good chemical and neutron properties, it is easy to manufacture but has a rather low total reflectivity. Cu has a very high reflectivity for $\lambda > 500$ nm but very low below and it is also sensitive to sputtering. W and Mo are high-Z materials with low Y by deuterium; their total reflectivity is however not so high. Among the different candidate materials,

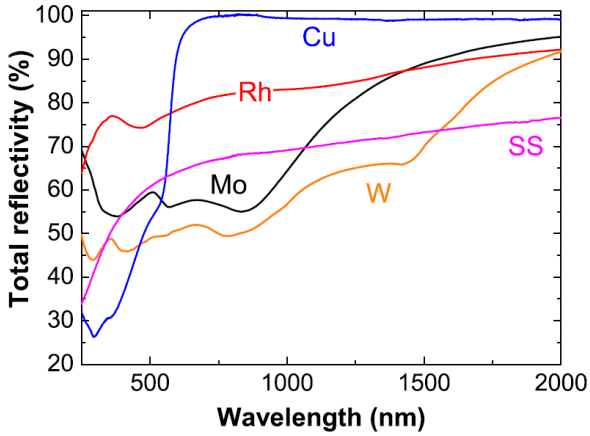

Figure 2.11: *Total reflectivity of the different candidate materials for ITER first mirrors, calculated using the optical constants indicated in [6].*

Rh seems to be the most promising material thanks to its high Z, high total reflectivity in a wide wavelength range and acceptable Y [66]. The main drawback is constituted by its high price as a raw material.

Various FMs configurations have been investigated so far, including polycrystalline, monocrystalline and nanostructured thin film mirrors [37]. The former choice appears to be the simplest solution in terms of cost and availability of the production techniques. However, as just pointed out in subsection 2.3.3, polycrystalline mirrors develop a complex step relief pattern when eroded by thermonuclear plasmas [56, 57]. A monocrystalline mirror or a mirror composed of crystallites with nanometric size should guarantee a more uniform erosion during ITER operation (the surface relief pattern would remain small with respect to the wavelength of the reflected light, thus ensuring a low diffuse reflectivity) and ultimately a more reliable diagnostic. In particular, it has been shown in laboratory experiments that W and Mo monocrystalline mirrors may actually preserve their specular reflectivity after the erosion of a superficial layer several microns thick [53]. However, since both high production costs and technical difficulties prevent the fabrication of monocrystalline mirrors with diameters (Ø) larger than 10 cm (ITER FMs Ø up to 50 cm [3], see sections 2.1 and 2.2), thin film technologies can offer a cheaper and feasible solution for ITER FMs manufacture. The choice of the best process for the deposition of FMs coatings thus arises. Specifically, it should guarantee that the specular reflectivity of the films maintain the same values as those of the corresponding bulk material. Moreover, good thermo-mechanical prop-

erties (i.e. high adhesion to the substrate, acceptable behaviour under ITER-relevant heat loads, etc.) of the coatings need to be ensured.

Considering rhodium, the high price as a raw material makes the thin film configuration almost mandatory. Rh coatings have been mainly produced by electrochemical deposition [67,68], electron beam evaporation [69] and magnetron sputtering [70, 71]. The former shows problems in the reproducibility of the method and the specular reflectivity of Rh coatings is lower than the reference values. While the promising results obtained by means of electron beam evaporation and magnetron sputtering, they find some limits in properly controlling film nanostructure and achieving at the same time satisfactory behaviour at high temperature.

In 2010, the Micro- and Nanostructured Materials Lab (NanoLab) of Politecnico di Milano started a novel research devoted to the production of Rh films functional for FMs by Pulsed Laser Deposition (PLD, see appendix B for a detailed description of the technique) [72]. This is one of the well-known vapour phase deposition processes for manufacturing ceramic and metallic thin films [73]. The main PLD advantage with respect to the other deposition techniques is its capability to tailor film properties at the nanoscale. By varying the main process parameters like laser energy, background gas nature and pressure, etc., it is possible to select the morphology and the nanostructure of the growing film [73–75]. As far as FMs production is concerned, this accurate and tiny control could permit, in principle, to optimize Rh films behaviour under ITER plasma erosion. However, intrinsic PLD drawbacks such as the non-uniform and heterogeneous nature of the deposit, the particulate and droplets production onto its surface and the stress relaxation concern for thick films, still represent open issues to be addressed in order to obtain Rh films with satisfactory optical and mechanical properties, suitable for ITER FMs. The first part of this Ph.D thesis, chapter 3, will be indeed devoted to deal with all these concerns. In chapter 4, PLD Rh films erosion properties will be also investigated.

2.3.5 How to mitigate first mirrors re-deposition concern

As pointed out in subsection 2.3.3, re-deposition onto FMs will dramatically influence their performance during ITER plasma pulses. In the following, the main features of contaminants recovered from the operating tokamaks and those expected in ITER will be presented, together with the most important techniques currently under consideration to prevent and mitigate ITER FMs re-deposition concern.

Main characteristics of tokamaks re-deposits

The high complexity of the transport phenomena in plasmas and the manifold functional differences between the nowadays tokamaks determine a great fan of re-deposited materials. It is clear that their features are strictly related to those of the considered tokamak first-wall which is eroded by the thermonuclear plasma. As previously discussed, a fraction of the functioning tokamaks, like Tore Supra (from the French words of torus and superconductor, Cadarache, France), still works with an all-C wall. Moreover, most of the others also operated with C as PFC during their history. Two examples are JET before the start of the ILW project (1994-2009) and ASDEX before the upgrade (1980-1990). For these reasons, the information about tokamaks re-deposits available from literature refers mainly to C contaminants. From 1991 ASDEX-U began to work with an all-W wall. The solution of W for the divertor plates was also adopted in Japan Torus-60 Upgrade (JT-60U, Naka, Japan). During 2010 JET was converted to an all-metal device. The ILW configuration comprises of Be in the main chamber and W in the divertor. Since the materials choice is the same as ITER, this project aims to help to faithfully predict ITER behaviours.

It is evident that carbon, tungsten, beryllium and hydrogen (or its isotopes) are the main constituent materials of the re-deposits recovered from tokamaks. Depending on the geometrical structure of the fusion device, on its magnetic fields configuration and on the associated impurities migration properties, the main re-deposits characteristics, i.e. morphology, chemical nature and nanostructure, vary from tokamak to tokamak and are also different considering various regions inside a single tokamak. It is otherwise possible to identify some recurrent re-deposits: low adhered compact films and contaminants with a very open morphology.

Considering the all-C JET tokamak, a wide investigation of the cross-section of re-deposits formed onto PFCs of the inner divertor (which, as observed in subsection 2.3.2, is a typical region of net re-deposition) by Optical and Scanning Electron Microscopy (OM and SEM, respectively) has been reported in [76]. The re-deposits showed a compact morphology and, specifically, three peculiar configurations are visible: columnar, lamellar and globular. The former indicates structures with prominent features nearly perpendicular to the surface of the re-deposit. Lamellar means layer structures with visible stratified sub-layers parallel to the surface of the re-deposit. Finally, globular indicates all the layer structures that look more disordered, but often shows more or less circular spots. An

example of a SEM cross-section image of a re-deposit displaying columnar structure is reported in figure 2.12a. Columnar layers were found also in Tokamak EXperiment for Technology Oriented Research (TEXTOR, Jülich, Germany) [77] and in Tore Supra [78]. The columnar configuration is usually explained in the framework of the structure zone model as ballistic aggregation in case of low surface mobility of the re-deposited material, which is assumed to arrive preferentially from some direction [79]. Figure 2.12b shows an optical image of a layer retrieved from a shadowed

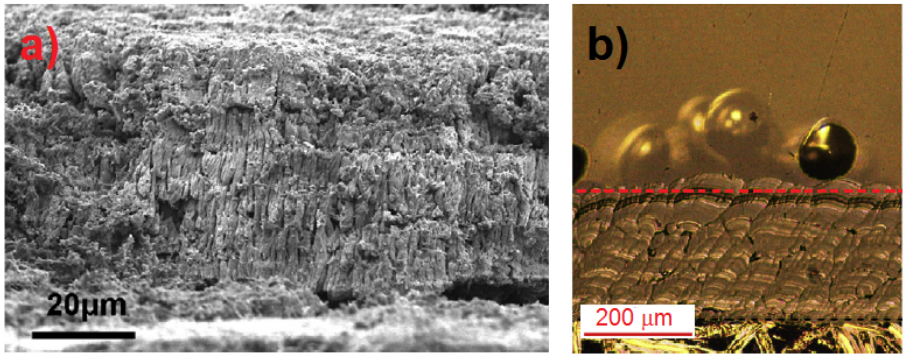

Figure 2.12: *SEM (a) and OM (b) cross-section images of typical re-deposits found on the inner divertor of the all-C JET [76].*

region of the inner divertor. There is a prominent line in the image, which helps orienting it. Approximately below that line the layer looks lamellar, whereas it is globular above.

The all-C JET re-deposits considered so far are mainly composed by carbon, hydrogen and beryllium (often vapour deposited in all-C JET for wall-conditioning). Their chemical nature and stoichiometry strongly depend on the analyzed region of the inner divertor.

Analogous results were obtained, again in the all-C JET, by the First Mirror Test (FMT) [59–61]. On the request of the ITER design team, this experiment was devoted to investigate the impact of a long-term exposure in a tokamak on the specular reflectivity change of possible candidate materials for ITER FMs. Some specimens were located in the divertor region and the others on the main chamber. As expected (see subsection 2.3.2), the surface state of mirrors in the divertor was governed by net-deposition, whereas net-erosion decided the state of mirrors located close to the plasma on the main chamber wall. As for [76], compact re-deposits were found on mirrors in the divertor region. In particular, SEM top-view images of figure 2.13 show the presence of flaking re-deposits

onto them. In figure 2.13a, one observes a stratified structure of the layer (lamellar), which peeled-off, thus forming terraces and areas of diversified re-deposit thickness. Flaking and poor adherence to the mirror, as can be judged from figure 2.13b, indicate that, during the entire period of exposure to the JET plasma, many consecutive layers could peel-off thus contributing to the formation of particulate which could re-deposit and finally aggregate bringing to the growth of contaminants with an open morphology.

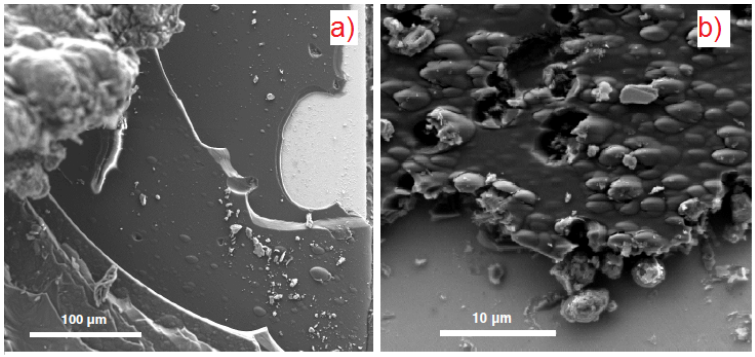

Figure 2.13: *SEM top-view images of compact re-deposits found on mirrors placed in the all-C JET divertor in the frame of the first mirror test [61].*

The formation of compact re-deposits with a stratified structure is not a peculiarity of C-based tokamaks. They were also observed in a full-metal device as ASDEX-U [80]. In this case, the main constituent material was clearly W. However, traces of C were revealed in the first re-deposited layers, residuals of the experimental campaigns performed before the upgrade.

Besides compact re-deposits, the formation of particulate, commonly referred to as dust, which does not adhere to surfaces and is capable of being mobilized, is also very common in nowadays fusion plasma research devices [81]. As far as the mechanisms of dust generation are concerned, today it is widely believed that the main source of dust in C-based tokamaks is due to the flaking of re-deposited films. However, analysis of the structure of dust collected from different fusion devices indicates that other mechanisms, such as volumetric and surface growth of dust grains (via nucleation, coagulation and condensation processes [82]), plasma off-normal events (which cause surface melting and droplets production), etc., also contribute and may even dominate in machines with all-metal PFCs [83]. The different mechanisms described so far bring to the formation of dust

with various shapes and characteristic sizes, as shown in figure 2.14. In

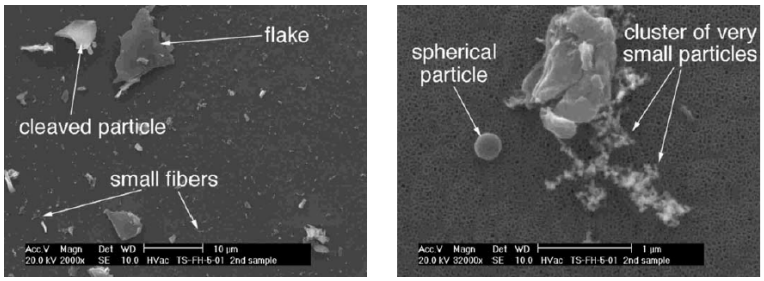

Figure 2.14: *SEM top-view images demonstrating various shapes of dust collected from tokamaks [81].*

particular, the growth of dust grains could determine the formation of films with a very open-morphology (also called "quasi-film" in the following). This is a typical low-energy process which could verify in regions not in direct contact with the plasma, as the ducts where some of the ITER FMs will be allocated. The topic of how re-deposited "quasi-films" will impact on FMs optical properties and hence on the performance of ITER diagnostics is therefore particularly relevant.

Mitigation and cleaning techniques

To face ITER FMs re-deposition concerns, various mitigation techniques have been investigated so far by the ITPA-SWG. The most promising are: shutters, gas blows in front of mirrors, temperature treatments and introduction of special diagnostic duct geometries. These are also known as active mitigation techniques. Whenever possible, they should be simultaneously applied to further reduce risk and enhance mirrors performance and lifetime. *In-situ* mirrors cleaning systems (called passive mitigation techniques) should be included in the diagnostics design. Given the uncertainties of the present predictions it seems wise to develop cleaning solutions not only for the case that the main toroidal field is switched off but also for the case that it is still on [19]. Presently, laser cleaning and plasma cleaning techniques are under assessment. In plasma cleaning, contaminants removal would be accomplished directing a Radio-Frequency (RF) or Direct Current (DC) plasma source towards the FM. However, all known plasma-etching techniques for thin films removal, widely applied in the semiconductor and optical industries, usually utilize knowledge of the composition and morphology of the etched material. Consequently, their eligibility for ITER purposes is not straightforward [84]. Furthermore,

substances containing chlorine and fluorine, commonly employed for etching, are unsuitable in ITER. Conventional methods based on gasification of thin films by oxidation (heating or discharge in oxygen) [85], are also not appropriate due to possible in-vacuum facility damage. Plasma cleaning techniques without activators, which would unfavourably affect ITER plasma discharge or PFCs, are the main priority of the current research.

The other possibility consists in exposing ITER FMs surface to a train of laser pulses with suitable properties, in terms of laser wavelength, spatial and temporal profiles, spot size and energy, in order to remove the re-deposited material with high efficiency and in the meantime preventing FMs surface from damage. Its main advantages are accurate focusing, high efficiency, remote and "on-line" operation. Besides these encouraging features, the principal drawback consists in the high sensitivity of this technique to mirror material and configuration, to the nature of the redeposit and to the laser source parameters, which results into the lack of a systematic approach to the concern of FMs cleaning from ITER contaminants [86–89].

Since during this thesis, great efforts were made to investigate the potentiality of the laser cleaning technique in the frame of the mitigation of ITER FMs re-deposition (chapter 5), its state-of-the-art will be briefly described in the next subsection.

2.3.6 Laser cleaning for ITER first mirrors

Laser cleaning has been widely used to clean ancient stones, metals and painted artifacts [90], semiconductor substrates employed in microelectronics [91] and, in nuclear fission industry, to decontaminate surfaces [92]. In the field of magnetic confinement nuclear fusion, it has been firstly exploited to detritiate [93, 94] and remove re-deposits, either retrieved from tokamaks [95–98] or faithfully reproduced in laboratory facilities [99–103], from PFCs. Considering the optical elements of nowadays nuclear fusion devices, the laser cleaning removal of contaminants re-deposited onto optical windows has been investigated [104–106]. Clearly, as for the first mirrors, the re-deposition phenomenon negatively affects the optical properties of these components, thus bringing to the malfunctioning of the corresponding diagnostics. Unlike FMs, the low windows absorption moves the damage threshold for laser irradiation to higher energies of the laser pulses permitting a more efficient contaminants removal through energetic pulses.

Application of laser cleaning to mirrors candidate as ITER FMs is still

at a preliminary stage [86–89]. One of the most important concerns is to guarantee the high FMs performances required for ITER. A possible damage due to laser irradiation could bring to an unacceptable value for the roughness of the FM surface and thus to a dramatic decrease of its specular reflectivity (see Bennett's formula 2.1). This will impose a superior limit to the energy and number of laser pulses that the FM could withstand, influencing therefore re-deposits cleaning efficiency [88]. The high sensitivity of laser cleaning technique to mirror material and configuration, to the nature of the re-deposit and to the laser source parameters, constitutes another important issue. The different features of contaminants re-deposited onto FMs located in different regions of ITER will require the optimization of the laser cleaning process parameters on a case by case basis.

The feasibility modelling assessment of cleaning of polycrystalline Mo and Rh mirrors from C compact re-deposits of different thicknesses (10 nm, 100 nm, 1 μm and 10 μm) by Nd:YAG laser system (λ = 1064 nm, 100 ns pulse duration, 20 kHz repetition rate) showed that a complete removal of C contaminants is possible for sufficiently thick films [65]. However, assuming a non-perfect thermal contact between the metal substrate and the re-deposit, for thin contaminant films it is still possible to reach the ablation temperature of C re-deposit without damaging the substrate. The removal of extremely thin films (1-5 nm thick) is nevertheless a problem, since the laser damage threshold for the film and the mirror is nearly the same under these conditions.

These findings were partially confirmed by laser cleaning dedicated experimental campaigns which showed that even with a re-deposit of some microns, its complete removal from the mirror surface is hard to achieve. This is probably due to the fact that laser cleaning was mainly applied to mirrors exposed in tokamaks. The considered re-deposits were far from being composed exclusively of C. The different chemical nature of the contaminants, together with possible intermixing between the impurity species and mirrors surface, dramatically influences the efficiency of the laser cleaning technique.

In [86], polycrystalline SS and Mo mirror samples (two types: 1×1×1 cm^3 cube with one flat polished surface and the second a 45° polished surface extending from the basic cubic shape), exposed in all-C JET in the frame of the first mirror test campaign (subsection 2.3.5), with compact deposits of up to a few hundred nanometers in thickness and with Be to C ratios ranging from 0 to ∼1, were cleaned using an ytterbium fiber laser (λ = 1064 nm, pulse duration 200 ns, energy per pulse 1 mJ, repetition rate

20 kHz, near Gaussian beam). To prevent substrate damage, bare SS and Mo mirrors were exposed to the laser beam and their laser damage threshold, i.e. the laser fluence (which is the ratio between the energy per pulse and the laser spot area) at which damage occurs on the mirror surface, was evaluated. In particular, it was 2.26 J/cm^2 for SS and 6.46 J/cm^2 for Mo for one laser pulse. The effect of multiple laser pulses incident on the same spot was also investigated. It was clearly found that the threshold for multiple laser pulses at a particular spot was lower due to a higher integrated fluence. The "one-pulse" damage threshold determined experimentally defined the maximum laser fluence to which the mirrors were exposed during the cleaning trials. For SS and Mo mirrors the ranges of laser fluence used were 1.17-2.25 J/cm^2 and 2.80-6.34 J/cm^2, respectively. Despite this conservative approach, the surface of mirrors exposed in JET was damaged after the cleaning procedure. This was probably due to the contaminant-mirror coupling that potentially modified mirror laser damage threshold. Following laser cleaning, the recovered total reflectivity was generally better in the infrared than in the visible spectrum, with recovery up to 90% of the initial total reflectivity being obtained at $\lambda = 1600$ nm for both Mo and SS mirrors, falling as low as 20-30% of initial total reflectivity at $\lambda = 400$ nm for some SS samples, rising to $\sim$80% for Mo mirrors. However multiple laser scans across the surface of the mirrors, it was not possible to remove all the re-deposits from them. The loss in reflectivity was more likely due to the remnant contaminant thin films (this agrees with the modelling results previously presented [65]) rather than to the damage of the mirrors. The latter should have determined a decrease of the specular reflectivity as a consequence of the rise of diffuse reflectivity due to mirrors surface roughening. Since the total reflectivity measured is the sum between specular and diffuse reflectivity (appendix A.1), it was not influenced by laser damage of the mirrors.

Besides JET activities, a polycrystalline Mo mirror with an area of 20×20 mm^2 was exposed in Huan-Liuqu (Chinese words stand for toroidal current device) 2A (Advanced) tokamak (HL-2A, Chengdu, China) and cleaned with a Q-switched Nd:YAG laser ($\lambda = 1064$ nm, pulse duration 10 ns, maximum output energy per pulse 100 mJ, laser spot diameter 5 mm, pulse repetition rate 1-10 Hz, near Gaussian beam) [87]. A C re-deposit 1 μm thick was found onto the mirror. The evaluated laser damage threshold was 1 J/cm^2 and the cleaning procedure was performed with a fluence per pulse of 0.645 J/cm^2, was well below the damage threshold. The C re-deposit was almost completely removed by multiple pulses repeated spatial scans. After the cleaning procedure, Mo mirror specular reflectivity was

recovered over 90% in the infrared regime. At UV-vis λ the cleaning results were not satisfactory, probably due to promptly deposition of the ablated matter and possible increase of uneven surface.

One of the most important attempts to extend the application of the laser cleaning technique to the case of high reflective films functional for ITER FMs is reported in [89]. The laser damage threshold of polycrystalline SS, nanocrystalline Rh and mono-, poly- and nanocrystalline Mo mirrors (both Rh and Mo nanocrystalline films were deposited by magnetron sputtering [69–71] onto SS substrates), at a number of wavelengths between 220 nm and 1064 nm, was determined using a commercial optical parametric oscillator system delivering tuneable, polarized laser radiation between 210 nm and 2300 nm (pulse duration 5 ns, pulse energies between 1.5 mJ and 35 mJ depending on λ, pulse repetition rate 20 Hz). Samples were on the order of 20-25 mm and either round or square depending on material. All the mirrors showed an increase of the damage threshold with decreasing the wavelength below 400 nm. In the case of Rh films, the laser damage threshold was $\sim$300 mJ/cm^2 for λ = 1064 nm and 532 nm, and $\sim$700 mJ/cm^2 for λ = 266 nm. Cleaning tests were performed on SS samples after applying different mixed aluminum/tungsten/carbon/deuterium coatings (with aluminum as Be-proxy, since Be is highly toxic and thus requires dedicated laboratory facilities for its handling) using magnetron sputtering. A substantial recovery of the specular reflectivity was obtained for each mirror, despite relevant differences in the composition of the contaminant films. Results so far indicate that UV irradiation (e.g. with 230 nm) following visible irradiation (e.g. with 532 nm) can significantly enhance the cleaning efficiency compared to the cleaning using a single wavelength. This is primarily due to the fact that different wavelengths imply different physical and chemical mechanisms involved in the interaction between the laser pulses and the irradiated material.

The discussion presented so far highlights the necessity of conducting further experimental trials in order to better understand the physics underneath the cleaning by laser pulses and to identify suitable process parameters regimes which permit to obtain a high cleaning efficiency preserving also the integrity of the FMs surface. As described, in literature the experimental investigations lean against two different strategies. The first consists in cleaning mirrors exposed to tokamaks plasma. In this case, the re-deposited material closely resembles that expected in ITER. However, it is not possible to control the nature of the contaminant and hence directly analyze the impact of a re-deposit feature variation onto the physics of the laser cleaning process. Furthermore, the chances of

exposing mirrors in operating tokamaks are not so high due to logistic issues. The second approach is represented by the possibility of reproducing "tokamak-like" contaminants in laboratory facilities exploiting the well-known deposition techniques (chemical vapour deposition methods, magnetron sputtering, PLD, etc.). This solution permits to take advantage of their flexibility to pre-determinately select the features of the deposited contaminants. Chapter 5 will be indeed devoted to present a novel approach to the process of Rh films production-contamination-cleaning, in which the same laser source is exploited to experimentally investigate ITER FMs re-deposition concern with laboratory-scale facilities.

2.4 Objectives of the thesis

2.4.1 Thesis subjects

This Ph.D thesis is an experimental work, mainly conducted at the Micro- and Nanostructured Materials Lab (NanoLab) of Politecnico di Milano. It is developed within the frame of an active collaboration between NanoLab and Istituto di Fisica del Plasma, Consiglio Nazionale delle Ricerche, EURATOM-ENEA-CNR Association. This Ph.D work has a twofold goal. **A)** The first objective is the production and investigation of rhodium (Rh) films for ITER First Mirrors, FMs (Part II). **B)** The second objective consists in a preliminary study of the laser cleaning technique as a potential method to mitigate the re-deposition of ITER first-wall eroded material transported in the plasma onto FMs surface (Part III).

A) The production of Rh coatings for FMs by means of Pulsed Laser Deposition (PLD, subsection 2.4.2 and appendix B for a presentation of this technique) is firstly addressed. Preliminary results already reported in literature are promising and encouraging [72]. By suitably changing the process parameters, PLD allows morphology and nanostructure control of the growing film in a peculiar manner with respect to the other deposition techniques, like electrodeposition and magnetron sputtering. However, with the aim of exploiting PLD for the development of suitable solutions for realistic ITER FMs based on a high reflective Rh coating, it is necessary to face some PLD drawbacks in a systematic way. First of all, films obtained by PLD have often non-uniform thickness and heterogeneous properties. This shortcoming becomes particularly important as far as the production of mirrors is concerned, because they need to be highly planar and homogeneous in order to have a high specular reflectivity on the whole

surface. Another relevant PLD issue is the presence of particulate and droplets of various geometrical shapes and dimensions, typically with a diameter lower than 0.5 μm or in the range 1-3 μm [107], on the surface of the deposited films. Micrometric droplets could determine a critical increase of the diffuse reflectivity of the films. The production of sufficiently thick films is also necessary to face the problem of erosion of FMs during ITER operation. In this context, it is crucial to consider the fundamental aspect of film-substrate adhesion, to avoid buckling and delamination phenomena in the coating, caused by internal stresses. In chapter 3, the solutions adopted to overcome the main PLD drawbacks reported above in order to obtain Rh films with realistic properties for ITER FMs, like a high specular reflectivity on a significant side area (up to 10 cm^2) and satisfactory mechanical properties of thick (up to 5 μm) films, will be discussed.

As described in subsection 2.3.4, a mirror composed by crystallites with nanometric size should avoid the formation of a complex relief pattern when eroded by the ITER plasma thus ensuring a more uniform erosion. However, the behaviour of nanocrystalline film mirrors in erosion-dominated zones as a function of their morphology and crystal structure still constitutes a major open issue. The distinctive PLD feature of tailoring films properties at the nanoscale was successfully exploited to produce Rh films with different morphology, crystallographic orientation and mean crystallite size, and their performances under erosion of a laboratory pure deuterium plasma with some qualifying features relative to the ITER peripheral plasma facing first mirrors, were deeply investigated. This experimental campaign was developed in collaboration with the Nanolino group at the Physics Department of Basel University (November 2012). Since Nanolino group has far back launched an activity for the production of Rh films by magnetron sputtering functional for FMs [70, 71], the investigation of Rh films properties under pure deuterium plasma exposure was also extended to a magnetron sputtered Rh sample. Chapter 4 will present the results of this campaign.

B) In order to perform a first study of the laser cleaning technique as a potential method to mitigate the re-deposition of first-wall eroded materials onto FMs, a novel approach to the process of Rh films production-contamination-cleaning, in which the same laser source is exploited to experimentally investigate ITER FMs re-deposition topic with laboratory-scale facilities, was developed. In detail, this

method consists in three steps: (i) production by PLD of Rh film mirrors, (ii) production by PLD of deposits with characteristics as close as possible to those recovered from the operating tokamaks and those expected in ITER, and (iii) investigation of the laser cleaning technique onto PLD Rh films contaminated with PLD "tokamak-like" re-deposits. The development of this novel and integrated approach to the problem of ITER FMs re-deposition, together with the relative results achieved, will be reported in chapter 5.

The study of the most recurring features of tokamaks re-deposits from literature (subsection 2.3.5) was also completed with a work, performed in the frame of a three months period at the JET tokamak (July-October 2013), of post-mortem characterization of JET first-wall PFCs (also known as tiles) extracted after the 2011-2012 experimental campaign. Among the post-mortem characterization techniques, tiles profiling permits to evaluate the erosion and re-deposition pattern of JET tiles on a macroscopic scale. To solve the main concerns associated to this method, an interpretative tool (i.e. MatLab routine) for tiles profiling measurements was developed. The description of the code and the main results obtained from its application to JET tiles extracted from 2011-2012 experimental campaign, will be discussed in chapter 6.

2.4.2 Experimental methods of this thesis

In this section, the main experimental apparatus, the approaches and the methods exploited for developing the novel approach to the process of Rh films production-contamination-cleaning, will be described. As mentioned in the previous section, both the production of Rh films and their contamination with tokamak-like re-deposits were performed employing pulsed laser deposition technique. PLD in one of the well-known vapour phase deposition processes for fabricating ceramic and metallic thin films. In PLD a target of the material to be deposited is placed in a vacuum chamber and is exposed to energetic laser pulses. After the interaction with a laser pulse, the surface of the target firstly melts and successively ablates. The vaporized particles expand in the vacuum chamber, assuming the classical shape called "plume", towards a substrate placed in front of the target, thus determining the growth of a film above it. A general overview of this technique is given in appendix B. In this subsection, the PLD apparatus exploited in the frame of this Ph.D thesis will be presented.

The Micro- and Nanostructured Materials Lab exploits two indepen-

dent PLD systems. The one employed in this work (figure 2.15) consists of a solid-state laser source, mirrors and optics to point the laser beam towards the deposition chamber, a cylindrical deposition chamber, a conventional pumping system and a flexible motors system for the motion of both the target and the substrate. The laser source is a solid-state

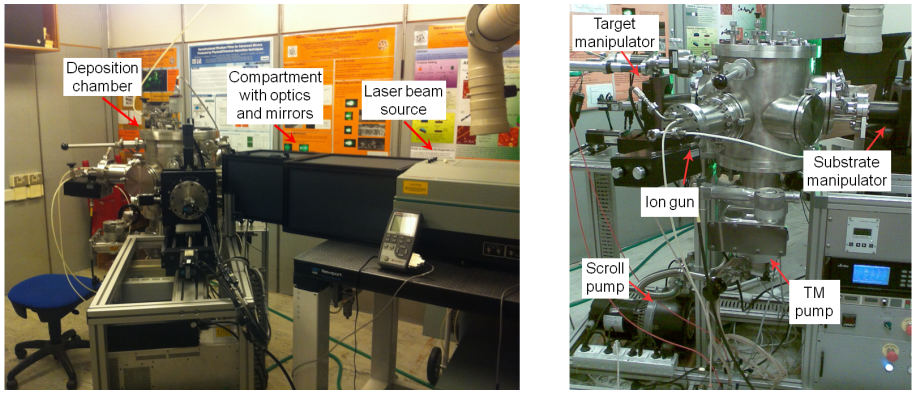

Figure 2.15: *Two photographs of the PLD system employed in the frame of this Ph.D thesis.*

Nd:YAG (neodymium-doped Yttrium Aluminum Garnet) laser. This system (Continuum Powerlite II 8010) permits to generate laser pulses at the fundamental wavelength $\lambda = 1064$ nm (IR) with duration 5-7 ns and maximum energy per pulse 1800 mJ. The laser pulses are produced by Q-switching through an electro-optical device. The maximum pulse repetition frequency is 10 Hz. Non-linear crystals are available and allow to frequency-double, -triple, and even -quadruple the fundamental Nd:YAG laser pulses, which have wavelengths of 532 nm (green), 355 nm (blue/UV) and 266 nm (UV), respectively. The laser spot presents a circular beam profile with a diameter of 9 mm. If necessary, the laser pulses are focused by a plano-convex lens (different for each laser wavelength employed), before entering the deposition chamber. The ablated target is placed within the focal length of the lens. Moving the lens through a suitable rail, it is possible to focus and defocus the laser beam, thus determining a variation of the laser fluence per pulse, i.e. the ratio between the energy per pulse and the laser spot, impinging on the target.

The deposition chamber is a cylindrical stainless steel chamber, with height and radius of 40 cm. It foresees a series of flanges allowing the access of different analysis instruments (like the quartz microbalance) and other useful components (e.g. the ion gun). Viton o-rings are employed to connect the different flanges.

Inside the deposition chamber, both target and substrate are fixed to suitable holders, placed opposite each other and locked to two manipulators (figures 2.16a and b, respectively). Each manipulator permits at least three degrees of freedom: translation along the vertical direction, translation along the direction parallel to the target (substrate) axis and rotation around the target (substrate) axis. All these motions are coordinated by stepper motors whose operation is controlled by a suitable software. The two motors acting along the direction parallel to the target and substrate axes allow the change of the distance between target and substrate. Target motors system has been also exploited to elaborate a properly optimized spiral motion which guarantees the uniform ablation of the target during the deposition process. Substrate manipulator permits to manually shift the horizontal position of the substrate holder. As it will be clear in chapter 3, the possibility of modifying the horizontal position of the substrate plays a crucial rule in the frame of the deposition of planar and homogenous films on wide areas (some cm^2).

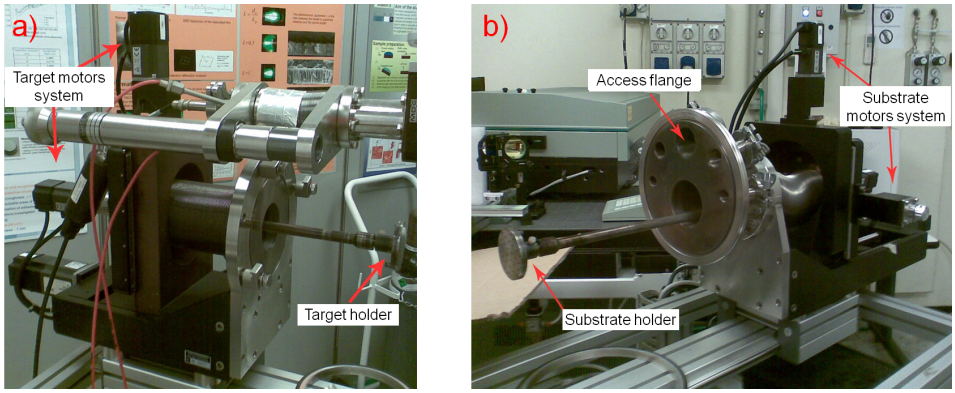

Figure 2.16: *Photographs of the target (a) and substrate (b) manipulator systems.*

The geometry of this PLD apparatus was chosen in such a way that the angle of incidence of the laser beam onto the material target is 45°, thus minimizing the risk of laser beam reflections directed towards the laser box which could compromise the integrity of the non-linear crystals. The scheme of the PLD apparatus employed is reported in figure 2.17a.

The pumping system allows to reach a high-vacuum regime (up to 10^{-4} Pa) inside the deposition chamber. It is constituted by a scroll and a TurboMolecular Pump (TMP). The scroll pump works under viscous flow conditions and depressurizes the chamber to ∼10 Pa. Once the "primary" vacuum is established, the TMP brings the system to the nominal

pressure of 10^{-4} Pa under molecular flow conditions. The pressure of the deposition chamber is controlled by two pressure measurement devices: one capacitance gauge and one full range Pirani and Bayard-Alpert sensor combination gauge (operation intervals 10^{3}-10^{-1} Pa and 10^{5}-10^{-4} Pa, respectively). The injection of a gas into the deposition chamber is possible thanks to a suitable flow-meters system, directly connected to the corresponding gas cylinder. This apparatus permits to regulate the gas flow with an accuracy of 0.1 sccm (standard cubic centimeter per minute) and to maintain an exact gases flows ratio in the case of operation with a mixture of two or more gases. Pressure control is achieved through a balance between the action of the TMP and the injected gases flows into the chamber. This control permits to obtain gases pressures in the range 10^{2}-10^{-1} Pa.

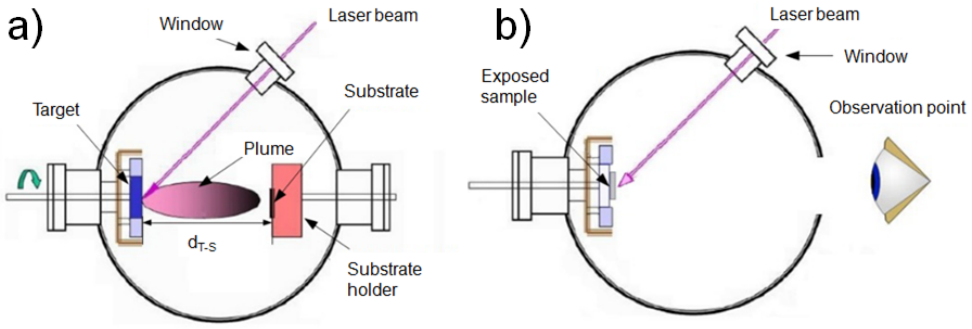

Figure 2.17: *Apparatus configuration for the production of Rh films and tokamak-like contaminants (a). Scheme for the laser cleaning process (b).*

The main PLD advantage with respect to the other deposition techniques is its capability to tailor film properties at the nanoscale. By varying the main process parameters such as buffer gas type and pressure, substrate temperature, laser wavelength, laser fluence per pulse, laser repetition rate, chemical composition and structure of the target and substrate, and target to substrate distance (d_{T-S}), it is possible to tune the energy of the ablated species thus choosing the morphology and the nanostructure of the growing film. This PLD peculiar feature was exploited to deposit compact Rh films and tokamak-like contaminants with different morphologies, from compact to highly porous. Moreover, in order to employ the laser cleaning procedure, the PLD apparatus was properly modified, substituting the PLD target with the sample that has to be cleaned and removing the substrate holder. The corresponding experimental setup is shown in

figure 2.17b. By a tempered glass flange placed in the upper part of the system chamber, it was possible to monitor by visual inspection the laser cleaning process.

Part II

Production and investigation of rhodium films

3

Production of nanostructured rhodium films by pulsed laser deposition

In this chapter the advances achieved in this thesis on the deposition by Pulsed Laser Deposition (PLD) of Rh films with suitable properties for First Mirrors (FMs) production will be described.

As discussed in subsection 2.3.4, NanoLab started in 2010 a novel research devoted to the production of Rh films functional for ITER FMs by PLD [72]. By suitably changing the process parameters, it was possible to deposit compact Rh films with different morphologies and crystal structures. In particular, two peculiar films, which could potentially determine an improvement of Rh films performance under ITER plasma erosion (see chapter 4), were obtained: a highly-oriented (preferential growth direction (111)) polycrystalline film (called also columnar in the following, because its SEM cross-section shows a columnar morphology, figure 3.1a) and an amorphous-like film (figure 3.1b) deposited in high-vacuum (3×10^{-3} Pa) and helium atmosphere, respectively. The average crystallite size (calculated from XRD spectrum by means of the Scherrer's formula [108]) of the highly-oriented film is in the range 10-20 nm while, depending on the deposition parameters, the mean crystallite size of the amorphous-like film is below 10 nm.

Despite the promising results reported in [72], the deposition of Rh films with suitable properties for the employment as FMs imposes to deal with some intrinsic PLD drawbacks. These are: non-uniform and heterogeneous nature of the deposit, the particulate and droplets production onto its surface, film-substrate adhesion and stress relaxation concern for thick coatings. The approaches adopted in the frame of this Ph.D thesis

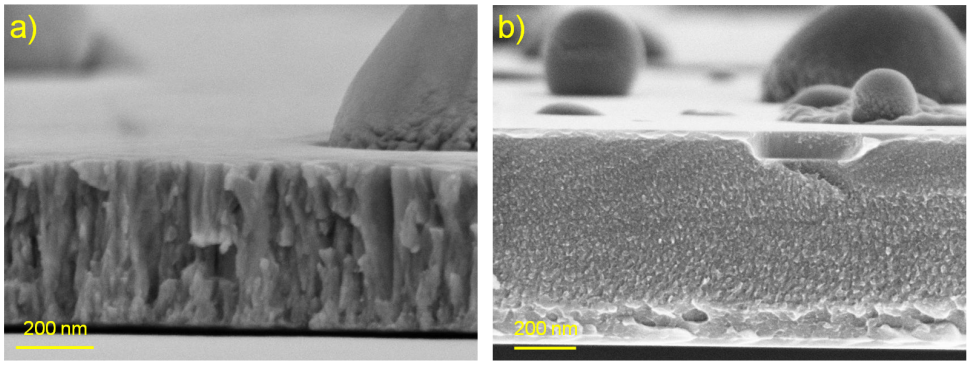

Figure 3.1: *SEM cross-section images of highly-oriented polycrystalline columnar (a) and amorphous-like (b) Rh films [72].*

to face all these concerns will be described in this chapter.

The depositions were performed using a 1 in. Rh target (purity 99.9%). The strategy followed to obtain homogeneous planar Rh films on a relevant side area (up to 10 cm^2) with high specular reflectivity will be described in section 3.1. A method to obtain relatively thick films (up to some μm) with good adhesion to a suitable substrate will be presented in section 3.2. Finally, section 3.3 will give an estimation of the capability to produce, by PLD, Rh films suitable for the requests of ITER [3].

3.1 Deposition of high reflective rhodium films on relevant areas

The development of a deposition technique for the production of FMs coatings of actual interest demands for the possibility to obtain films with a high specular reflectivity on a significant side area. Due to the dimension of the ablation source and the narrow angular distribution of the plume species, films grown by PLD often present non-uniform thickness and heterogeneous properties. The conventional scheme of a PLD deposition and the shape of the resulting film are reported in figure 3.2a. This shortcoming becomes particularly relevant in the frame of mirrors production, because they need to be highly planar and homogeneous in order to have a high specular reflectivity on the whole surface. There are many ways to potentially overcome the issue of films inhomogeneity [109]. In this work, the so-called "off-axis" deposition technique [73] was exploited. As shown in figure 3.2b, the rotating substrate axis is shifted with respect to the plasma plume axis (i.e. the direction along which the ablation rate is

maximum) by some length d, that depends on various parameters such as the material to be deposited, the distance between target and substrate (d_{T-S}), the substrate dimensions and the angular distribution of the evaporated species in the plasma plume. In this way, the main fraction of the

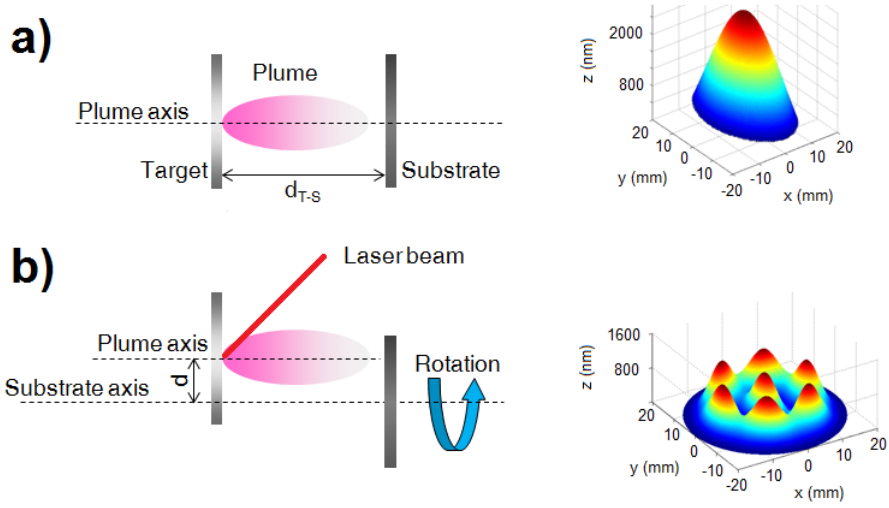

Figure 3.2: *PLD scheme (on the left) and shape of the deposited film (on the right) using the conventional setup (a) and by means of the "off-axis" technique (b).*

ablated particles arrives near the substrate edge. By suitably choosing d, it is possible to obtain homogeneous films with uniform thickness on a significant side area thanks to the proper overlapping of the deposited material.

As an example, the "off-axis" deposition technique was exploited in order to grow a highly-oriented polycrystalline Rh film, planar on an area on the order of 10 cm^2. As previously discussed, the deposition was performed in high-vacuum (3×10^{-3} Pa). The process parameters are: laser wavelength 1064 nm, fluence per pulse 19 J/cm^2, d_{T-S} 60 mm, deposition time 50 min. The evaporated species were collected on a 2.6×2.6 cm^2 (100) silicon model substrate, very suitable for characterizations. In particular, it allows to acquire the thickness of Rh films by cross-section SEM analysis, cutting the specimen along the middle plane. A series of depositions was performed changing the value of the parameter d, by step of one millimeter, both in positive (towards the laser beam) and negative (away from the laser) direction. For the selected process parameters, d = -5 mm resulted in the production of planar columnar Rh films. Figure 3.3 shows

a comparison between thickness profiles of two highly-oriented polycrystalline Rh films: the first (blue line) was deposited in a conventional way (coincident plume and substrate axes) and the second (red line) with the "off-axis" configuration (and d = -5 mm). Thickness data points were acquired by cross-section SEM analysis of the Rh films cut along the middle plane. The graph highlights the effectiveness of the "off-axis" deposition technique: film profile varies within 80 nm over an average thickness of ∼800 nm on a line of ∼26 mm length. Specifically, the requirements for FMs to be employed in the most of the ITER diagnostics are satisfied, that is thickness variation $< \lambda/2$, where $\lambda = 400$ nm is the lowest value of interest [67]. From the deposition time point of view, 50 min to grow

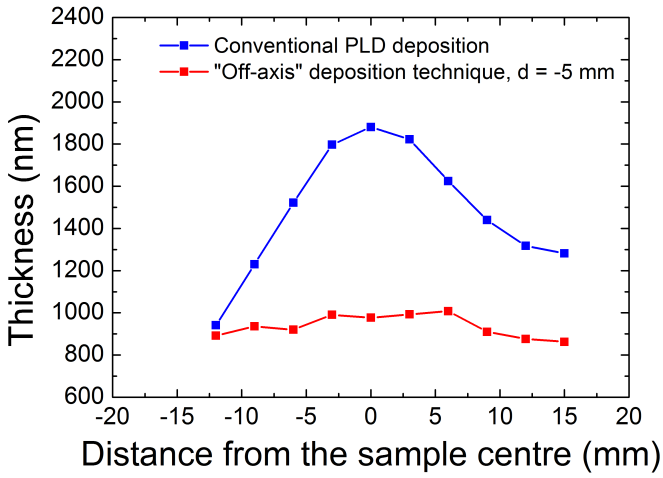

Figure 3.3: *Thickness profiles for a highly-oriented polycrystalline Rh film deposited with the conventional PLD configuration (blue line) and with the "off-axis" deposition technique (red line).*

planar Rh films 800 nm thick on a side area of 2.6×2.6 cm^2 is a very promising value. An estimate of the time required to produce Rh films on surfaces comparable to those of the main ITER FMs will be reported in section 3.3.

Another particularly important PLD shortcoming is the presence of particulate and droplets of various geometrical shapes and dimensions, typically with $\emptyset < 0.5$ μm and 1-3 μm [107], on the surface of the deposited films (figure 3.4). Micrometric droplets determine a critical increase of the diffuse reflectivity of the films. Consequently, proper handling of this possibly crucial drawback is mandatory as far as the production of mirrors

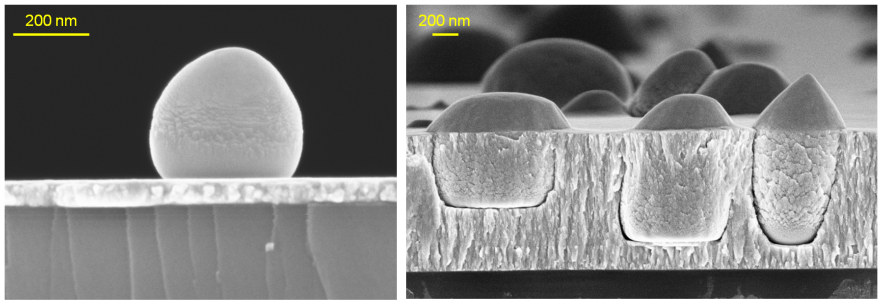

Figure 3.4: *SEM cross-section images of different Rh films. Droplets with various geometrical shapes and dimensions were deposited within them.*

is concerned. Droplets generation is mainly related to hydrodynamic instabilities at the target surface, to target superheating and liquid-phase expulsion under the action of vapour and plasma pressure [73, 110–112]. These phenomena strongly depend firstly on the material to be deposited and also on laser fluence per pulse, laser wavelength and target reflectivity. For rhodium, ablation with high fluence (10-19 J/cm^2), infrared laser pulses is a possible solution to achieve droplets suppression as well as a significant deposition rate. To investigate this option, two amorphous-like Rh films were produced using most of the same process parameters, like fluence per pulse ∼10 J/cm^2 and deposition time 40 min (which gave the same films thickness ∼800 nm), but different laser wavelengths: the first was deposited with the 2nd harmonic (green radiation, $\lambda = 532$ nm) and the second with the fundamental wavelength (infrared radiation, $\lambda = 1064$ nm). Figures 3.5a and b show the top-view by SEM (see appendix A.2 for an overview of the SEM technique and the SEM experimental setup used in the frame of this thesis) of the two amorphous-like Rh films. The surface of the Rh sample grown with green pulses (figure 3.5a) is uniformly covered by micrometric droplets. From the image relative to the Rh film deposited with infrared pulses (figure 3.5b), the effective reduction of droplets formation is evident. As an example of droplets influence on films optical properties, the diffuse reflectivity (R_{Diff}) of the two Rh coatings, measured by spectrophotometer (see appendix A.1.1), is reported in figure 3.5c. The mean diffuse reflectivity for the Rh sample deposited at $\lambda = 532$ nm is 15%. This value determines a dramatic decrease of the specular reflectivity (R_{Spec}) which becomes not acceptable in the frame of ITER FMs application. On the other hand, the diffuse reflectivity of the Rh film produced at $\lambda = 1064$ nm is very low (mean value 2%). As a re-

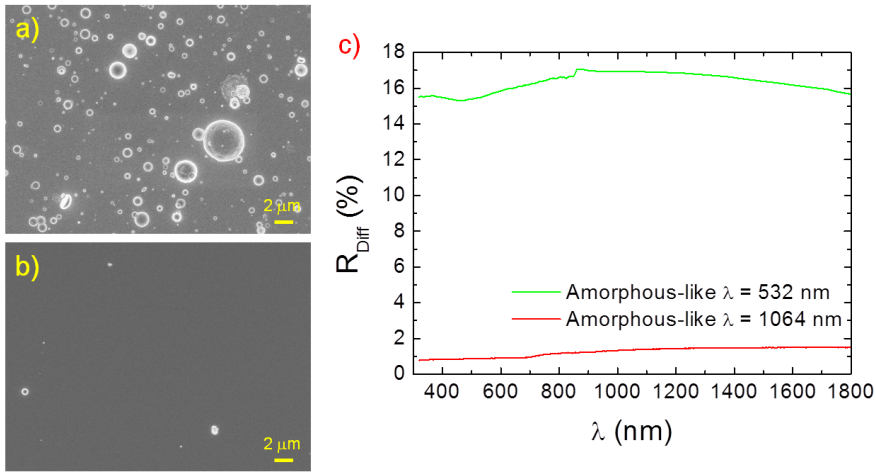

Figure 3.5: *SEM top-view images of amorphous-like Rh films deposited with the 2nd harmonic (a) and the fundamental wavelength (b), maintaining most of the other process parameters fixed. (c) Diffuse reflectivity (R_{Diff}), as measured by spectrophotometer on the 300-1800 nm wavelength range, for amorphous-like Rh films shown in SEM images (a) (green line) and (b) (red line).*

sult, total reflectivity (R_{Tot}) of the film almost coincides with the specular one.

To obtain satisfactory specular reflectivity, deposition of films with uniform properties over the area of interest and effective suppression of the droplets-induced diffuse scattering, together with a sufficiently low films roughness, are essential. In [72], Atomic Force Microscopy (AFM) measurements showed that generally speaking PLD Rh films could be produced with a roughness resembling the substrate one. Therefore, in the case of Rh films deposited onto suitably polished substrates, roughness would not influence their optical properties. Specular reflectivity is clearly crucial for mirrors performance and thus for the entire ITER diagnostics system. The developed optimized PLD process was thus exploited to produce both a highly-oriented polycrystalline and an amorphous-like Rh film with high-specular reflectivity on a significant side area. For the former, the process parameters were as follows: deposition in high-vacuum (3×10^{-3} Pa), laser wavelength 1064 nm, fluence per pulse 19 J/cm^2, d_{T-S} 60 mm, d -5 mm, deposition time 50 min. The production of the amorphous-like film was performed in helium atmosphere at 35 Pa, with fluence per pulse 10 J/cm^2, d_{T-S} 80 mm, d -4 mm, deposition time 60 min. Both samples were deposited onto 2.6×2.6 cm^2 (100) Si substrates. In fig-

ure 3.6 the specular reflectivity measured by spectrophotometer of these two samples, together with a reference calculated using optical constants of bulk Rh [6], is shown versus wavelength in the range 320-1700 nm. It can be seen that the two curves associated to the deposited films are

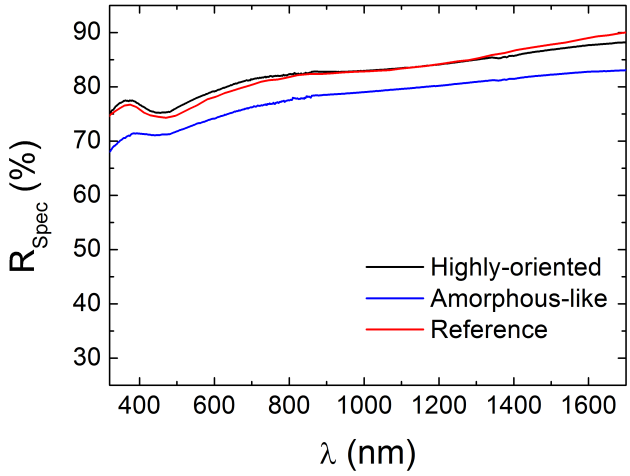

Figure 3.6: *Specular reflectivity (R_{Spec}) of the highly-oriented polycrystalline (black line) and the amorphous-like (blue line) Rh films deposited with high fluence, infrared laser pulses and the "off-axis" configuration, together with a reference calculated using optical constants of bulk Rh [6] (red line).*

very close to the reference. In these specific cases, since the surface root-mean-square Roughness (R_{rms}) of the Si substrates was about 0.1 nm, Rh films R_{rms} was maintained below 1 nm and therefore did not significantly contribute to the decrease of their specular reflectivity. The difference between the theoretical curve and that associated to the amorphous-like sample is lower than 5% in the whole spectral range. This slight discrepancy was probably related to an increase of amorphous-like Rh film light absorption coefficient due to surface contamination (by oxygen and hydrocarbons). This topic will be deeply discussed in chapter 4. We only anticipate here that the lower mean crystallite size of the amorphous-like sample, with respect to that of the highly-oriented film, determined a longer fraction of grain boundaries and hence a higher surface area to volume ratio which potentially brought to a relevant density of adsorption sites for the impurities.

3.2 Deposition of rhodium films with suitable mechanical properties

The production of sufficiently thick films is necessary to face the problem of FMs erosion during ITER operation. In this context, it is crucial to consider the fundamental aspect of film-substrate adhesion, to avoid buckling and delamination phenomena in the coating, caused by internal stresses. With the purpose of understanding the relation between film structure and adhesion properties, a scratch analysis was performed on a series of samples, ranging from highly-oriented to amorphous-like films. In particular, these samples were deposited on molybdenum (Mo), at $\lambda =$ 266 nm with fluence values per pulse in the range 1.25-1.6 J/cm^2, d_{T-S} 60 mm, respectively in high-vacuum and in He atmosphere at 5, 15 and 30 Pa. The mean thickness was about 1.2 μm. Morphologies and structures of Rh films deposited in these conditions are reported in [72]. Adhesion properties were investigated using a CSM instrument scratch tester. The indenter was a diamond stylus with a spherical tip ($\varnothing$ = 200 μm). The applied load was progressively increased from 0.03 N to 30 N at a rate of 10.79 N/min, on the 3 mm scratch length. The critical Load (Lc), i.e. the load at which the substrate becomes visible along the track, was determined by post-mortem observation of the scratch track by means of an Optical Microscope (OM). For a more detailed characterization, a second set of measurements was performed by applying a constant load close to Lc on the same scratch length.

Critical loads for the considered PLD Rh films as a function of the deposition pressure are reported in figure 3.7a. For the highly-oriented columnar film Lc weighs 12.9 N, which is comparable with that of Rh coatings produced by magnetron sputtering (dashed line) [113]. Lc decreases by raising the helium pressure. For the amorphous-like film obtained at 30 Pa, it is 2.48 N. This decreasing behaviour was probably due to the lower kinetic energy of the species impinging onto the substrate which finally led to worse adhesion. In figure 3.7b, OM images of the scratch tracks made at constant load, 10 N and 3 N for the highly-oriented and amorphous-like films (the latter deposited in He at 30 Pa), are displayed. The columnar film exhibits high adhesion to the Mo substrate: no deformation beyond the scratch track is present. The behaviour in the case of the amorphous-like sample is however opposite. It presents cohesion higher than adhesion to the substrate (ASTM ID: C1624-05). The scratch track shows the low adhesion and the brittle nature of this coating. According to the results achieved so far, it is possible to infer that, among the possible

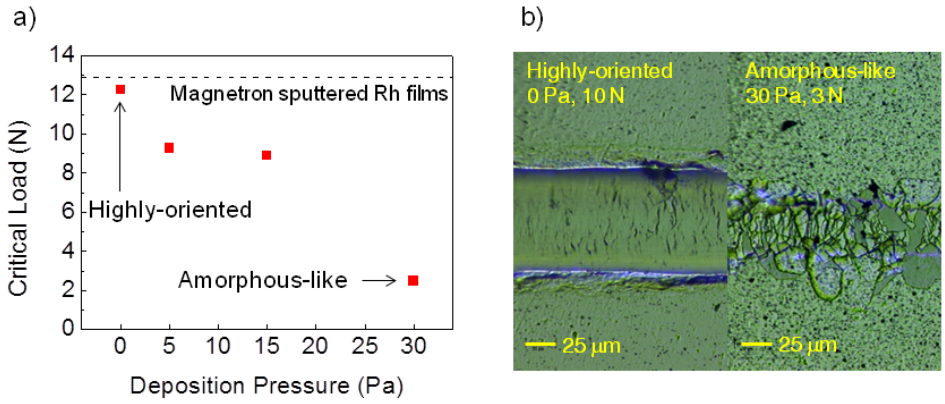

Figure 3.7: *(a) Critical load values versus deposition pressure for PLD Rh films (red squares). The dashed line represents the maximum Lc for magnetron sputtered Rh films [113]. (b) Optical images of the scratch track for: the columnar film and the amorphous-like sample grown in He atmosphere at 30 Pa.*

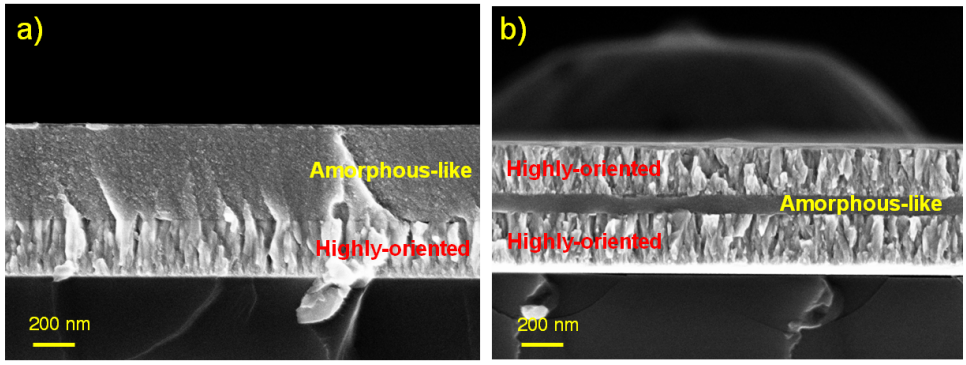

Figure 3.8: *(a) SEM cross-section image of an amorphous-like Rh film with a highly-oriented polycrystalline buffer layer deposited directly above the substrate. (b) SEM cross-section image of a Rh film with the following configuration: columnar Rh layer, amorphous-like Rh layer and columnar Rh layer.*

nanostructures achievable by PLD, the highly-oriented polycrystalline one guarantees the best adhesion to the substrate while the highest cohesion is obtained in the amorphous-like films. These behaviours open the possibility for the production of nanoengineered, properly optimized, multilayered configurations. For example, as far as the production of a thick amorphous-like Rh film is concerned, the associated low adhesion suggested the deposition of a columnar Rh buffer layer between the substrate

and the amorphous-like film. Figure 3.8a displays a SEM cross-section image of this film: a highly-oriented polycrystalline layer of ∼200 nm below an amorphous-like film nearly 600 nm thick. Unlike the amorphous-like nanostructure, the highly-oriented polycrystalline develops compressive strains in the deposited films which can compromise their mechanical stability for higher thicknesses. One possible approach to overcome this issue consists in the deposition of a series of thin amorphous-like Rh layers between thick columnar films, as shown in figure 3.8b.

3.3 Evaluation of the feasibility of producing rhodium films for ITER first mirrors by pulsed laser deposition

The time required to produce Rh films with the properties discussed in the previous sections is an important further aspect which has to be highlighted. The choice of the fundamental wavelength of the exploited laser source permits to employ high fluences per pulse (up to 20 J/cm^2) which minimize the deposition time. In particular, the deposition rates associated to a side area of 2.6×2.6 cm^2 for the highly-oriented polycrystalline and the amorphous-like films whereof the specular reflectivity was measured and shown in figure 3.6, were 3.3 nm min^{-1} cm^{-2} and 1.9 nm min^{-1} cm^{-2}, respectively, as evaluated by SEM cross-section analyses (see figure 3.3). Therefore, the deposition of 1 μm thick Rh coatings occurred approximately in about half an hour in the first case and in slightly more than a hour in the second case. It is interesting to quantitatively discuss the feasibility of the production of Rh films meeting the requirements for the development of FMs for ITER. In [3] a detailed list of the specifications for ITER FMs can be found. For example, as discussed in section 2.2, the foreseen Rh first mirror of the Thomson scattering core LIDAR diagnostic will have a diameter of 35 cm. On the other hand, the thickness of the film mirror critically depends on the location of the port of the corresponding diagnostic in the vacuum vessel of ITER. Referring to a Rh FM placed in an erosion-dominated zone, like the main chamber wall or the outer divertor, the estimated thickness required for several years of ITER operation is 5 μm [71]. With the aim of acquiring the information about the volume of the Rh layer produced by a single laser pulse from SEM cross-section analysis, a conventional PLD deposition (figure 3.2a) was performed for the identified experimental conditions and a relevant deposition time (e.g. 10 min). Starting from this information, a MatLab

programme was developed to estimate the deposition rate (in nm/min) inherent to the production of films on a given side area. The required PLD time was thus calculated dividing the films thickness by the obtained deposition rate. The estimated deposition rates can be largely increased by means of a laser source having the same parameters of the system employed and a repetition rate of 100 Hz (one order of magnitude higher). Four cases were considered: the production of highly-oriented polycrystalline (high-vacuum, fluence per pulse 19 J/cm^2, d_{T-S} 60 mm) and amorphous-like (He atmosphere at 35 Pa, fluence per pulse 10 J/cm^2, d_{T-S} 80 mm) Rh films with diameters of 10 cm, representative value for a typical Rh coated ITER FM mock-up [114, 115], and 35 cm. The deposition rates for the two laser systems, together with the time required to produce Rh FMs with a thickness of 5 μm, are given in table 3.1. It

Sample nanostructure	Ø (cm)	Dep. Rate (nm/min) @10Hz	Dep. Rate (nm/min) @100Hz	PLD time (hours) @100Hz
Highly-oriented	10	2.6	25.8	3
Highly-oriented	35	0.2	2.1	40
Amorphous-like	10	1.4	14.3	6
Amorphous-like	35	0.1	1.2	71

Table 3.1: *Estimated deposition rates (in nm/min) for the production of columnar and amorphous-like Rh films with diameters of 10 cm and 35 cm for the two laser systems, together with PLD process time (in hours) corresponding to a thickness of 5 μm by means of the laser source with the repetition rate of 100 Hz.*

is possible to conclude that PLD could be a promising deposition process for the production of ITER FMs. Moreover, to achieve specific mirror parameters, proper adaptation and optimization of the methods presented in this chapter can be required. For example, in order to produce planar Rh films with a profile excursion of some tens of nanometers on a side area of approximately 10 dm^2, the "off-axis" deposition technique could exhibit problems and difficulties in the assessment of the deposition parameters, especially in terms of the shifts of the substrate with respect to the target (quantity d). In this frame, a more sophisticated technique could be more suitable [109].

Once the deposition process was optimized, the natural continuation of this Ph.D thesis was to expose PLD Rh films to plasmas of proper dedicated machines or tokamaks to investigate their performance in environments with qualifying properties relative to ITER.

4

Rhodium films behaviour under deuterium plasma erosion

With the aim of addressing the potential of pulsed laser deposition towards the improvement of Rh films behaviour under ITER plasma erosion, this chapter presents an experimental investigation of the performance of Rh films exposed to a laboratory pure deuterium plasma, with some qualifying features relative to the ITER peripheral plasma facing first mirrors. The experimental campaign was developed in collaboration with the Nanolino group at the Physics Department of Basel University (November 2012). Since in the last decade Nanolino group has developed a research devoted to the deposition by magnetron sputtering of Rh coatings for FMs [70, 71], the investigation of PLD Rh films properties under pure deuterium plasma exposure also included the comparison with a magnetron sputtered sample. The main goal of this activity was to study the relation between Rh films performance (specular reflectivity) under erosion by deuterium plasma and their morphology and crystal structure. In section 4.1 the deuterium plasma exposure facility will be described. The characteristics of the samples being investigated will be discussed in section 4.2. Finally, in section 4.3 the results obtained and their interpretation in section 4.4 will be reported.

4.1 Experimental setup

The plasma exposure facility at the Physics Department of Basel University offers a complete toolkit for the manufacturing and investigation

of metallic mirrors, including experimental simulation of erosion and redeposition conditions that will likely occur in ITER [64, 116–118]. This is complemented by a wide set of equipments for chemical surface analyses and optical characterizations, including *in-situ* X-ray and UV Photo-Electron Spectroscopy (PES) and *in-situ* reflectometry, as well as plasma diagnostic tools. Figure 4.1 shows the experimental facility scheme (a) and photograph (b). It is constructed around a high-vacuum chamber equipped with a Radio-Frequency (RF) plasma source and magnetrons, permitting the injection of various types of gases and admixtures of impurities by means of magnetron sputtering. Conventional pumping systems are used to obtain a background pressure of 5×10^{-5} Pa. Plasma is created in a Pyrex tube of 12 cm diameter and 40 cm length through a matching network by a 13.56 MHz RF generator at a typical power of 90 W. This RF supply is coupled to the tube by an outer electrode acting as a surfatron. A mass spectrometer, a Langmuir probe and an optical spectrometer are used for plasma analysis. A samples carousel with heatable and biasable probe holders, which typically take specimens of 25 mm Ø, is located in the middle of the chamber. The small diameter of the samples compared to that of the plasma source guarantees homogeneity of the plasma across the specimens surface. An *in-situ* reflectometry system [117] (a detailed description of this apparatus is reported in appendix A.1.4) is used to monitor the evolution of $\tilde{R}(\lambda,t)$, the specular reflectivity relative to the initial reflectivity at an angle of incidence of 52° for wavelengths λ between 400-800 nm at a plasma exposure time t. A PES spectrometer is attached to the vacuum chamber, allowing samples to be directly transferred for chemical surface analysis after exposure.

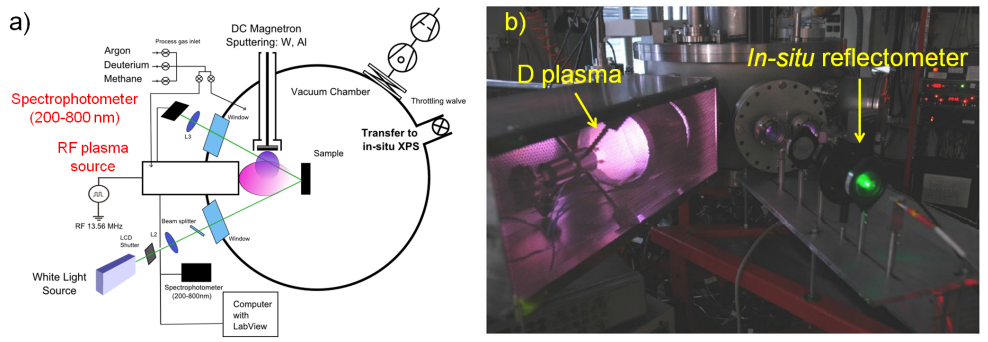

Figure 4.1: *Basel experimental facility scheme (a) and photograph (b).*

4.2 Rhodium films characteristics

In order to investigate the role of morphology and crystal structure of Rh films eroded by a pure deuterium plasma, one Rh film produced by the magnetron sputtering technique and three different PLD Rh films were considered. All the samples were grown on Stainless Steel-316L (SS) substrates (25 mm diameter, 2 mm thick), which were mechanically polished (first by abrasive silicon carbide paper, then by diamond paste, and finally by an alumina powder of 0.05 μm particles size).

Details about the complete deposition procedure and characterizations of the magnetron sputtered Rh film, henceforth referred to as "MS", are given in [70,71]. In summary, the Mean Crystallite Size (MCS) was around 10 nm, the crystallites did not present any specific texture or preferential orientation and SEM cross-section analysis showed dense columnar structure. The investigated sample was 300 nm thick.

The PLD films were produced with the optimized deposition process illustrated in chapter 3 ("off-axis" deposition technique, $\lambda = 1064$ nm, high fluence per pulse, in case multi-layered configuration) in different experimental conditions (in terms of pressure of the helium atmosphere, laser fluence per pulse, d_{T-S} and parameter d) in order to obtain various morphologies and crystallite sizes. The first sample was a highly-oriented polycrystalline columnar Rh coating grown as usual in high-vacuum 3×10^{-3} Pa, with fluence per pulse 19 J/cm^2, d_{T-S} 60 mm, d -4 mm. It is named as "columnar" in the rest of the chapter. The other two samples were amorphous-like films labeled as NC, from NanoCrystalline, indicating a mean crystallite size MCS below 10 nm (as detailed in the following). In particular, the deposition of the second and the third kind of PLD samples, NC1 and NC2, was performed in helium atmosphere at 40 Pa and 55 Pa, respectively. The values for laser fluence per pulse, d_{T-S} and d were fixed to 10 J/cm^2, 70 mm and -4 mm. To guarantee a high mechanical stability for NC1 and NC2 coatings, a Rh columnar adhesion layer was deposited directly above the SS substrate (section 3.2). The deposition time for each PLD sample was chosen in order to deposit films 700 nm thick. With the aim of investigating the crystallite size and orientation of the PLD Rh films, they were characterized by X-Ray Diffraction (XRD) both at a grazing incidence (with different angles of the X-ray source) and in $\theta/2\theta$ configuration (see appendix A.4). The mean crystallite size for each film was estimated starting from the spectra acquired by grazing XRD which, in the case of NC1 and NC2 samples, potentially minimized the contribution of the columnar adhesion layer to the XRD signal. For

the columnar film only the angle of incidence of 5° was considered. On the other hand, for NC1 and NC2, spectra were collected at: 5°, 4°, 3°, 2°, 1°, 0°, -0.5°, -1°. Figure 4.2 displays a comparison of the XRD signals acquired at 5° for the three PLD samples. For each spectrum, Rh peaks (111), (200), (220) and (113) were fitted with 1-3 Lorentz functions. The Scherrer's formula [108] was applied to each Lorentz function and the average of the values thus obtained was interpreted as an estimate for the mean crystallite size. The results are reported in table 4.1. The columnar

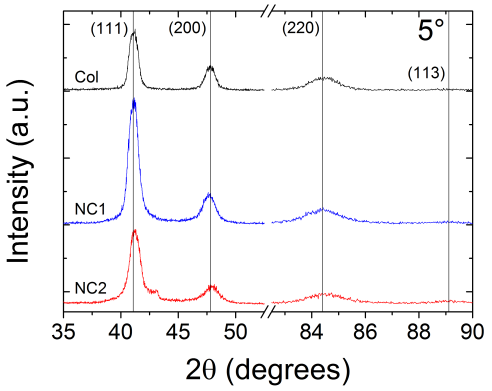

Figure 4.2: *Comparison of the XRD spectra acquired with an angle of incidence of 5° for: columnar (black line), NC1 (blue line) and NC2 (red line) Rh films.*

Sample name	MCS (nm)
Columnar 5°	12.28
NC1 5°	11.56
NC1 4°	7.88
NC1 3°	8.06
NC1 2°	8.32
NC1 1°	8.44
NC1 0°	8.20
NC2 5°	8.70
NC2 4°	6.56
NC2 3°	6.67
NC2 2°	5.85
NC2 1°	4.87

Table 4.1: *Mean Crystallite Size (MCS) from grazing XRD spectra.*

sample mean crystallite size is ∼12 nm. For NC1 and NC2 samples, the quantity MCS evaluated from the spectrum at 5° is greater than those estimated from the spectra collected at the other angles. Moreover, in the case of NC2 film, a decreasing trend of the mean crystallite size lowering the angle of the X-ray source is evident. These behaviours could be due to the influence of the columnar adhesion layer on the XRD data or to the conditioning of the same on the morphology of the film grown above it. Nevertheless the measurements performed at lower angles prove that the superficial layers (those actually exposed to the deuterium plasma) of NC1 and NC2 samples had MCS of ∼8 nm and ∼6 nm.

The orientation (111), perpendicular to the surface of the considered samples, was characterized using XRD $\theta/2\theta$ and the spectra thus acquired are displayed in figure 4.3. This kind of measurement setup allows the analysis of the crystalline structures in the direction perpendicular to the surface. It is thus possible to speak about film orientation because of

the absence or the different intensity of the collected reflections with respect to those measured for the bulk material. According to this, the $\theta/2\theta$ XRD spectrum of the columnar film confirms what just reported in literature [72], that is its high orientation along the (111) direction. This feature, although still present, becomes less evident for NC1 and NC2 specimens. The ratio between the areas of peaks (111) and (200) is 217.1, 31.4 and 2.9 for columnar, NC1 and NC2 Rh films, against 2.1 for the bulk.

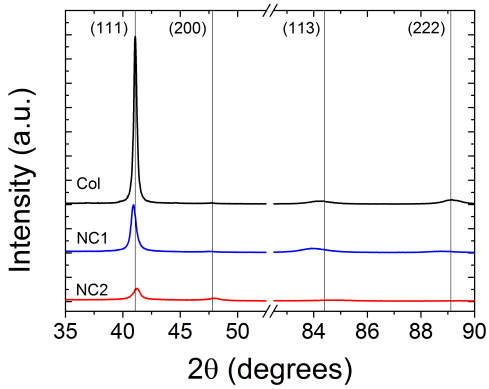

Figure 4.3: *Comparison of the XRD spectra acquired in $\theta/2\theta$ configuration for: columnar (black line), NC1 (blue line) and NC2 (red line) Rh films.*

To investigate Rh films morphology, the four samples were analyzed by SEM. Figure 4.4 shows the SEM top-view images for MS (a), columnar (b), NC1 (c) and NC2 (d) Rh films, where compact morphologies can be observed. For the NC2 film, it is also possible to notice the presence of a slight open structure or "granular-like" morphology. Moreover, a crack network around the scratches of the polished SS substrate is visible (figure 4.5a). This is the result of the combination between the tensile stress present in the film and its brittle nature (as shown in section 3.2). A typical crack width is of some tens of nanometers (figure 4.5b).

The details of the magnetron sputtered and the PLD samples are summarized in table 4.2.

Deuterium plasma exposures were performed in the experimental facility described in section 4.1. Before the exposure, Rh films were heated to a temperature of 150 °C and a bias of -200 V was applied to them, in order to mimic the expected edge conditions in ITER [119]. Deuterium was injected in the Pyrex tube with a flow of 70 sccm, in such a way that the incoming pressure was set to 3.05 Pa using conventional pumping systems.

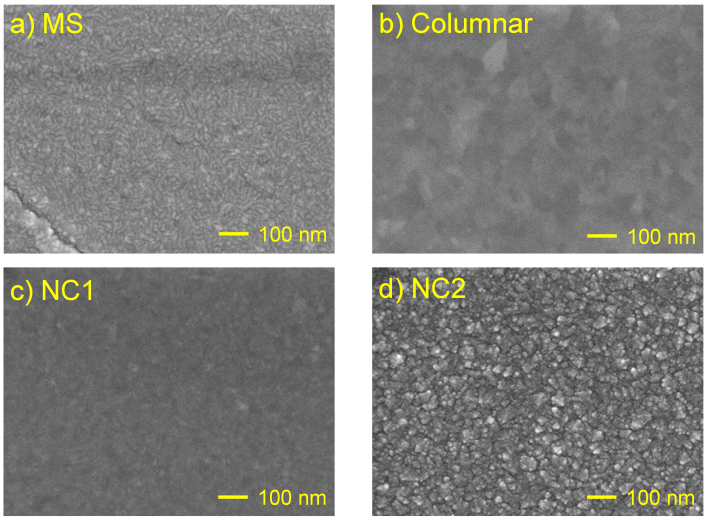

Figure 4.4: *SEM top-view images for: MS (a), columnar (b), NC1 (c) and NC2 (d) Rh films as deposited.*

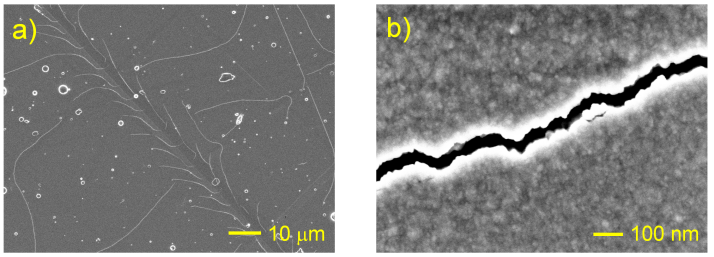

Figure 4.5: *SEM top-view images of the NC2 Rh film at two different magnifications. (a) Crack network close to a scratch of the polished SS substrate. (b) Magnified image around a crack.*

Sample name	Deposition technique	MCS (nm)	Morphology
Columnar	PLD	12	no features
MS [71]	magnetron sputtering	10	no features
NC1	PLD	8	no features
NC2	PLD	6	granular-like

Table 4.2: *Samples and their characteristics: deposition technique, mean crystallite size MCS (nm) and morphology.*

The total ion flux, including molecular ions, was estimated at 3.25×10^{19} m^{-2} s^{-1} with Langmuir probe measurements [116].

Ex-situ UV-vis-NIR total and diffuse reflectivities of the mirrors were

measured both before and after deuterium exposure by spectrophotometer (see appendix A.1.2) in the λ range 250-2500 nm. Specular reflectivity was calculated as usual by subtracting the diffuse reflectivity from the total reflectivity. Moreover, for each Rh film, the ellipsometric parameter angles (ψ,Δ) were measured *ex-situ* by ellipsometer (appendix A.1.3), both before and after plasma exposure, in the wavelength range 350-2100 nm for angles of incidence of 45°, 55° and 65°. Using a one layer fixed refractive index and absorption model, the fit of these six data sets was performed to obtain the optical constants of each Rh film as a function of λ. The specular reflectivity of the films at normal incidence was then recalculated using these optical constants.

The *in-situ* reflectometry equipment, described in section 4.1 and appendix A.1.4, was used to monitor the evolution of $\tilde{R}(\lambda,t)$, starting from the switch on of the heating system, till after the end of the deuterium plasma exposure, for wavelengths between 400 nm and 800 nm. For the NC1 specimen, $\tilde{R}(\lambda,t)$ is available only for λ = 450 nm, 550 nm and 650 nm.

The effects of deuterium plasma on Rh films morphology were investigated by SEM and by AFM topography (appendix A.3) with scan sizes for the latter of 1×1, 3×3 and 10×10 μm^2. The R_{rms} was then extracted from the AFM images as an average on five scan lines.

Before and after plasma exposure, the samples were transferred into the ultrahigh-vacuum chamber housing the XPS (appendix A.5), linked without breaking the vacuum to the high-vacuum exposure chamber (figure 4.1a). Large scale XPS spectra from 0 to 1000 eV did not show any other peak than those related to rhodium, oxygen and carbon. Fitting of the XPS spectra was performed using Doniach-Sunjic functions, after a Shirley background subtraction with the help of UNIFIT 2011 software. A convolution of Lorentz and Gauss line shapes was used to fit the individual peaks. Atomic concentrations were then estimated using Scofield sensitivity factors.

4.3 Results of the experiment

Figure 4.6 shows the specular reflectivity measured *ex-situ* before exposure by spectrophotometer (a) and ellipsometer (b) as a function of the wavelength for each Rh film, together with a reference calculated using optical constants of bulk Rh [6]. The specular reflectivity data measured with the two different instruments are rather comparable (although the

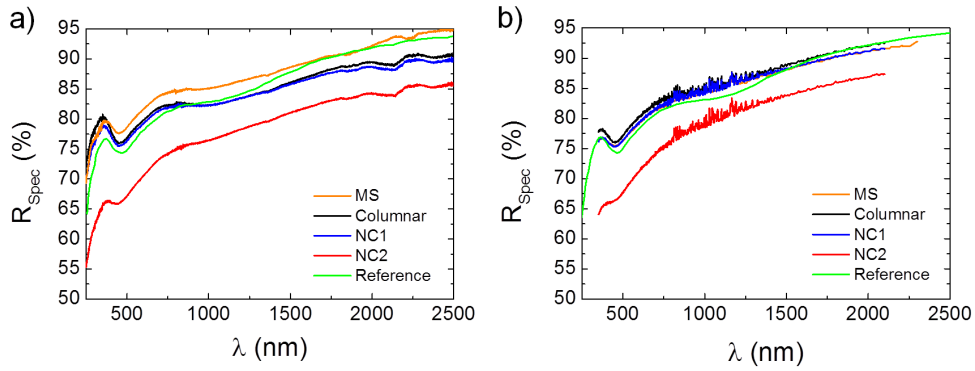

Figure 4.6: *Specular reflectivity measured ex-situ before the exposure by spectrophotometer (a) and ellipsometer (b) as a function of the wavelength for MS (orange line), columnar (black line), NC1 (blue line) and NC2 (red line) Rh films, together with a reference (green line) calculated using optical constants of bulk Rh [6].*

values acquired with the ellipsometer are lower than those measured with the spectrophotometer in the case of the MS sample). Except for the NC2 morphology, Rh films R_{Spec} tends to the reference. Lower values for the specular reflectivity of the NC2 sample are not unforeseen. In chapter 3, figure 3.6 showed that this behaviour is typical for PLD amorphous-like Rh films.

Figure 4.7 displays the trend of $\tilde{R}(\lambda,t)$ for λ = 450 nm, 550 nm and 650 nm in the case of: MS (a), columnar (b), NC1 (c) and NC2 (d) Rh films. For each of them, the exposure time to the deuterium plasma was: 838 min for MS, 753 min for columnar, 533 min for NC1 and 701 min for NC2. Considering the columnar sample, the maximum value of the t-axis in figure 4.7b is 646 min due to unexpected shut-down of the *in-situ* reflectometry system. The MS film exhibited a specular reflectivity approximately constant during the heating and began to decrease at the plasma switch on. Both for columnar and NC1 morphologies, the heating induced a decrease in the specular reflectivity. At the plasma switch on there was a sharp increase of $\tilde{R}$. Finally, during the exposure it decreased. For the NC1 film, at the plasma switch off the specular reflectivity slowly raised. The qualitative trend of $\tilde{R}$ is rather similar for these samples, while it is very different for the NC2 morphology. In this case, both heating and plasma switch on had a beneficial effect on the specular reflectivity of the coating. Furthermore, $\tilde{R}$ remained rather constant during the exposure.

Figure 4.8a shows the difference between the specular reflectivity measured *ex-situ* by spectrophotometer after and before deuterium plasma

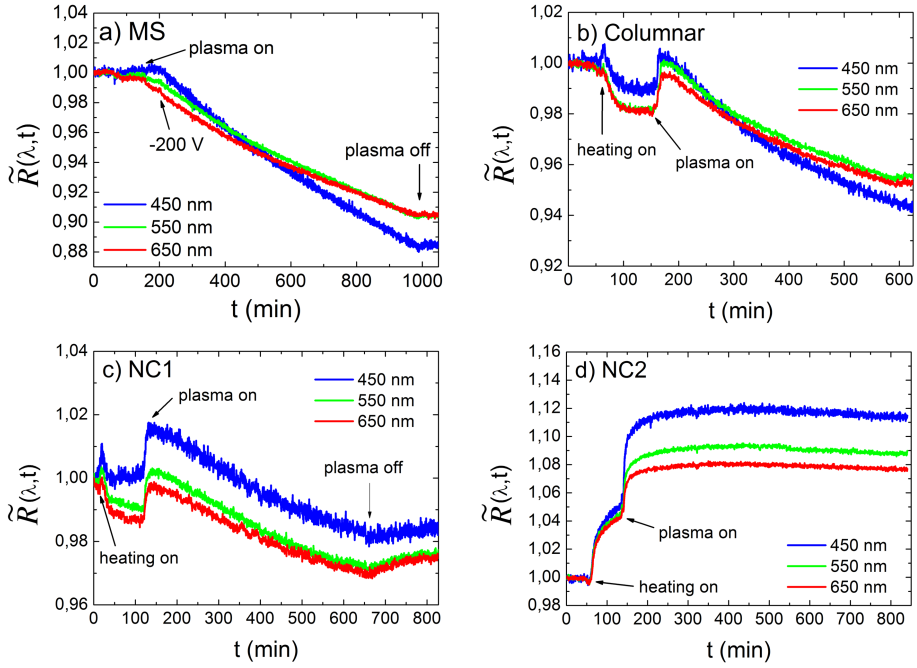

Figure 4.7: *$\tilde{R}(\lambda,t)$ for λ = 450 nm (blue line), 550 nm (green line), 650 nm (red line) in the case of: MS (a), columnar (b), NC1 (c) and NC2 (d) Rh films.*

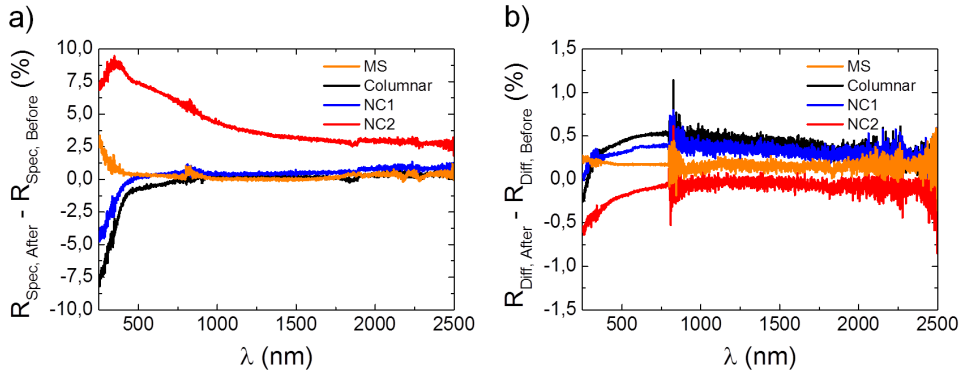

Figure 4.8: *(a) Difference between the specular reflectivity measured ex-situ by spectrophotometer after and before deuterium plasma exposure as a function of the wavelength for: MS (orange line), columnar (black line), NC1 (blue line) and NC2 (red line) Rh films. In (b) the same for the diffuse reflectivity.*

exposure as a function of the wavelength. In the case of MS, columnar and NC1 Rh films the specular reflectivity did not change significantly after the exposure. For $\lambda < 400$ nm the spectrophotometer displays an increase of the specular reflectivity for the MS sample (albeit Nanolino group demonstrated that this trend is not reproducible [120]) and a decrease for the columnar and NC1 Rh films, within few percents. The specular reflectivity for the NC2 specimen increased after the exposure approximately 5% on the entire wavelength range. Since the ellipsometer measurements (not shown here) do not add further information to that just pointed out by the spectrophotometer, in the following the quantity specular reflectivity acquired *ex-situ* means measured by spectrophotometer.

The difference between the diffuse reflectivity acquired *ex-situ* after and before plasma exposure as a function of the wavelength is reported in figure 4.8b. For each sample, it maintains within ∼1% on the entire wavelength range.

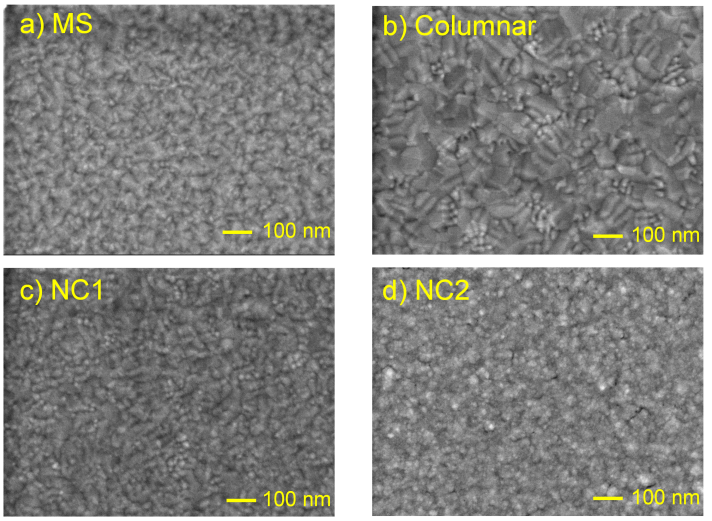

Figure 4.9: *SEM top-view images for: MS (a), columnar (b), NC1 (c) and NC2 (d) Rh films after the exposure to deuterium plasma. The MS SEM image refers to a sample which was subjected to many cycles of deuterium exposure and air storage.*

The effects of deuterium plasma on the Rh films morphology were investigated by SEM analysis. Figure 4.9 shows the SEM top-view images after the exposure for MS (a), columnar (b), NC1 (c) and NC2 (d) Rh films. The MS SEM image (a) refers to a sample which was subjected to many cycles of plasma exposure and air storage. Comparing figure 4.9

with figure 4.4, it is clear the change in morphology for MS, columnar and NC1 films induced by deuterium plasma. In the case of NC2 sample, the plasma exposure did not affect the morphology as well as the crack network.

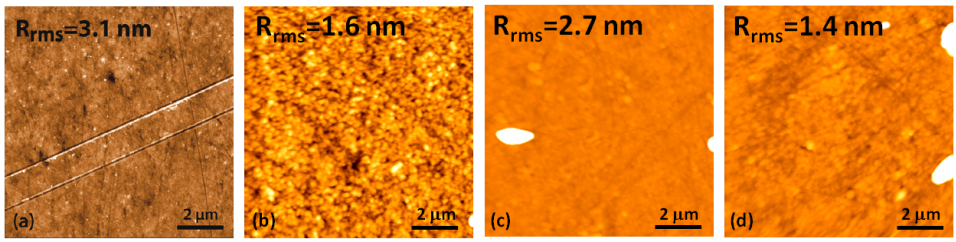

Figure 4.10: *10×10 μm^2 AFM topography images for: MS [64] (a), columnar (b), NC1 (c), NC2 (d) Rh films after the exposure to deuterium plasma.*

Besides SEM analysis, the deuterium plasma effects on the Rh specimens morphology were studied also by AFM. Figure 4.10 displays 10×10 μm^2 AFM topography images for MS [64] (a), columnar (b), NC1 (c) and NC2 (d) Rh films after the exposure to deuterium plasma. The straight lines in (a) are traces of the mechanical polishing of the SS substrate. The circular features in (c) and (d) are PLD droplets. The R_{rms} values for all the scanning areas (1×1, 3×3 and 10×10 μm^2) are summarized in table 4.3. The main result is that R_{rms} of all Rh films remains on the order of that of the SS substrate (few nanometers) even after the deuterium plasma exposure.

Sample name	R_{rms} (nm) 1×1 μm^2	R_{rms} (nm) 3×3 μm^2	R_{rms} (nm) 10×10 μm^2
Columnar	1.0	1.3	1.6
MS [64]	1.8	1.8	3.1
NC1	0.6	1.5	2.7
NC2	0.7	1.1	1.4

Table 4.3: *Surface root-mean-square Roughness (R_{rms}) of the different Rh films after deuterium plasma exposure extracted from AFM images acquired on scanning areas 1×1, 3×3 and 10×10 μm^2.*

The results obtained from the XPS analyses of Rh films before and after plasma exposure, in terms of peaks positions and atomic concentrations, are reported in table 4.4 (BE stands for Binding Energy and a-C:H for amorphous hydrocarbons). In the case of the MS sample, the outcomes refer to a film that was produced and measured by XPS without breaking the vacuum (section 4.1). It follows that no impurity peaks were observed

	MS	MS exposed	Columnar	Columnar exposed	NC1	NC1 exposed	NC2	NC2 exposed
$Rh3d_{5/2}$ metal BE (eV)	307	307	307.1	307.1	307.1	307.1	307.1	307.1
$Rh3d_{5/2}$ oxide BE (eV)			308.2		307.9		307.8	
O1s 1st peak BE (eV)			530.1		530.5		530.4	
O1s 2nd peak BE (eV)			531.4		531.7		531.6	531.6
C1s 1st peak BE (eV)			284.4		284.3	284.1	284.3	284
C1s 2nd peak BE (eV)			286.3		285.2		285.4	
% Rh metal	100	100	52	100	46	93	35	92
% Rh oxide			7		9		13	
% O oxide			8		11		9	
% O			10		2		3	3
% a-C:H			23		32	7	40	5

Table 4.4: *XPS analyses of the Rh films before and after deuterium plasma exposure: peaks positions and atomic concentrations. BE stands for the Binding Energy and a-C:H for amorphous hydrocarbons.*

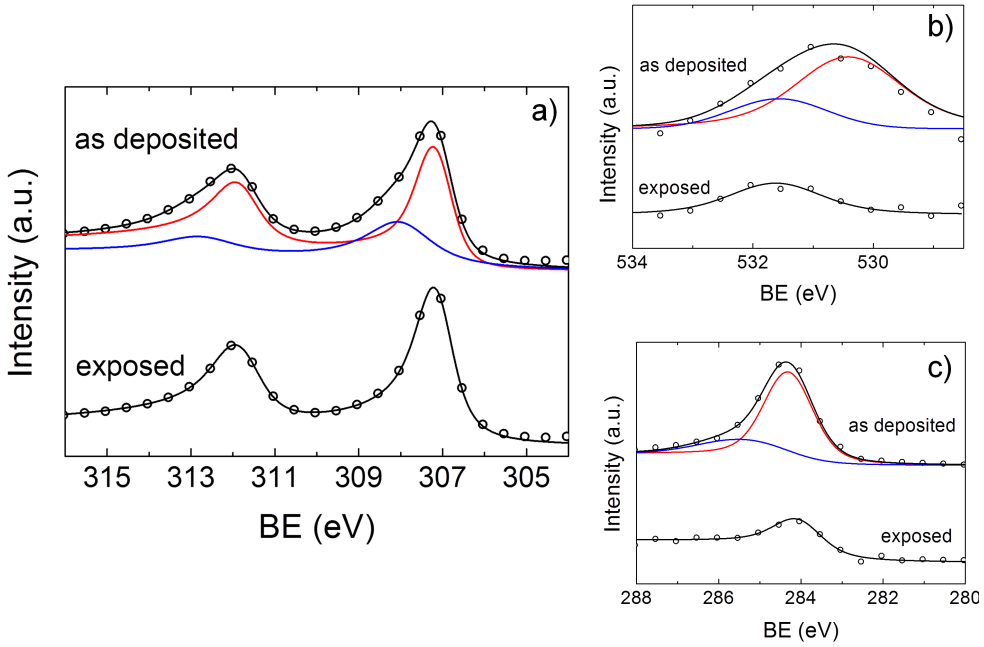

Figure 4.11: *(a) Rh3d core level XPS spectra of NC2 Rh film as deposited and after exposure. Open circles: measured data; full line: mathematical fit. Red and blue lines correspond to the metal and the oxide components, respectively, and the black one is associated to the fit sum. (b) O1s core level XPS spectra of NC2 Rh film as deposited and after exposure. Red and blue lines correspond to the peaks of Rh oxide and OH or H_2O molecules adsorbed on the surface, respectively. (c) C1s core level XPS spectra of NC2 Rh film as deposited and after exposure. Red and blue lines correspond both to the peaks of hydrocarbons.*

both before and after exposure. On the contrary, independently from the morphology, PLD Rh films (deposited *ex-situ*) were highly contaminated with oxygen and hydrocarbons before the exposure. Rh metal atomic

concentration was the lowest for the NC2 specimen, 35% (as an example, the XPS spectra of this sample are reported in figure 4.11). The exposure had a beneficial effect on the surface contamination as Rh metal atomic concentration after the process was above 90% for each PLD morphology. In particular, for the columnar film, only a metal component was present after the exposure.

4.4 Interpretation of the results

The results presented in section 4.3 show that the behaviour of Rh films under deuterium plasma exposure strongly depends on their crystal structure and morphology. Firstly, the lower specular reflectivity of NC2 sample before the exposure with respect to the reference, highlighted in figure 4.6, could be explained in terms of a high surface contamination, as shown by XPS data in table 4.4. They display a significant amount of oxygen and hydrocarbons contaminants onto its surface (Rh metal concentration is at least $\sim$10% lower than that of the other configurations) [121, 122]. This hypothesis is in agreement with the granular-like feature of the NC2 film (figure 4.4d); such a morphology, together with the crack network (figure 4.5), results in a higher surface area to volume ratio with respect to the other Rh samples which could favour the percolation of water, leading to a deeper oxidation, as well as a higher density of adsorption sites for hydrocarbons impurities.

The XPS data could also explain the sharp increase in specular reflectivity of all the PLD films at the plasma switch on, as shown by the *in-situ* reflectometry system (figures 4.7b-d). This phenomenon could actually be associated to the desorption of oxygen and hydrocarbons contaminants from the surface of the films as-deposited and also to the removal of the oxide structure for the NC2 sample.

In order to compare the effect of the deuterium plasma exposure on the *in-situ* specular reflectivity of the different morphologies, figure 4.12 shows $\tilde{R}$ at $\lambda = 450$ nm, as a function of the total deuterium ion fluence (estimated as the product between the exposure time and the deuterium ion flux) for the different Rh films. The limit of the fluence axis is around $9{\times}10^{23}$ ions m^{-2} which corresponds to about 55 ITER discharges for mirrors in equatorial ports [123]. The trend of $\tilde{R}$ for MS and columnar films is quite similar. The specular reflectivity decrease during deuterium plasma exposure is strongly reduced for the NC1 morphology and negligible for the NC2 sample. For the PLD Rh films, it is therefore clear that the

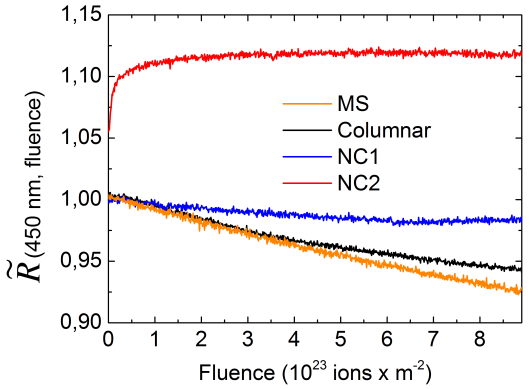

Figure 4.12: *$\tilde{R}$ at λ = 450 nm, versus the deuterium ion fluence in the case of: MS (orange line), columnar (black line), NC1 (blue line) and NC2 (red line) Rh films.*

$\tilde{R}$ decreasing rate reduces upon moving towards smaller mean crystallite sizes (see table 4.2).

The specular reflectivity decrease for MS, columnar and NC1 Rh films during deuterium plasma exposure is not due to the surface roughening by deuterium ions impact. As pointed out in section 4.3, the R_{rms} of all Rh films (table 4.3) remains on the order of that of the SS substrate (few nanometers) even after the deuterium plasma exposure. This is consistent with the difference between the diffuse reflectivity measured *ex-situ* after and before deuterium plasma exposure (figure 4.8b) which remains for every Rh films within ∼1% on the wavelength range 250-2500 nm.

The formation of a rhodium deuteride (RhD_x, $x \leq 2$) sub-superficial layer during deuterium plasma exposure was previously claimed to be the actual reason of the *in-situ* specular reflectivity drop of MS, columnar and NC1 Rh films. As explained in [64], after air storage their surface got depopulated of deuterium adsorbates due to a catalytic reaction between oxygen and deuterium, which resulted in a diffusion of the incorporated deuterium first to the surface and then into air. This agrees with the *ex-situ* spectrophotometer results of figure 4.8a which show how the original specular reflectivity of MS, columnar and NC1 Rh coatings is almost recovered for $\lambda \geq 400$ nm.

In order to stress the difference between the specular reflectivity measurements acquired *in-situ* during deuterium plasma exposure and *ex-situ* after air storage, the *absolute* specular reflectivity as a function of wavelength was calculated at the exposure time t = 430 min for each sample.

To evaluate this quantity, $\tilde{R}(\lambda,t = 430\ min)$ was multiplied by the specular reflectivity measured *ex-situ* with the spectrophotometer before the exposure. However, since $\tilde{R}$ was acquired at 52° while the spectrophotometer worked at a nearly normal incidence, $\tilde{R}(\lambda,t = 430\ min)$ at 0° was recalculated by means of the Fresnel's equations [124]. Figure 4.13 summarizes the results. The specular reflectivity recovery after air storage is clear for

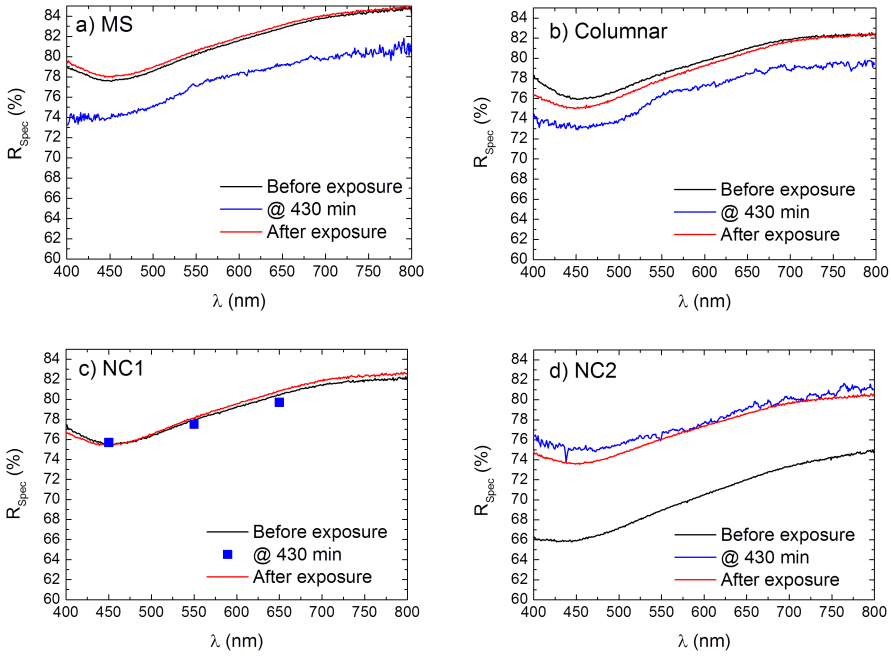

Figure 4.13: *Specular reflectivity as a function of the wavelength measured ex-situ before the exposure (black line), at 430 min (blue line/blue squares) and ex-situ after the exposure (red line) for: MS (a), columnar (b), NC1 (c) and NC2 (d) Rh films. Since for the NC1 specimen* $\tilde{R}(\lambda,t)$ *is available only for* λ *= 450 nm, 550 nm and 650 nm, in figure (c) the specular reflectivity at 430 min is represented by three squares.*

MS and columnar Rh films and is less significant for the NC1 specimen since its specular reflectivity at 430 min is still too close to that measured before the exposure. In the case of the NC2 sample, its *ex-situ* specular reflectivity after deuterium plasma exposure is only slightly lower than that measured *in-situ* at an exposure time of 430 min. The process of rhodium deuteride sub-superficial layer formation during exposure to the deuterium plasma potentially affected only MS, columnar and NC1 Rh films, although the specular reflectivity decrease during exposure for PLD

coatings reduces upon moving towards smaller mean crystallite sizes. The NC2 film could inhibit RhD_x sub-superficial layer formation thanks to its granular-like morphology which has a high surface area to volume ratio. The implanted deuterium diffused to the pores and either was stored there or diffused out to the vacuum. The crack network also acted as a further external surface for the outward diffusion. Assuming that the deuterium unloading rate of the lattice was higher than the loading one, no deuterium occupied the interstitial sites of the Rh lattice, hence the specular reflectivity of the NC2 sample maintained rather constant during plasma exposure. Unloading of the incorporated deuterium could also depend on the adsorption mechanism of deuterium on the Rh surface. Lower mean size of the ordered domains could influence the interaction between Rh surface and deuterium adsorbates [125, 126], favouring the outward diffusion. Hydrocarbons impurities could also play an additional role, since they could fill deuterium adsorption sites on the surface. In conclusion, the NC2 sample could get depopulated deuterium without requiring a reaction with oxygen. The significant tendency of the NC2 film to adsorb contaminants explains the slight decrease of the specular reflectivity after exposure and subsequent air storage.

To estimate Rh coatings performance under erosion in a tokamak environment (like that of ITER), figure 4.14 shows for each sample the specular reflectivity after 430 min of plasma exposure as measured by the *in-situ* reflectometry system. Albeit the specular reflectivity of the NC2

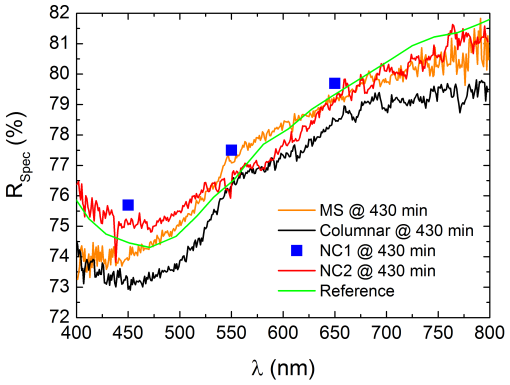

Figure 4.14: *Specular reflectivity at 430 min for: MS (orange line), columnar (black line), NC1 (blue squares) and NC2 (red line) Rh films, together with the reference (green line).*

film before the exposure was significantly lower than that of the other

samples, for an exposure time of 430 min it is still comparable with the reference. For longer exposures, the decreasing trend of $\tilde{R}$ reported in figures 4.7a-c for the MS, the columnar and the NC1 specimens, would result in a specular reflectivity well below to that of the NC2 film, which, on the contrary, would remain rather constant (figure 4.7d). Since the main requirement for ITER FMs is to maintain their specular reflectivity as high as possible and unchanged during operation (to make the diagnostic signals intense and reliable), the NC2 morphology shows promising properties, which could make it suitable for use in erosion-dominated zones. Exposure of the investigated Rh films in a tokamak is anyway necessary to study their performance in an environment closer to that of ITER and to obtain conclusive information towards the production of realistic mirror devices.

Part III

Laser cleaning from "tokamak-like" contaminants of rhodium films

5

Laser cleaning technique: methods development and first results

This chapter presents a preliminary study of the laser cleaning technique as a potential method to mitigate the re-deposition of ITER first-wall materials onto FMs. As discussed in subsection 2.3.3, re-deposition of eroded first-wall material transported in the plasma onto FMs surface will dramatically influence their performance during ITER plasma pulses. Therefore, a novel approach to the process of Rh films production-contamination-cleaning, in which the same laser system is exploited to experimentally investigate this topic with laboratory-scale facilities, was developed. In detail, this method consists of three steps: (i) production by PLD of Rh film mirrors, (ii) production by PLD of deposits with characteristics resembling those recovered from both operating tokamaks and ITER, and (iii) investigation of the laser cleaning technique onto PLD Rh film mirrors contaminated with PLD "tokamak-like" re-deposits. Point (i), the production by PLD of Rh coatings, was deeply discussed in chapter 3. A brief description of the Rh films, together with the other substrates, required for the study, will be reported in section 5.1. Point (ii), the deposition by PLD of tokamak-like contaminants, will be discussed in section 5.2. In section 5.3 the laser cleaning procedure, point (iii), will be described. The method to properly determine the required process parameters, with particular reference to the evaluation of Rh films laser damage threshold, i.e. the laser fluence per pulse at which damage occurs on Rh films surface, as a function of number of pulses, will be discussed. Finally, the results of the laser cleaning of Rh coatings contaminated with

C films, having different morphologies, will be shown.

5.1 Mirrors used in the investigation

Since the outcomes of the laser cleaning trials strictly depend on the nature of the materials involved, the choice of the substrates and the contaminants to be deposited above them, is particularly relevant.

As a first preliminary step, a model substrate to quickly perform the general procedure of tokamak-like re-deposits production and laser cleaning, saving the time for Rh coatings deposition, was selected. (100) silicon wafer 0.7 mm thick was chosen for the following reasons. This substrate is widely used in the frame of PLD thanks to its availability and low cost. Furthermore, its peculiar properties allow a deep characterization of the film grown above it (e.g. SEM cross-section analysis).

Once the procedure was tested onto the model substrate, the next step consisted in investigating the laser cleaning of tokamak-like contaminants deposited onto realistic mirror substrates, that are Rh films deposited onto (100) Si wafers. Both the peculiar Rh nanostructures achievable by PLD, i.e. the highly-oriented polycrystalline and the amorphous-like (see chapter 3), were studied. The deposition of the former was performed in high-vacuum as usual. Laser fluence per pulse, d_{T-S} and the parameter d, were chosen at 19 J/cm^2, 60 mm and -4 mm, respectively. The deposition time of 50 min permitted the growth of a 1 μm thick columnar film. Two amorphous-like Rh films were analyzed. Both were produced in helium atmosphere at 40 Pa with fluence per pulse 10 J/cm^2, d_{T-S} 70 mm and d -6 mm, for 40 min (films thickness of $\sim$700 nm). With the aim of studying the influence of the adhesion layer onto the amorphous-like Rh films laser damage threshold, only one of the amorphous-like samples presented a highly-oriented polycrystalline buffer layer, $\sim$200 nm thick.

The standard dimensions of these substrates were 2.6$\times$2.6 cm^2 which, as it will be clear later, permitted to perform up to four attempts of the elaborated laser cleaning procedure on a single sample (static approach). Moreover, 2.6$\times$2.6 cm^2 represents an interesting dimension as an example of "realistic" area for ITER FMs to be cleaned.

5.2 Deposition of tokamak-like contaminants

In subsection 2.3.5 it was highlighted that the main features of the re-deposited materials are related to those of the eroded PFCs of the con-

sidered tokamak. In reference to the available literature and to the ITER design, it is possible to identify some recurring chemical elements in tokamaks re-deposits: carbon, tungsten, beryllium and hydrogen isotopes, separately or combined. The technological constraints of the PLD system employed in the frame of this thesis, together with the safety issues, limited the choice of the materials that could be deposited by PLD to carbon and tungsten. The operation with hydrogen atmosphere is really complex due to its explosion characteristics. The high toxicity of beryllium imposes its handling in suitable laboratory facilities which, considering the nuclear fusion research field, are really few.

As discussed in subsection 2.3.5, two of the most recurring re-deposits morphologies are: low adhered compact films and contaminants with a very open morphology or "quasi-films". In particular, the latter are typically found in regions not in direct contact with the plasma, as the ducts where some of the FMs in ITER will be allocated.

The deposition of carbon and tungsten carbide (WC) films with compact and very open morphologies, using a 2 in. graphite target (purity 99.9%) without and with W wires, respectively, was thus considered as the starting point to simulate tokamak-like contaminants by PLD.

Since NanoLab in 2011 launched a research devoted to the production of C films by PLD for application in the frame of target normal sheath acceleration [127], the choice of the main process parameters for depositing carbon films with tokamak-like morphologies was aided by the progress in this activity. C depositions were therefore performed in helium atmosphere, with laser wavelength $\lambda = 532$ nm and fluence per pulse 1.6 J/cm^2, for a deposition time of 5 min which should have guaranteed films thickness of at least some hundreds of nanometers. The experimental parameters varied to faithfully resemble the features of the re-deposits retrieved from full-C tokamaks were the He pressure and d_{T-S}. Both these quantities influence the energy of the ablated species impinging on the substrate. Using low gas pressures and d_{T-S} values, the preferential growth mechanism is atom by atom and the resultant film has a compact morphology. On the other hand, with relevant background pressures and high d_{T-S}, the scattering between the ablated species and the molecules of the buffer gas favours the cluster assembling growth. In these conditions, the morphology of the film is highly open and porous.

The deposition of C compact films was performed in high-vacuum (3×10^{-3} Pa) and in He atmosphere at 5 Pa. The parameter d_{T-S} was chosen at 70 mm. Figure 5.1a displays a typical SEM cross-section image of C compact films deposited by PLD. It is easy to notice that with a depo-

sition time of 5 min, the growth of a ∼200 nm thick C compact re-deposit was achieved. Besides the typical tokamak-like morphology, the selected process parameters also permitted to produce films with bad mechanical properties. As shown in figure 5.1b, buckling and delamination phenomena, fingerprints of the scarce adhesion of the film to the substrate, were very common in PLD C compact contaminants. By means of the PLD technique, it was thus possible to faithfully reproduce the compact and flaking re-deposits retrieved from mirrors placed in all-C JET divertor in the frame of the first mirror test [59–61] (figure 2.13).

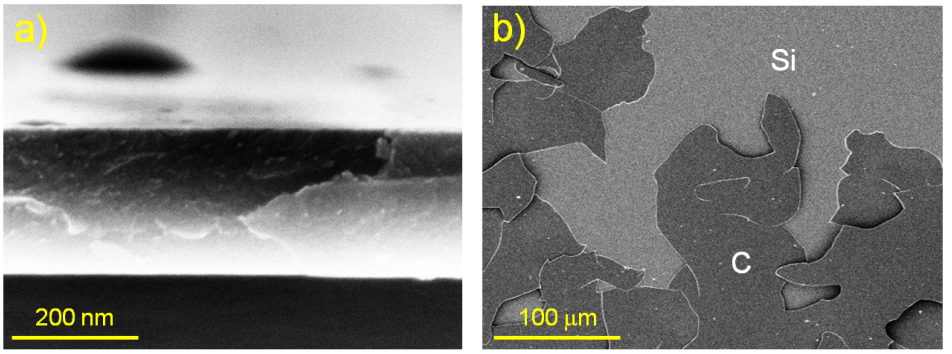

Figure 5.1: *SEM cross-section (a) and top-view (b) images of a compact C film deposited in high-vacuum (3×10^{-3} Pa) on a Si substrate. From figure (b) the flaking nature of the simulated re-deposit is evident.*

Contaminants with a very open morphology or "quasi-films" were obtained raising the He pressure to 60 Pa and d_{T-S} to 90 mm. As a consequence of the lower density with respect to the compact morphology, a deposition time of 5 min allowed the production of ∼2 μm thick C quasi-films. Figure 5.2a shows the SEM cross-section image of a C quasi-film deposited on a highly-oriented polycrystalline Rh film. From the associated SEM top-view image of figure 5.2b, a very open morphology, which closely resembles that of contaminants found in carbon-based tokamaks (figure 2.14), can be appreciated.

Relative to the tungsten carbide films, the depositions were performed in He atmosphere, with laser wavelength 532 nm and fluence per pulse 1.6 J/cm^2, as in the case of C contaminants production. The deposition time was instead chosen at 20 min. It was chosen a deposition time four times bigger than that for the C re-deposits because the presence of tungsten wires onto the graphite target probably should have reduced the deposition rate of the WC films.

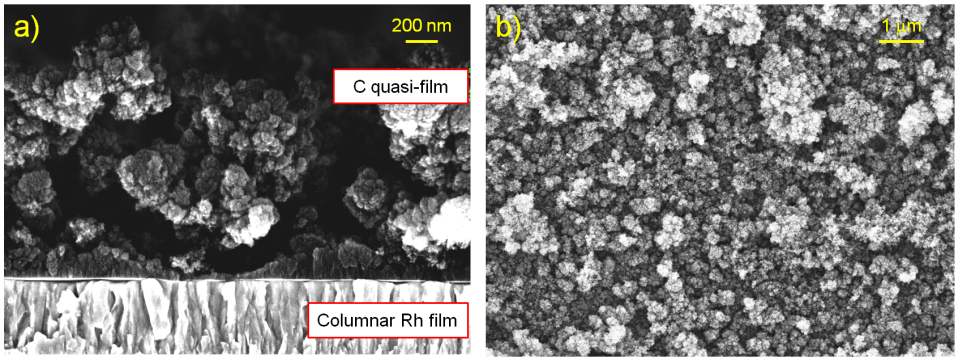

Figure 5.2: *SEM cross-section (a) and top-view (b) images of a C quasi-film grown on a highly-oriented polycrystalline Rh film.*

The deposition of compact WC films was done in high-vacuum and the parameter d_{T-S} was set to 60 mm. With respect to the compact C films, the addition of tungsten determined an increase of the mechanical properties of the WC coatings thus produced. Visual inspection and SEM analysis showed indeed that no buckling and delamination phenomena occurred. Since the SEM images of the compact WC films are qualitatively similar to those shown in figure 5.1 for a compact C re-deposit, they are not reported here.

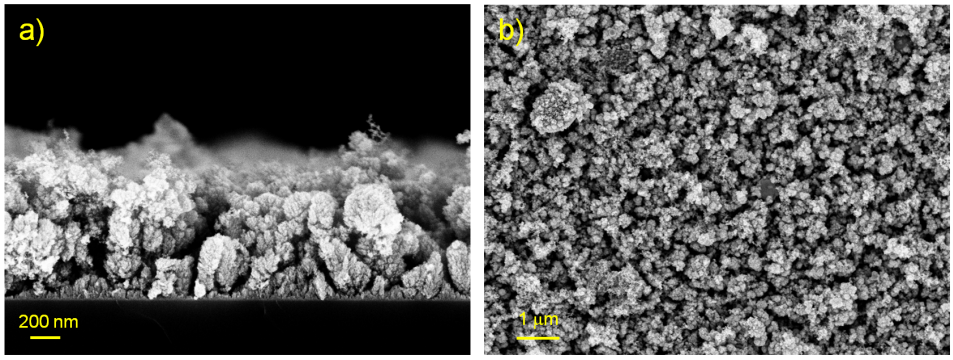

Figure 5.3: *SEM cross-section (a) and top-view (b) images of a WC quasi-film deposited on a Si substrate.*

Tungsten carbide quasi-films were produced increasing the helium pressure to 100 Pa. Due to the higher kinetic energy of the ablated species from the WC target, the value of 60 Pa chosen in the case of the deposition of C contaminants with an open morphology was too low and did not

permit to obtain the same morphology reported in figure 5.2. Figure 5.3 shows the SEM cross-section (a) and top-view (b) images of a tungsten carbide quasi-film. Albeit the high deposition time, the thickness of the WC coating barely reaches $\sim$1 μm.

The discussion developed in this section highlights that a suitable procedure was elaborated in order to faithfully reproduce, by PLD, tokamak-like C re-deposits. In the case of WC films, the PLD process parameters need to be properly optimized in order to deposit flaking contaminants as those in figure 2.13 and WC films with an open morphology closer to that obtained for PLD C re-deposits (figure 5.2). For these reasons, the laser cleaning technique was firstly tested on C low adhered compact and quasi-films (subsection 5.3.3). The extension to PLD tungsten carbide contaminants constitutes one of the first possible perspectives of this Ph.D thesis.

5.3 Laser cleaning of rhodium films

From literature [91], it is clear that the most important parameters which rule the laser cleaning process are: the laser wavelength, the laser fluence per pulse, the number of pulses considered and the atmosphere in which the procedure is done. In order to perform a preliminary methodological analysis, a first set of parameters was chosen.

5.3.1 Laser cleaning process parameters

One of the main conditions that a suitable laser cleaning procedure has to guarantee is the integrity of the substrate that has to be treated. Therefore, it was necessary to properly choose the correct process parameters to satisfy this condition. In the frame of this Ph.D thesis, Rh films laser damage threshold assessment and laser cleaning of C contaminated Rh films (system C/Rh) were mainly conducted with infrared (IR) laser pulses at $\lambda = 1064$ nm (the fundamental wavelength of the exploited laser source). This choice was justified by two principal reasons. First, high values for Rh reflectivity and absorption length in the infrared region of the electromagnetic spectrum [6] potentially ensured a high laser damage threshold of the Rh substrate. Second, it was demonstrated a satisfactory laser cleaning efficiency with infrared laser pulses of tokamaks C re-deposits on PFCs [95–98]. Moreover, infrared wavelengths are well suitable for optical fiber applications, permitting remote handling [106]. This is one of the

technological constraints that a laser cleaning procedure has to respect in order to be employed in the frame of ITER.

To study the role of laser fluence per pulse in the cleaning process, pulse energy was changed with fixed laser spot dimensions ($\sim$90 mm^2, unless different specification). The investigated fluence range was 350-1200 mJ/cm^2. The lower limit of 350 mJ/cm^2 was dictated by the particular laser source and optical system employed. The other main parameter considered was the number of laser pulses hitting Rh substrates and C/Rh films. The maximum number of laser pulses was 3000. The combined effect of these two parameters on Rh coatings laser damage threshold and on C laser cleaning efficiency was investigated. The fluence per pulse multiplied by the total number of laser pulses will be indicated as "total laser fluence" in the following.

In order to maximize the number of laser exposure sites per sample, a suitable movement procedure was elaborated. According to the laser spot area and the substrate dimensions, 4-6 spots per sample were identified.

Since laser cleaning for ITER application will be probably done between plasma discharges, laser damage threshold and cleaning experiments were performed in high-vacuum (3×10^{-3} Pa).

5.3.2 Rhodium films laser damage threshold

A different laser fluence per pulse was associated to each of the 4 exposure spots identified onto the highly-oriented columnar Rh film. The maximum number of laser pulses considered to determine its laser damage threshold ($\Phi_{\mathrm{Rh,c}}$) was 3000. However, the irradiation was promptly interrupted if a luminous signal coming from the sample, indicating the onset of a damage of the Rh film, was detected. It could be due, for example, to film ablation or to the removal of macroscopic fragments from its surface. The fluence range of 350-900 mJ/cm^2 is investigated in detail. For 900 and 750 mJ/cm^2, laser exposure was interrupted after $\sim$10 s since visible sparks were detected. As the laser repetition rate was 10 Hz, the corresponding number of pulses for 10 s was 100. Visual inspection and SEM analysis (figure 5.4a) showed the presence of sub-millimetric damages. From the magnified SEM top-view image of the spot irradiated at 900 mJ/cm^2, reported in figure 5.4b, the onset of severe damages in the form of ripples was evident. $\Phi_{\mathrm{Rh,c}}$ for 100 laser pulses was lower than 750 mJ/cm^2. In the case of 650, 550, 400 and 350 mJ/cm^2, no luminous signal was detected during the exposure to 3000 pulses. However, for 650 and 550 mJ/cm^2, visual inspection and SEM investigation displayed again the

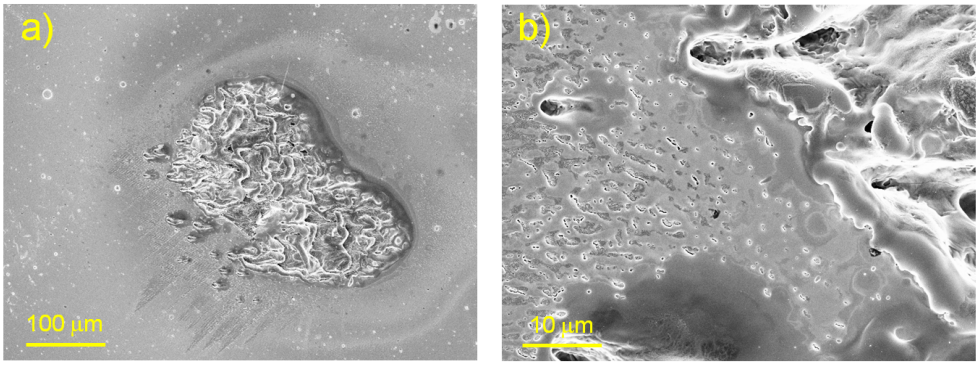

Figure 5.4: *SEM top-view images at two different magnifications of the irradiated spot at 900 mJ/cm^2 for 100 laser pulses of the highly-oriented polycrystalline Rh film. (a) Sub-millimetric damage. (b) Magnified image around it.*

onset of damage onto the Rh coating, albeit its extent was clearly lower than that shown in figure 5.4. For 400 and 350 mJ/cm^2, visual inspection revealed no damage at all. Figure 5.5 displays SEM top-view images of the highly-oriented polycrystalline Rh film as deposited (a) and after 3000 pulses at 350 mJ/cm^2 (b). No main effects as a consequence of the laser

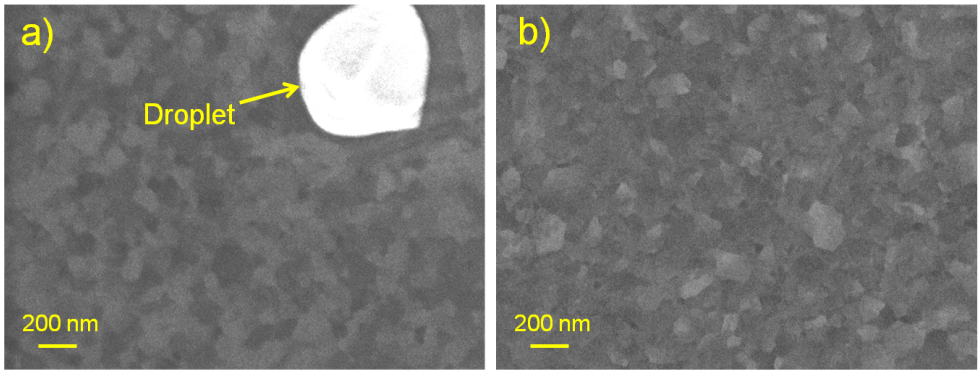

Figure 5.5: *SEM top-view images of the columnar Rh film as deposited (a) and after 3000 pulses at 350 mJ/cm^2 (b).*

heat load are noticeable at the sub-micrometric scale. Even in this case, visual inspection and SEM analysis gave the same result. It was possible to conclude that $\Phi_{\mathrm{Rh,c}}$ for 3000 laser pulses felt in the range 400-550 mJ/cm^2.

Unlike the highly-oriented polycrystalline film, the fluence per pulse impinging on a single exposure site identified onto the amorphous-like

films was fixed. The investigated parameter was the total laser fluence, i.e. a different number of identical pulses was associated to each of the 4-6 exposure spots.

The amorphous-like Rh film with the columnar buffer layer was irradiated with a fluence per pulse of 350 mJ/cm^2, for 1, 2, 5, 50 laser pulses. A photograph of the treated sample is reported in figure 5.6a. Even at one pulse, the film appears damaged. Figures 5.6b and c show the SEM analysis of the site exposed to 5 laser pulses. A severe damage in the form of melted and successively re-solidified Rh film is evident. The laser damage threshold ($\Phi_{Rh,a}$) associated to this sample was therefore below 350 mJ/cm^2 just for one laser pulse.

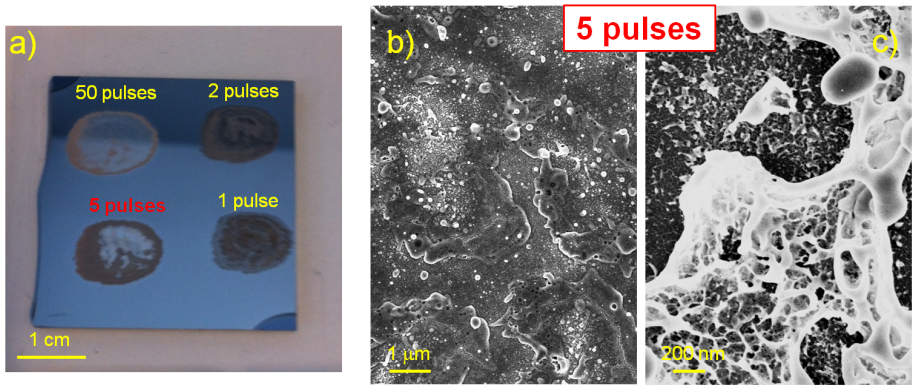

Figure 5.6: *Photograph of the amorphous-like film with the columnar buffer layer exposed to a fluence per pulse of 350 mJ/cm^2, for 1, 2, 5, 50 laser pulses (a). SEM top-view images of the spot irradiated with 5 laser pulses: low (b) and high (c) magnification.*

As discussed before, with the aim of studying the influence of the adhesion layer on the interaction between laser pulses and amorphous-like Rh morphology, an amorphous-like Rh film lacking in the columnar buffer layer was exposed to infrared laser pulses. The available results refer to trials with fluence per pulse 1200 mJ/cm^2 in face of 40 mm^2 laser spot area. The lower dimension of the laser spot permitted to identify 6 sites to be exposed on a unique sample. The different sites were irradiated with 1, 2, 3, 4, 5, 50 laser pulses, respectively. Figure 5.7a shows the appearance of the amorphous-like Rh film after the exposures. Since the fluence per pulse considered was significantly higher than 350 mJ/cm^2, the onset of damage was foreseeable even for one laser pulse. It is however interesting to compare the SEM analysis performed on the site of the amorphous-like Rh film with the adhesion layer exposed to 5 laser pulses (figures 5.6b

and c), with that on the site of the amorphous-like Rh film lacking in the columnar layer irradiated with a single pulse (figure 5.7b). Albeit these sites were exposed to approximately the same total laser fluence, the interaction processes between laser pulses and the two films were rather different. In particular, due to the absence of the columnar layer, the main mechanism of damage visible from figure 5.7b was the exfoliation, which is clearly a symptom of the scarce adhesion of the amorphous-like Rh film to the silicon substrate.

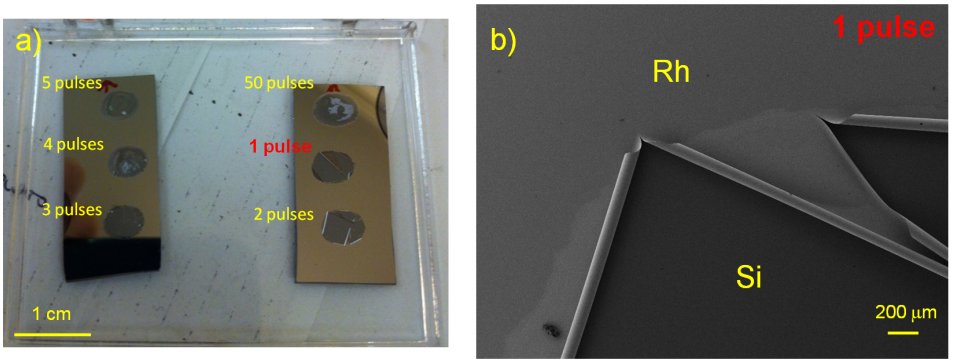

Figure 5.7: *Photograph of the amorphous-like Rh film lacking in the columnar buffer layer exposed to a fluence per pulse of 1200 mJ/cm^2, for 1, 2, 3, 4, 5, 50 laser pulses (a). SEM top-view image of the spot irradiated with 1 laser pulse (b).*

5.3.3 Laser cleaning of carbon contaminated rhodium films

In order to elaborate a suitable laser cleaning procedure to face ITER FMs re-deposition concern with laboratory-scale facilities, subsection 5.3.2 highlighted the better predisposition, in terms of a higher value of the laser damage threshold, of the highly-oriented polycrystalline Rh film with respect to that of the amorphous-like Rh coating, to be employed as the substrate for the preliminary laser cleaning tests. Moreover, it was natural to start the activity trying to remove by laser pulses a mono-elemental redeposit. For these reasons, the laser cleaning of C low adhered compact and quasi-films from columnar Rh coatings was performed and the main related results will be discussed in this subsection.

Considering the chronological order, a first explorative test was conducted onto a C quasi-film contaminated columnar Rh coating exposed to a fluence per pulse of 350 mJ/cm^2, for 1, 50, 600 and 3000 pulses. As described in subsection 5.3.2, $\Phi_{Rh,c}$ for 3000 pulses was between 400

and 550 mJ/cm^2, therefore 350 mJ/cm^2 should have guaranteed the integrity of the Rh substrate, even for the maximum number of laser pulses considered. At this first stage, the irradiated sites were characterized by visual inspection and SEM. Figure 5.8a shows a photograph of C contaminated Rh film after the irradiation. It is evident that the cleaning efficiency increases with the number of pulses. At visual inspection, the spot exposed to 3000 pulses seems to be almost clean from C contamination. Two SEM top-view images relative to this spot are reported in figures 5.8b and c. Both with low (b) and high (c) magnification, it can be seen that the Rh substrate is actually completely covered by C particles and aggregates, with dimensions that go from some nanometers to some hundreds of nanometers. This example demonstrates that visual inspection alone could not be enough to properly evaluate the effectiveness of the laser cleaning procedure.

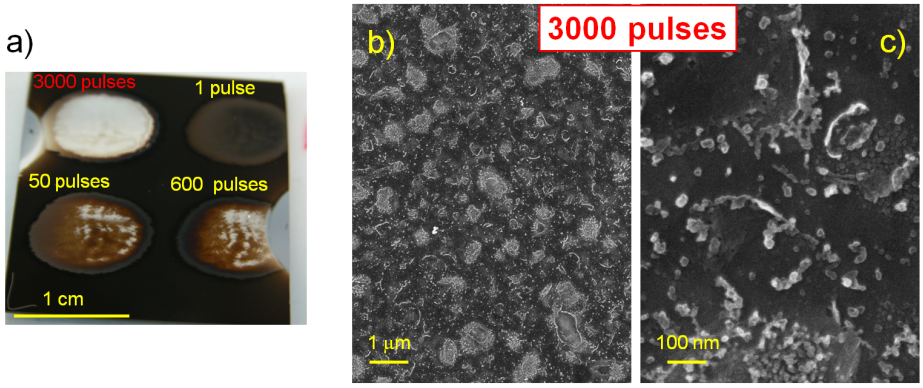

Figure 5.8: *Photograph of the laser cleaned C quasi-film contaminated columnar Rh coating at 350 mJ/cm^2, for 1, 50, 600 and 3000 pulses (a). SEM top-view images of the C/Rh film exposed at 350 mJ/cm^2 for 3000 pulses: low (b) and high (c) magnification.*

One potential way to increase the efficiency of the process was the exposure of samples to laser pulses having higher energy. Two approaches were investigated: exposure at a "moderate" fluence, 400 mJ/cm^2, closer to $\Phi_{Rh,c}$ for 3000 pulses and irradiation at "high" fluence, 900 mJ/cm^2, for a reduced number of laser pulses, 10. In both cases, at visual inspection (figure 5.9a), the cleaning efficiency of the spot increased. In particular, a shine boundary region was evident. Figures 5.9b-e show the SEM top-view analysis of this zone for the exposure sites at 400 mJ/cm^2 (b,c) and 900 mJ/cm^2 (d,e). In figures 5.9b and d the presence of C contaminated and Rh cleaned regions can be appreciated. Rh cleaned zones at higher

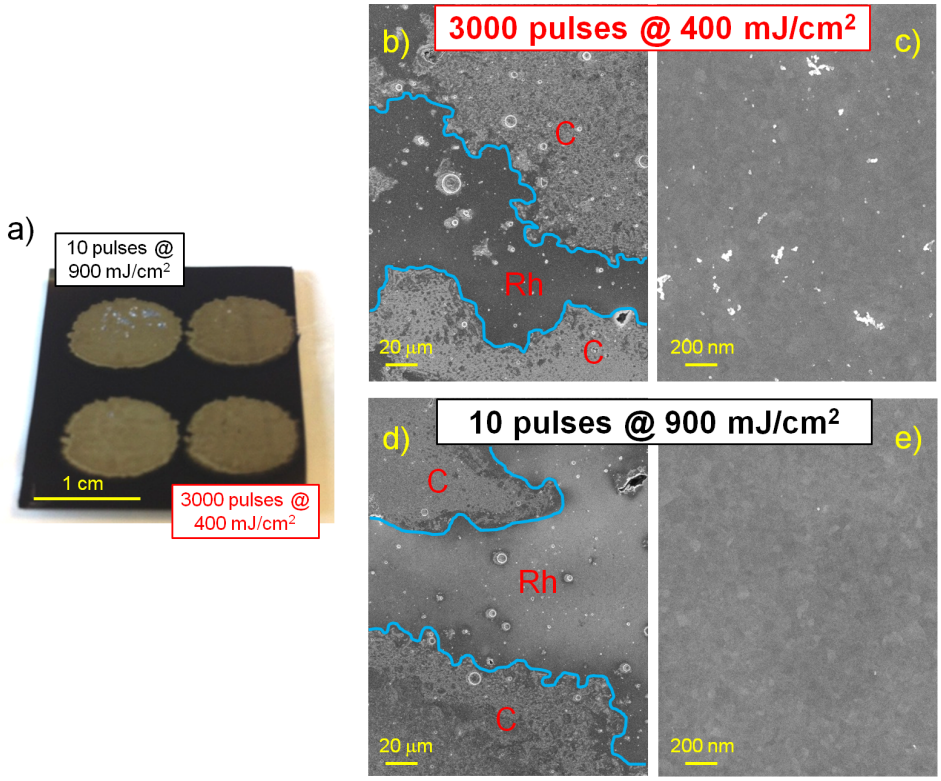

Figure 5.9: *Photograph of the laser cleaned C quasi-film contaminated columnar Rh coating at different laser fluences per pulse and for different numbers of laser pulses (a). SEM top-view images of the boundary region of the site exposed at 400 mJ/cm² for 3000 pulses: low (b) and high (c) magnification. SEM top-view images of the boundary region of the site exposed at 900 mJ/cm² for 10 pulses: low (d) and high (e) magnification.*

magnitude are shown in figures 5.9c and e. The typical crystallinity of the highly-oriented polycrystalline Rh film (see figure 5.5a) is evident, with very few remnant nanometric C particles. Despite the two exposure approaches used significantly different parameters, the two irradiated spots were very similar. The boundary laser-cleaned zone was narrow and pretty inhomogeneous, while the adjacent regions were still covered by C particles and aggregates. The indented profile of the C covered regions suggested that, besides the direct ablating action of the laser pulses, mechanical exfoliation of the contaminant film potentially played a role in the laser cleaning process. One of the possible sources of inhomogeneity

of the Rh cleaned zones could be related to spatial non-uniformities of the laser pulse employed. The main difference between the two exposure conditions investigated was the effect onto the Rh substrate. Only the irradiation at a lower fluence per pulse with a high number of laser pulses allowed the preservation of the integrity of the Rh substrate on the whole surface (figure 5.10a). In the case of the exposure to 10 laser pulses at 900 mJ/cm^2, the onset of a severe damage of the columnar Rh film was evident from both visual inspection (figure 5.9a) and further SEM analyses (figure 5.10b). Therefore, the cleaning approach by means of 3000

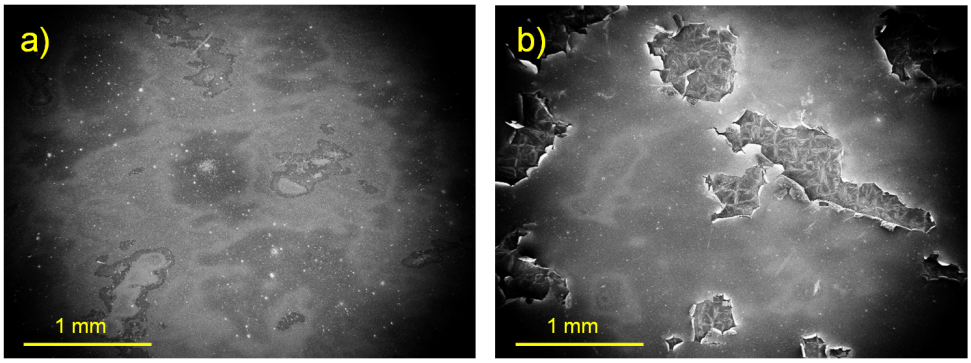

Figure 5.10: *SEM top-view images at very low magnitude of the laser cleaned C quasi-film contaminated columnar Rh coating at 400 mJ/cm^2 for 3000 pulses (a) and at 900 mJ/cm^2 for 10 pulses (b).*

laser pulses at 400 mJ/cm^2 seemed to be more suitable to clean C quasi-films without compromising the highly-oriented polycrystalline Rh films surface.

To investigate how the spatial laser beam profile influenced the cleaning process, PLD target rotation was exploited. The motion of the treated sample should have mitigated the effects of laser pulse non-uniformities, determining a more uniform laser heat load distribution onto the exposure site and a successive enhancement of C contaminants removal. The rotation velocity was fixed to 11 rpm to minimize the overlapping of the adjacent laser pulses. Since 400 mJ/cm^2 and 3000 pulses gave the best results in terms of integrity and cleaning of the columnar Rh substrate, these parameters were chosen to test the laser exposure with sample rotation. The Rh cleaned boundary region seemed to be wider at visual inspection (figure 5.11a). SEM top-view images of the peripheral zone associated to static and rotated exposure for 400 mJ/cm^2 and 3000 pulses are reported in figures 5.11b and c, respectively. The rotated exposure

significantly increased the laser cleaning efficiency. Indeed, the two SEM images show that the dimension of the region in which rhodium substrate can be observed is much more extended rotating the sample.

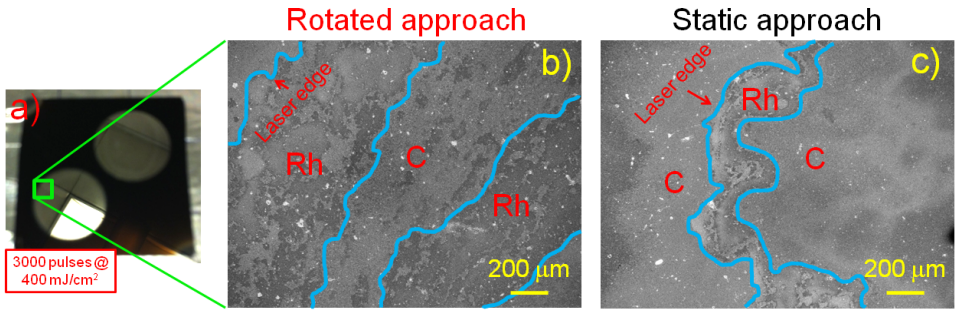

Figure 5.11: *Photograph (a) and SEM top-view image (b) of the C quasi-film contaminated columnar Rh coating cleaned with 3000 laser pulses at 400 mJ/cm^2 using the rotated configuration. Comparison with a SEM top-view image of the same system cleaned by means of the static approach (c).*

It is clear that the main property for a mirror is the specular reflectivity. For this reason, the rotated spot cleaned with 3000 pulses at 400 mJ/cm^2 (figure 5.11a) was measured by ellipsometry in the same manner described in section 4.2 for the Rh films exposed to the deuterium plasma. The results are reported in figure 5.12. The specular reflectivity of the cleaned site (red line) tends to that of the Rh coating as deposited (black line) in the infrared region of the electromagnetic spectrum (R_{Spec} recovery of ~91.6% on average). However, the specular reflectivity drop of ~20% in the UV-vis regime is not acceptable in the context of ITER FMs since they will have to maintain high performance during their operational lifetime.

The natural continuation of the laser cleaning activity consisted in optimizing the procedure elaborated so far in order to extend the cleaned area to the overall PLD Rh mirrors surface (2.6×2.6 cm^2). For this purpose, a sample handling procedure, the so-called "snake pathway" technique, was developed. It allowed to treat areas of some square centimeters in few minutes, exploiting the motors system of the target holder of the PLD apparatus (see subsection 2.4.2). A sketch of the procedure is represented in figure 5.13. The laser spot path is highlighted with green and red arrows on C contaminated Rh film mirror. The vertical motor of the PLD target holder permitted to move the sample with a selected velocity v_y. The laser spot thus described a vertical stripe (green arrow). At the end of the sample, the irradiation was interrupted and the film proceeded forward by a pre-determined step Δx (red arrow), exploiting the motor of the target

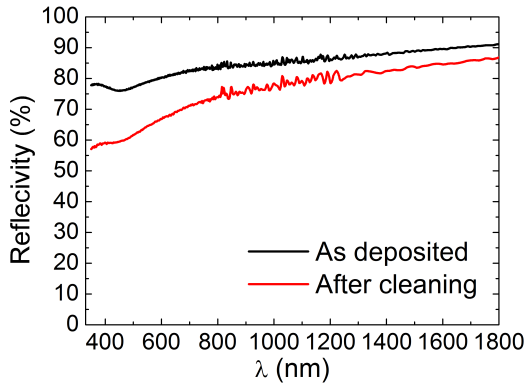

Figure 5.12: *Specular reflectivity measured by ellipsometry in the λ range 330-1800 nm for the highly-oriented Rh film as deposited (black line) and cleaned from C quasi-film with 3000 laser pulses at 400 mJ/cm^2 exploiting the rotated configuration (red line).*

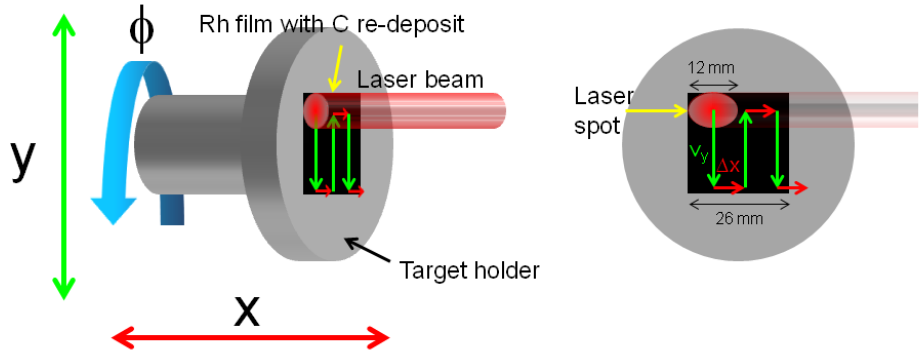

Figure 5.13: *Scheme of the "snake pathway" procedure. The laser spot path is highlighted with green and red arrows on C contaminated Rh film mirror.*

holder which acts along the direction parallel to its axis. The laser was switched on again and another vertical cleaning stripe, this time in the opposite way, was performed. The procedure was repeated until all the sample surface was treated. Moreover, the PLD target holder could be rotated by an arbitrary angle ϕ. This feature gave the possibility to clean the contaminated film along different directions. For example, after the first laser snake pathway, rotating by 90° the target holder and repeating the procedure, a vertical and a successive horizontal laser cleaning scan could be carried out. It is clear that the elaborated snake pathway

technique foresaw three degrees of freedom: the vertical velocity v_y, the horizontal step Δx and the angle of rotation ϕ. In particular, the parameter Δx had to be chosen lower than the major axis of the elliptical laser spot (as described in subsection 2.4.2, the formerly circular laser beam hits the PLD target holder at 45°), in order to guarantee the overlapping of the drawn laser vertical stripes and therefore the cleaning of the whole surface of the film.

The snake pathway procedure was firstly applied to the system extensively discussed in this section, that is the C quasi-film contaminated columnar Rh coating. The 2.6×2.6 cm^2 surface of the film was cleaned in less than 5 min with a single scan of infrared pulses at 400 mJ/cm^2, choosing v_y 4 mm/s and Δx 3 mm. It was shown that the value of 400 mJ/cm^2 was very close to the $\Phi_{Rh,c}$ for 3000 laser pulses. The couple 4 mm/s and 3 mm for v_y and Δx, respectively, determined that the total number of pulses per site was 92, well below 3000, thus ensuring the integrity of the columnar Rh substrate. Figure 5.14 shows the photograph and the corresponding specular reflectivity measured by the spectrophotometer (appendix A.1.1) for the columnar Rh coating as deposited (I, blue line), contaminated with C quasi-film (II, black line) and cleaned with infrared pulses (III, red line). From photograph III, it is straightforward to notice that C contaminant was almost completely removed. Nonetheless, a brownish halo was still present on the surface of the Rh film. Comparing lines II and III, the R_{Spec} recovery is evident on the entire wavelength range. As in figure 5.12, the specular reflectivity of the cleaned sample is however satisfactory only in the infrared region (R_{Spec} recovery of ∼90.3% on average). It is anyway important to stress how the snake pathway technique extended the results of figure 5.12 to an area approximately five times larger.

As previously described, the outcomes of a particular laser cleaning procedure strictly depend on the wavelength of the laser pulses employed. This is primarily due to the fact that different wavelengths imply different physical and chemical mechanisms involved in the interaction between the laser pulses and the irradiated material. One potential solution to increase the specular reflectivity recovery of the IR cleaned columnar Rh mirror of photograph 5.14III consisted in exposing it to further laser pulses with a different λ [89]. Exploiting the fourth harmonic generator system of the laser source employed, the considered C/Rh sample was exposed to a scan of UV pulses with wavelength 266 nm and fluence per pulse 170 mJ/cm^2. The parameters v_y and Δx were maintained unchanged: 4 mm/s and 3 mm, respectively. The results of this trial are summarized by the

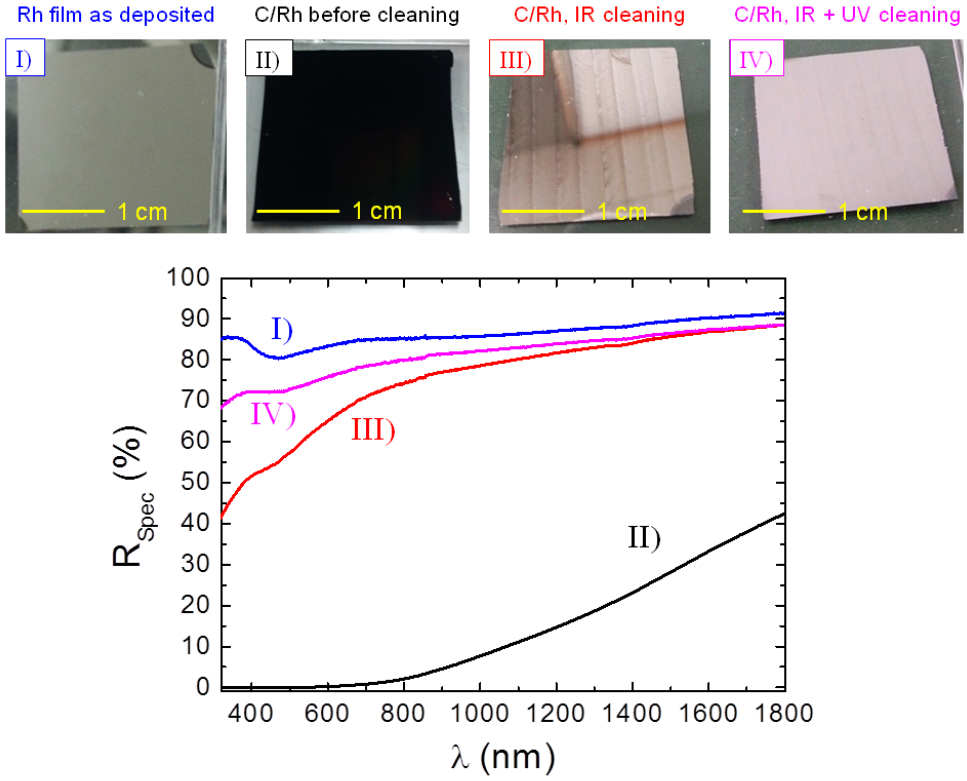

Figure 5.14: *Photograph and corresponding specular reflectivity measured by spectrophotometer in the wavelength range 330-1800 nm for the highly-oriented polycrystalline Rh film as deposited (I, blue line), contaminated with C quasi-film (II, black line) and cleaned with a single scan of IR pulses (III, red line) plus a single scan of UV pulses (IV, purple line), by means of the snake pathway technique.*

photograph and the specular reflectivity labeled with IV in figure 5.14. The brownish halo was present no more on the surface of the sample and its specular reflectivity increased up to ∼30% in the UV-vis region.

In order to demonstrate the effectiveness, reliability and robustness of the laser cleaning procedure elaborated so far, it was applied to remove a low adhered compact C film from a 2.6×2.6 cm^2 highly-oriented polycrystalline Rh coating. By means of the snake pathway technique, the sample was irradiated by a single scan of 400 mJ/cm^2 infrared laser pulses, with v_y 4 mm/s and Δx 3 mm. Figure 5.15 reports the photograph and the corresponding specular reflectivity measured by the spectrophotometer for the columnar Rh coating as deposited (I, blue line), contaminated with a low adhered compact C film (II, black line) and cleaned with infrared

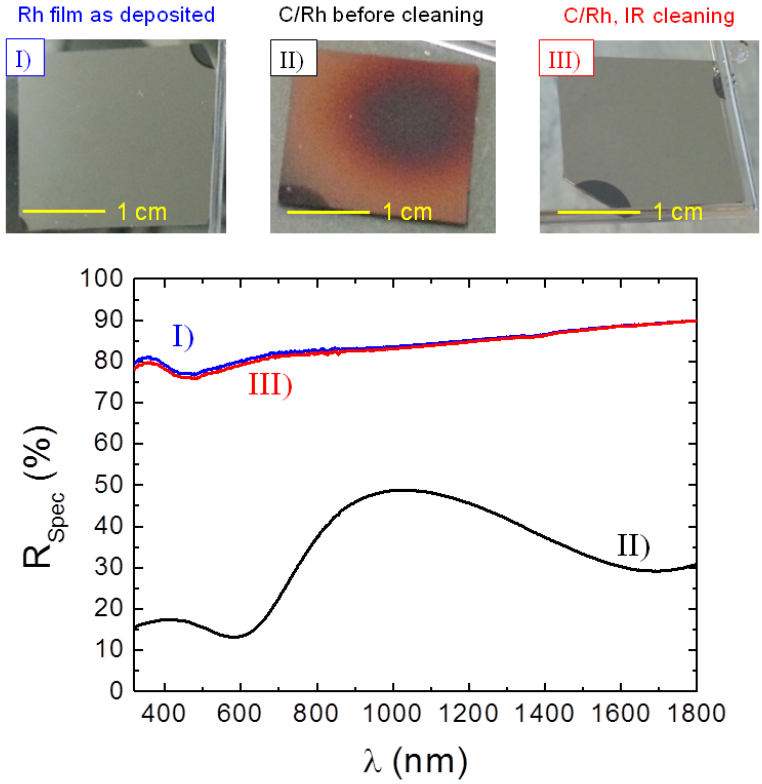

Figure 5.15: *Photograph and corresponding specular reflectivity measured by spectrophotometer in the wavelength range 330-1800 nm for the highly-oriented polycrystalline Rh film as deposited (I, blue line), contaminated with a low adhered compact C film (II, black line) and cleaned with a single scan of IR pulses (III, red line), by means of the snake pathway technique.*

laser pulses (III, red line). Firstly, comparing photographs and specular reflectivity behaviours II of figures 5.15 and 5.14, it is clear how a different morphology of the PLD tokamak-like film affects its appearance and optical properties. In the case of the low adhered compact C film, a single scan of IR pulses was enough to remove all the contaminant from the columnar Rh film. This is evident both from its photograph and specular reflectivity (figure 5.15III). In particular, the R_{Spec} recovery is complete on the entire wavelength range ($\sim$99% on average). There was no need of a further scan with UV laser pulses. This was potentially due to the scarce adhesion of the compact C contaminant to the columnar Rh substrate.

6

Tiles profiling at JET: development of an interpretative tool

In this chapter, the main results obtained during a three months period (July-October 2013) at the Joint European Torus (JET, Culham, Oxfordshire, United Kingdom), will be presented. JET is the largest operative tokamak, the closest to ITER in terms of dimension, plasma performance and, from 2010, PFCs, due to a re-configuration within the frame of the ITER-Like-Wall project (ILW). My activity at JET was focused on the topic of post-mortem characterization of JET PFCs, or "tiles". Post-mortem characterization of JET tiles has the aim of acquiring information about JET first-wall erosion and re-deposition, in terms of erosion depth, nature and thickness of re-deposits, etc. In section 5.2, the production by PLD of contaminants with features resembling those foreseen in ITER was discussed. It is clear that the results of post-mortem characterization of JET tiles could help to reproduce them more faithfully, especially after the beginning of the ILW project. Among the post-mortem characterization techniques, tiles profiling allows to evaluate the erosion and re-deposition pattern of the tiles, in terms of erosion depth and re-deposits thickness, on a macroscopic scale. In order to solve the main concerns associated to this technique, an interpretative tool for tiles profiling measurements was developed and preliminary tested on divertor tiles installed in JET during the first ILW campaign of 2011-2012. Relevant information about the thickness of contaminants deposited above these PFCs, particularly important in the frame of tokamak-like re-deposits production by PLD, was obtained.

The main features of JET-ILW and post-mortem characterization tech-

niques used to analyze first-wall tiles retrieved from JET chamber after experimental campaigns will be discussed in section 6.1. Tiles profiling will be described in section 6.2. The interpretative tool developed for tiles profiling measurements will be explained in section 6.3. Finally, in section 6.4, the results of its application on two divertor tiles exposed to JET plasma will be reported.

6.1 ITER-Like-Wall project at JET

2010 constitutes a turning point in the worldwide nuclear fusion scenario: JET was converted from an all-carbon (figure 1.7) to an all-metal device [27] (figure 6.1a). This new configuration is known as ITER-Like-Wall (ILW) since it is designed to help to predict the behaviours of ITER (see subsection 1.6.2). ILW is characterized by beryllium in the main chamber and tungsten in the divertor. In detail, the transition from all-C wall to ILW consisted in changing graphite and CFC tile elements to bulk Be, Be coated inconel or W coated CFC tiles in the main chamber and W coated CFC with one row of bulk W in the divertor. The first JET-ILW campaign took place during 2011-2012. It was followed by an intervention where a set of tiles from the main chamber and divertor were retrieved from the vessel for post-mortem analyses [128]. They include Ion Beam Analysis (IBA) methods, cross-section microscopy and tiles profiling. To obtain an overall picture about the erosion and re-deposition of JET first-wall, it is necessary to exploit all the post-mortem characterization techniques, integrating the acquired information in a suitable way. Among them, tiles profiling [129–131], in which a stylus comes in contact with the tile at pre-determined points evaluating its profile on a macroscopic scale, allows to classify JET first-wall into erosion- and re-deposition-dominated zones. This information, properly extrapolated to ITER, could also support the ITPA-SWG in the selection of FMs features (i.e. material, configuration, thickness, etc.), depending on their location on ITER first-wall.

6.2 JET tiles profiling and related issues

A set of tiles profiling data relative to divertor and main chamber tiles installed in JET during the first ILW campaign of 2011-2012 was available. In detail, the profiled tiles were upper and mid-plane inner wall guard limiter tiles, upper dump plates, outer poloidal limiter tiles and divertor tiles 1, 3, 4, 6, 7 and 8. Figure 6.1b shows their poloidal location in JET.

Once received from the vessel, a detailed photographic surface study was also performed for each tile. In this chapter, only the divertor tiles will be considered.

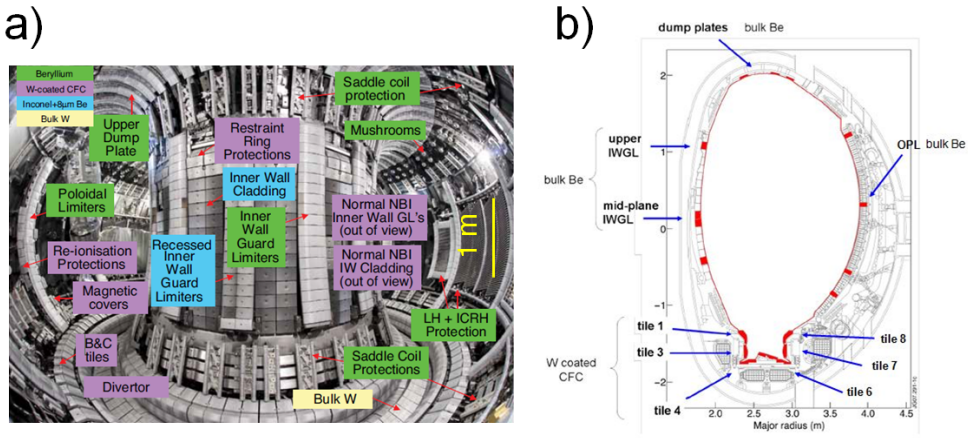

Figure 6.1: *Photograph of JET ITER-Like-Wall (a): the main components and their composition are reported. Poloidal cross-section of JET ITER-Like-Wall vessel (b): tiles measured by the profiling system are indicated.*

Tiles profiling system consists of a X-Y table and a Z probe (figures 6.2a and b). The tile to be profiled is mounted onto the X-Y table and moved with an accuracy of approximately 1 μm using two stepper motors according to a pre-determined sequence of (X,Y) coordinates thus forming a measurement grid. At each grid point the Z probe is extended until the contact with the surface of the tile and a relative height value is recorded. As a result, a cloud of points which represents the tile surface is obtained (figure 6.2c). A typical profiling grid for a divertor tile consists of up to 350 points and the distance between two adjacent points is 5 mm along both the directions. This choice constitutes a good compromise among measurement accuracy and time. Depending on the shape of the tile, the X-Y grid is selected in such a way that it has 35 and 10 points along JET poloidal and toroidal directions, respectively. Repeated measurements provide profile accuracy within few microns in Z direction. The major source of measurement error arises from the positioning of the tile on the X-Y table. On horizontal surfaces this error is minimal, however it could become significant where the tiles surfaces have sloped curvatures. From simple trigonometry the error in the height is 0.18 μm per micron misalignment on a surface at 10° to the horizontal. The positioning misalignment could include one to three shifts along the three space

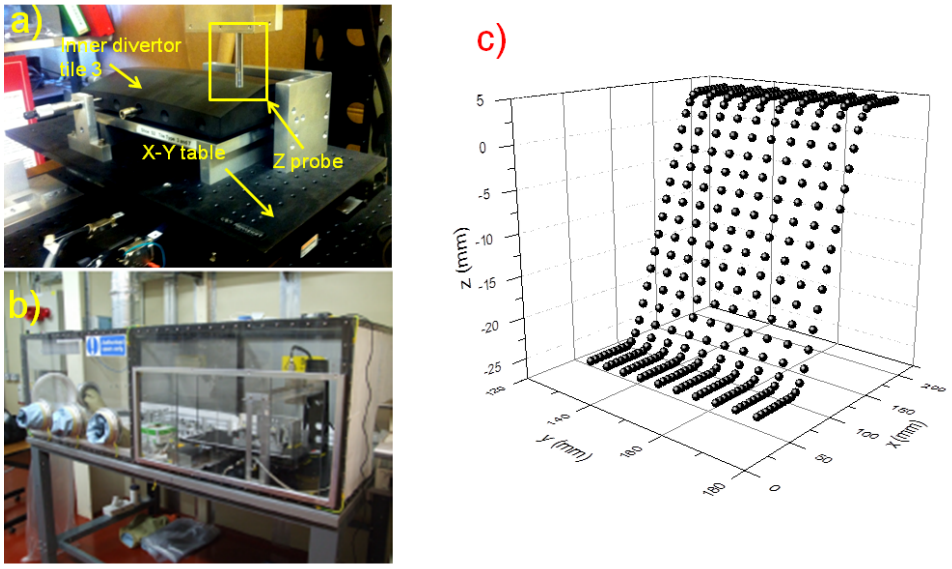

Figure 6.2: *Tiles profiling equipment used at JET (a). This system is sealed in a suitable casing necessary to handle beryllium (b). Profiling measurement outcome relative to inner divertor tile 4 (c).*

directions and one to three tilts with respect to the three tile rotation axes. Presently, measurement of a single tile is considered accepted when three sequential profiling measurement results, including re-positioning of the tile, are statistically within 5 μm of each other.

By subtracting the profile of the tile measured before its installation in JET chamber to that acquired after its exposure to JET plasma, an evaluation of the erosion and re-deposition pattern of the tile, in terms of erosion depth and re-deposits thickness, can be obtained. It is clear that a positioning error between the two tile profiling measurements performed before and after its exposure could introduce misleading artifacts into the estimated erosion/re-deposition pattern, thus complicating its interpretation. Moreover, during 2010 the stylus of JET profiling system was bent of $\sim$405 μm both in X and Y directions as a consequence of personnel oversight. Some of the bare divertor tiles here considered were measured before the stylus crash. In order to perform profiling measurements in the same experimental conditions before and after tiles installation for 2011-2012 JET-ILW campaign, hence avoiding the misalignment of $\sim$405 μm along both the profiling table directions, the profile of most of the virgin tiles was reassessed with the stylus bent.

6.3 An interpretative tool for tiles profiling measurements

With the aim of solving the misalignment issues, we decided to follow a numerical approach. We thus developed a MatLab routine in order to estimate the shift between tile positioning and re-positioning for the profiling measurements performed before and after tile exposure in JET experiments. Once the shift was determined, tile erosion/re-deposition pattern was evaluated with high accuracy. The code was then applied to the available data set of profiling measurements of inner divertor tiles 1, 3, 4 and of outer divertor tiles 6, 7, 8.

The hypothesis on which the approach was based consisted in the symmetry of divertor tiles erosion/re-deposition pattern along JET toroidal direction. By means of this assumption the misalignment concerns reduced to a bi-dimensional (2D) problem: a misalignment along the direction X or Y of the profiling table representing JET poloidal direction, generally labeled as x, a misalignment along the Z vertical direction of the profiling system, renamed as z, and a tilt in the x-z plane with respect to the tile centre, θ. The 3D cloud of points measured by the profiling system became a set of points in the x-z plane (figure 6.3). The 2D hypothesis permitted to focus on only one toroidal coordinate for each divertor tile.

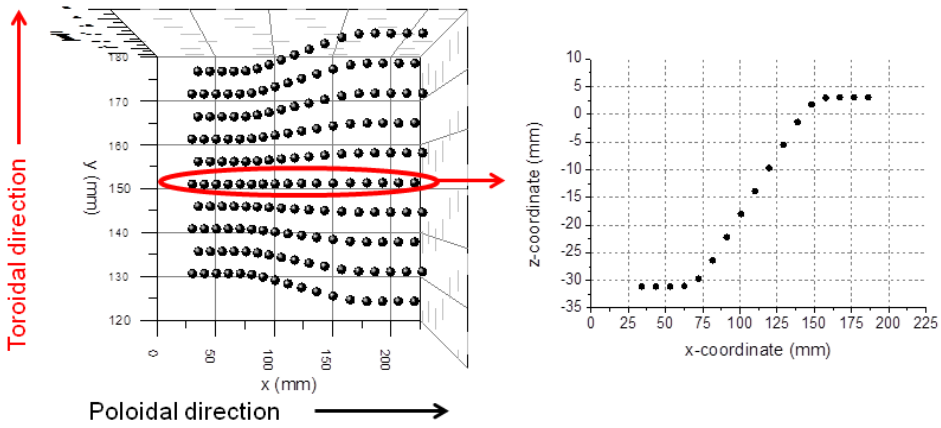

Figure 6.3: *Thanks to the 2D assumption it was possible to focus on only one toroidal coordinate for each divertor tile. The case here reported is relative to inner divertor tile 4.*

In order to evaluate the actual misalignment and erosion/re-deposition pattern of JET tiles, the selected approach minimized the distance along

vertical direction z between the points of the profiles of the considered tile measured before and after its exposure. In this way, the estimated tile erosion/re-deposition pattern was characterized by minimum values for erosion depth and re-deposits thickness. However, if the real erosion and re-deposition pattern of the tile had a constant background, its quantitative evaluation from profiling measurements constituted a hard task and hence cross-section microscopy was mandatory for calibrating the height of tile erosion/re-deposition pattern obtained by the developed numerical approach.

The elaborated MatLab routine was based on the following alignment procedure. The profile of the tile measured after its exposure was moved by a user-defined shift Δx along x, Δz along z and tilted by an angle θ with respect to the tile centre (figure 6.4). These three quantities identified a shift triplet (Δx,Δz,θ). To estimate wether the triplet (Δx,Δz,θ)

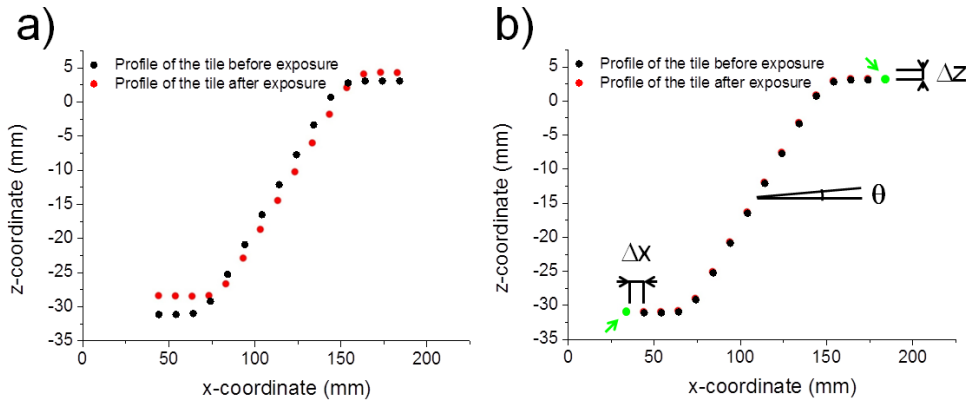

Figure 6.4: *Profile of inner divertor tile 4 before (black dots) and after (red dots) its exposure as measured by the profiling system (a). A shift of Δx along x, Δz along z and a θ tilt with respect to the tile centre are imposed to the profile of the tile measured after the exposure (b). Green dots indicate the points of the two profiles excluded by the alignment procedure.*

minimized the distance along z between the points of the profiles of the tile measured before and after its exposure, the classical standard deviation formula was rearranged as follows:

$$\sigma_{\mathrm{m}} = \sqrt{\frac{\sum_{\mathrm{i}=1}^{\mathrm{N}} \left(\mathrm{z}_{\mathrm{after,i}} - \mathrm{z}_{\mathrm{before,i}}\right)^2}{\mathrm{N}}} \tag{6.1}$$

where the sum ran over the N points of the two profiles with identical x-values (the points of the two profiles with different x-values were ex-

cluded by the alignment procedure; they are represented by green dots in figure 6.4b). $z_{before,i}$ and $z_{after,i}$ were the i-th z-values of profiling measurements performed before and after tile exposure to JET plasma. The shifted profile of the tile measured after the exposure which fitted at best the profile acquired before the exposure was that with the minimum σ_m. The corresponding shift triplet represented the actual positioning error between the two profiling sessions carried out on the tile before and after its exposure. In order to find the shifted profile after exposure with minimum σ_m, the shift triplet spanned the region of the space Δx-Δz-θ with sides 2Ux, 2Uz and 2Uθ, centred at the origin. +Ux (-Ux), +Uz (-Uz) and +Uθ (-Uθ) were the upper (lower) limits of Δx, Δz, and θ. The minimum increment of the shift triplet was δx, δz, $\delta\theta$ along Δx, Δz and θ directions, respectively. A sketch of this procedure is shown in figure 6.5. The quantities Ux, Uz, Uθ, δx, δz, $\delta\theta$ were all defined by the user. The

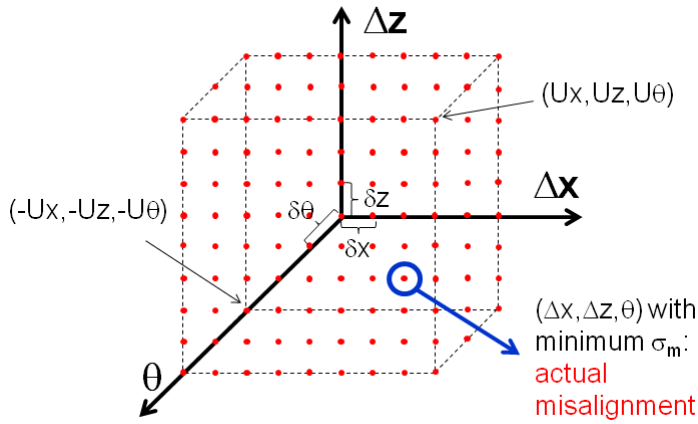

Figure 6.5: *Investigated region of the space Δx-Δz-θ. It is a parallelepiped lattice, centred at the origin, with sides 2Ux, 2Uz and 2Uθ. The distance between two adjacent points is δx, δz, $\delta\theta$ along Δx, Δz, θ directions.*

Erosion/Re-deposition pattern (ER) was finally obtained subtracting the profile measured before tile exposure to the best shifted profile acquired after tile exposure (figure 6.6):

$$ER_i = z_{after,i} - z_{before,i} \tag{6.2}$$

Equation 6.2 implied that positive values for the erosion/re-deposition pattern correspond to re-deposition and, conversely, negative values correspond to erosion.

With the goal of evaluating tiles misalignment with an accuracy of some

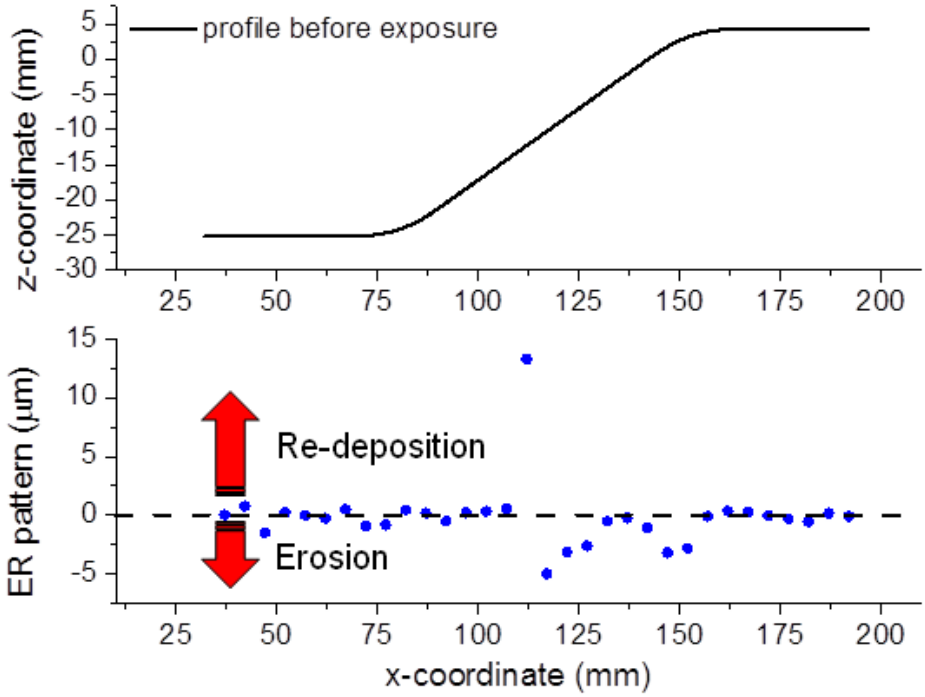

Figure 6.6: *Top panel represents the profile of inner divertor tile 4 measured before the exposure (a black line is used as eye guide instead of dots). With the same x-axis, the erosion/re-deposition pattern evaluated by the alignment procedure is shown in the bottom panel.*

microns and some hundredth of degree, the number of points acquired by the profiling system along the poloidal direction for the divertor tiles (up to 35) was not sufficient. The profile of the tiles measured before the exposure was therefore interpolated by the spline method to have approximately 170000 points 1 μm afar.

To estimate the validity of the hypothesis of divertor tiles erosion and re-deposition symmetry along the toroidal direction, the following approach was exploited. The alignment procedure described so far was applied to all the profiled toroidal coordinates of the considered tile. For each toroidal coordinate, the best shift triplet and erosion/re-deposition patter were evaluated (figure 6.7a). The overall misalignment triplet, $(\overline{\Delta x}, \overline{\Delta z}, \overline{\theta})$, and erosion/re-deposition pattern were successively estimated as the average on the misalignments and as the average on the erosion/re-deposition patterns of each toroidal coordinate. Finally, the standard deviation associated to the average erosion/re-deposition pattern was evaluated in cor-

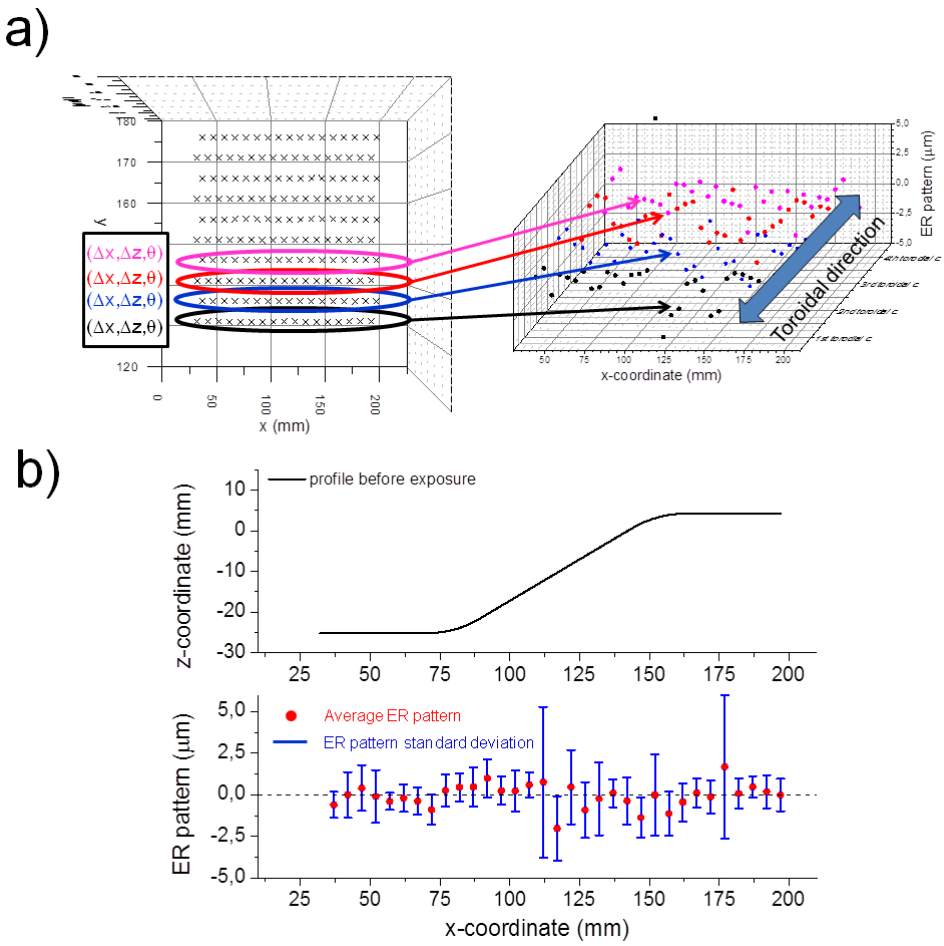

Figure 6.7: *Analyses and outcomes of each toroidal coordinate for inner divertor tile 4 (a). Average erosion/re-deposition pattern (red circles) and standard deviation bars (blue bars) (b). The latter are clearly on the order of the profiling system accuracy and the 2D hypothesis is thus satisfied.*

respondence of each profiling poloidal grid point (figure 6.7b). The 2D hypothesis was considered fulfilled if the values of the erosion/re-deposition pattern standard deviation were comparable with the profiling system accuracy along the z direction of some microns.

6.4 Evaluation of JET tiles erosion/re-deposition pattern

As discussed before, the numerical approach described in section 6.3 was applied to inner divertor tiles 1, 3, 4 and to outer divertor tiles 6, 7, 8 in order to get information about the overall JET divertor erosion and re-deposition pattern. Figure 6.8 shows a magnification of image 6.1b representing JET-ILW divertor. In this section, only the results referred

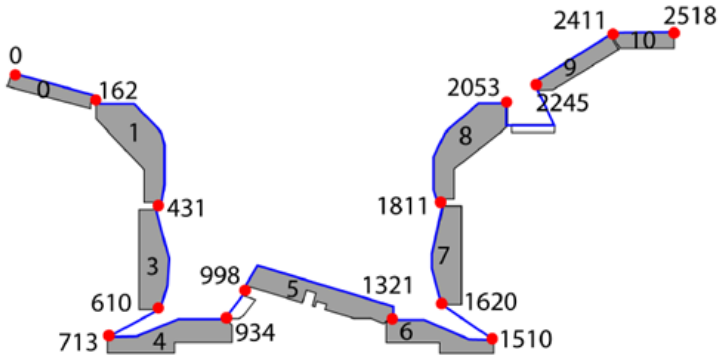

Figure 6.8: *Scheme of JET-ILW divertor. The numbers reported outside the tiles represent the "s coordinates" of JET-ILW divertor. They are the distances around the divertor tiles surfaces, from inboard to outboard.*

to tiles 1 and 6, representative of inner and outer divertor, respectively, will be reported. The cases of inner divertor tiles 3, 4 and of outer divertor tiles 7, 8 will be discussed in appendix C. Figures 6.9a, 6.10a show the photographs of tiles 1 and 6 after 2011-2012 JET-ILW campaign, together with the grids employed to perform the profiling measurements. The actual location of the considered tile in JET divertor, in terms of the neighboring tiles, is indicated, as well. Figures 6.9b, 6.10b show the results of the numerical approach for both tiles. The interpolated profiles of the tiles before their exposure are reported in the top panels, while in the bottom ones the average erosion/re-deposition patterns and the corresponding standard deviation bars are displayed. For tiles 1 and 6, it is clear that the standard deviation bars keep within the order of the profiling system accuracy. The bi-dimensional hypothesis of the symmetry of the divertor tiles erosion and re-deposition along the toroidal direction was thus well satisfied.

The photograph of inner divertor tile 1 after its exposure to JET

pulses (figure 6.9a) shows an evident groove which occurred during the transportation of the tile from the chamber to the IBA facility for the other post-mortem characterizations. Albeit this damage was not the result of JET plasma erosion, it was exploited to validate the MatLab routine which correctly evaluated the scratch as an "erosion zone" with a depth up to 15 μm (figure 6.9b). Except for the groove, the reconstructed erosion/re-deposition pattern highlights that the tile was in a re-deposition-dominated zone (re-deposits thickness up to 15 μm). This is consistent with the available literature relative to JET previous experimental campaigns with all-C wall, which reports about the asymmetric re-deposition/erosion characteristics of inner and outer divertor legs [49]. Moreover, the latest cross-section microscopy images of tile 1 quantitatively confirm the evaluated erosion/re-deposition pattern of figure 6.9b: a re-deposition of some microns on the left part of the tile and a strong re-deposition more than ten microns on the right part.

Photograph of outer divertor tile 6 (figure 6.10a) displays a dark stripe followed by a lighter one where the tile starts to slope, and a broader dark stripe on the right part. The latter feature is not included in the measurement grid. As it is evident from figure 6.10b, the MatLab routine estimated the region closeness to the left dark stripe as a re-deposition zone with a thickness up to 10 μm and the near light stripe as an erosion zone with a maximum depth of 15 μm. Moreover, an evident re-deposition region (up to 15 μm) followed by an erosion zone (10 μm) could be found in correspondence of the final part of the slope of the tile and at the top flat region, respectively. The presence of adjacent erosion and re-deposition zones in two different regions of tile 6 could not be unexpected, since JET-ILW outer divertor is probably an erosion-dominated zone [49], implying that the erosion of tile 6 could be accompanied by prompt re-deposition.

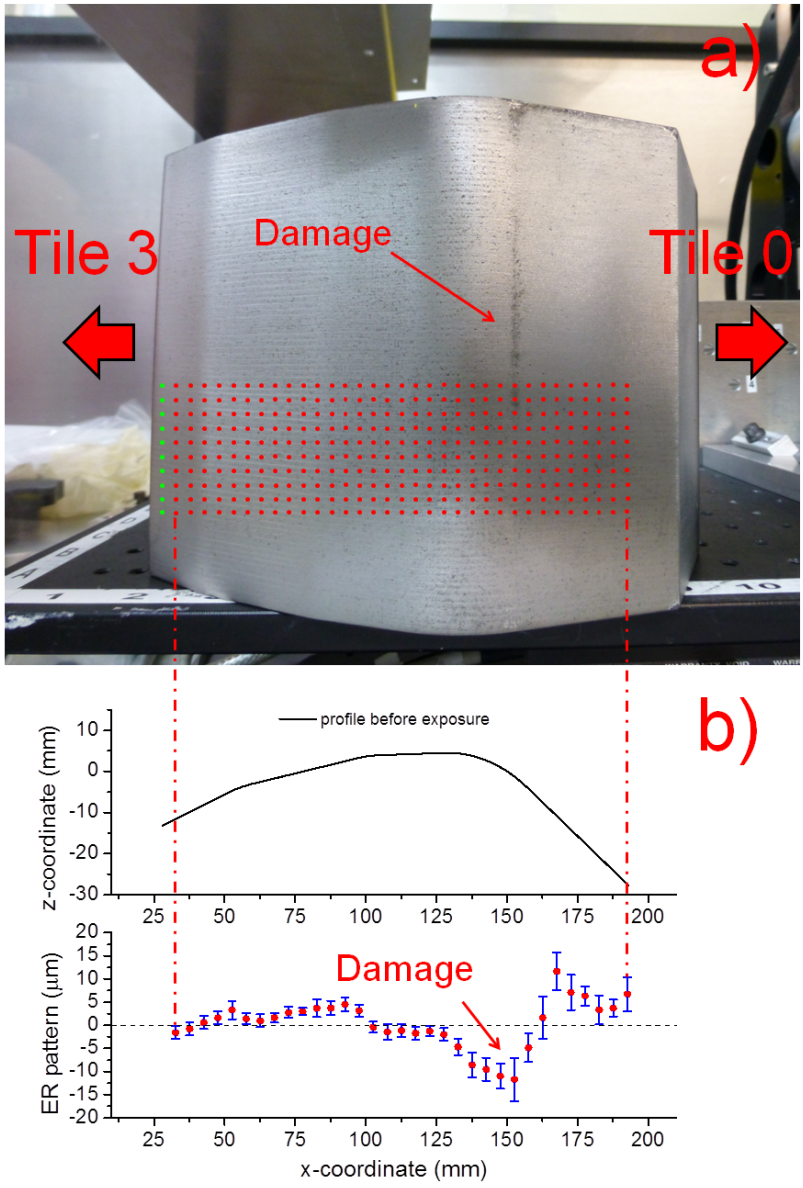

Figure 6.9: *A photograph of inner divertor tile 1 after its exposure, together with the grid used for the profiling measurements (red and green dots; the latter indicate the grid points excluded by the alignment procedure) and a hint of the location of the neighbouring tiles (a). The outcome of the numerical approach (b). The mean shift triplet was (398.8±14.5μm, -34.9±2.3μm, -0.0064°±0.0037°). As tile 1 was measured only earlier the stylus crush before its exposure, the average poloidal shift Δx was on the order of the stylus bent, 405 μm.*

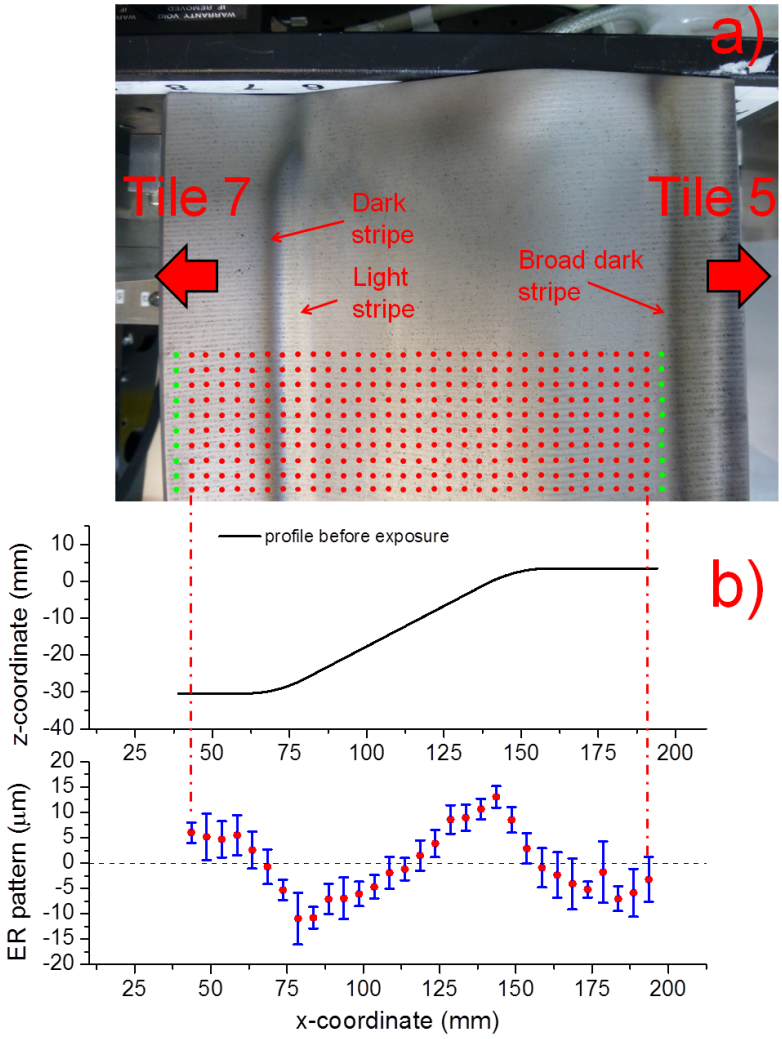

Figure 6.10: *A photograph of outer divertor tile 6 after its exposure, together with the grid used for the profiling measurements (a). The outcome of the numerical approach (b). The evaluated average misalignment was (407±4.8μm, -15.6±1.8μm, -0.0049°±0.0014°). As for tile 1, since the profile of tile 6 was acquired before its exposure only earlier the stylus crash, the mean poloidal shift Δx was on the order of the stylus bent.*

7

Conclusions and perspectives

The main objective of this Ph.D thesis was the study and the development of nanostructured rhodium (Rh) films for the production of diagnostic mirrors employed in nuclear fusion systems.

The concerns related to the construction of nuclear fusion devices are enormous in number, and many years are still necessary for demonstrating the feasibility of producing energy for civil purposes by means of nuclear fusion reactions (Part I: Chapter 1). A possible design solution consists in confining by a complex magnetic fields configuration a deuterium tritium (D-T) mixture brought to the state of thermonuclear plasma. In this frame, the tokamak concept constitutes one of the most investigated approaches. Its peculiar feature is the toroidal shape of the plasma. The foreseeable extreme temperatures ($\sim 10^8$ K) and magnetic fields (some teslas), the characteristic devices for plasma heating as well as the several auxiliary systems, convey the idea of the complexity of the tokamak approach. The international project ITER ("the way" in Latin) aims to demonstrate the feasibility of the tokamak solution and thus to make a major step in the long-awaited transition from experimental studies of plasma physics to full-scale electricity producing nuclear fusion power plants.

The diagnostic system in ITER will play the crucial role of controlling the nuclear fusion process, ensuring at the same time the integrity of its toroidal chamber. Since the extreme temperatures will make a direct contact between the plasma and material probes impossible, many diagnostics will exploit the electromagnetic radiation emitted, reflected or diffused by the thermonuclear plasma, which will reach the measurement apparatuses by complex mirrors labyrinths (Part I: Chapter 2). Some of their most

critical components will be the mirrors placed on the first-wall of the ITER toroidal chamber, called also First Mirrors (FMs). The study and development of these elements belong to the widely investigated branch of Plasma-Wall Interaction (PWI). ITER FMs will endure severe conditions in terms of intense thermal loads, strong radiation fields and high particles fluxes. Among the main effects of this harsh environment on their performance and lifetime, FMs erosion by energetic particles coming from the hot plasma and re-deposition of sputtered material transported from the first-wall onto their surface constitute the highest priority issues. These phenomena could lead to a dramatic decrease of FMs specular reflectivity, posing a serious threat on the operation of the entire diagnostics.

The first objective of this Ph.D thesis consisted in the production of Rh films with suitable properties for ITER FMs by means of Pulsed Laser Deposition (PLD). The deposition process was optimized to produce Rh coatings with a high specular reflectivity on a significant side area of 10 cm^2 (Part II: Chapter 3). This goal was achieved combining the "off-axis" deposition technique and the ablation by high fluence infrared laser pulses (10-19 J/cm^2). The obtained results could be exploited for the production of mock-ups relevant for some type of ITER FM [114, 115]. In general, since a fraction of the ITER diagnostics will employ Rh FMs with a diameter over 20 cm [3], a further improvement of the deposition process is mandatory. In particular, the approaches currently under investigation to make PLD a competitive technique in the industrial field (e.g. by means of multiple laser beams [132]) could be used. The critical issue of film-substrate adhesion was addressed producing and properly characterizing nanoengineered multi-layered Rh coatings. This strategy constitutes an interesting and attractive solution as it is based on a mono-elemental approach. It has been already employed by NanoLab for the production of tungsten films and their mechanical properties under exposure to divertor-like plasmas have been recently investigated. In order to further validate the multi-layer solution, it is crucial to expose Rh films to ITER-relevant radiation fields and thermal loads [133].

Suitable morphology and nanostructure control of the growing film, guaranteed by PLD, was successfully exploited also to improve Rh coatings behaviour under erosion of a pure deuterium plasma with some qualifying features relative to the ITER peripheral plasma facing first mirrors (Part II: Chapter 4). This experimental campaign was performed at the Physics Department of Basel University, in collaboration with the Nanolino group. Specular reflectivity of PLD Rh film with a granular-like morphology and small mean crystallite size (6 nm) maintained rather constant during deu-

terium plasma exposure. This characteristic could be due to the lacking in the formation of rhodium deuteride (RhD_x, $x \leq 2$) sub-superficial layer. Exposure in tokamaks or in proper dedicated machines, like linear devices for simulation of ITER divertor-like plasmas (PSI-2, Pilot-PSI, Magnum, etc.), is however necessary to collect data on PLD Rh films performance in an environment closer to ITER and to obtain conclusive information towards the production of realistic mirror devices.

A further natural continuation of this Ph.D work in the frame of the production of surface mirrors could consist in exploiting the knowledge and the expertise acquired in the deposition of Rh films by PLD with the goal of extending the investigation to other materials relevant for ITER FMs production, as molybdenum and tungsten (an activity to deposit molybdenum mirrors by PLD has been launched during the final months of this Ph.D thesis). Moreover, the study of specific problems relative to mirror devices employed in realistic ITER diagnostics is mandatory to validate the PLD approach.

The second objective of this Ph.D thesis was focused on the study of the laser cleaning technique as a potential method to mitigate the re-deposition of first-wall eroded material onto FMs (Part III: Chapter 5); a novel approach to address this issue with laboratory-scale facilities was developed and primarily tested. In particular, carbon (C) and tungsten carbide (WC) "tokamak-like" contaminants were successfully produced by PLD and deposited onto PLD Rh films. The PLD apparatus was properly modified in order to perform the laser cleaning process. A first set of the main process parameters that rule this technique (the laser wavelength, the fluence per pulse, the number of pulses considered and the atmosphere in which the procedure is done) was chosen in order to conduct a preliminary methodological analysis. Rh films laser damage threshold, i.e. the laser fluence per pulse at which damage occurs on Rh films surface, as a function of number of pulses, was determined. To treat the overall Rh coatings surface ($\sim$10 cm^2), a sample handling procedure was also developed. This solution could be easily scaled to most of the areas relevant for ITER FMs through suitably designed movement systems. Highly-oriented polycrystalline Rh films were cleaned from C "quasi-film" by means of a double wavelength approach, that is a first scan with infrared laser pulses and a second scan with ultraviolet pulses. The achieved specular reflectivity recovery was satisfactory on a wide wavelength range (300-1800 nm). In order to demonstrate the effectiveness and robustness of the elaborated laser cleaning procedure, the extension of these results to different tokamak-like re-deposited C morphologies was necessary. A low adhered

compact C film was thus removed from columnar Rh coatings. In this case, mainly because of the scarce mechanical properties of the considered typology of C contaminant, a single scan with infrared laser pulses was sufficient to totally restore Rh mirrors specular reflectivity. The laser cleaning of PLD WC contaminants is one of the first possible perspectives of this Ph.D thesis. Moreover, other tokamaks plasma facing materials should be considered. Since tungsten (W) and beryllium (Be) have been selected for ITER divertor and main chamber, respectively, the deposition of W, aluminum (Al), magnesium (Mg) and boron (B), with Al, Mg and B as Be-proxy (due to its toxicity), constitutes an attractive option. This investigation could be also conducted through a coordinated activity which exploits the synergy between the results of the post-mortem characterization of tokamaks first-wall tiles and the PLD contaminant production process. In this context, the information acquired during the three months period spent at the Joint European Torus (JET) about the thickness of the re-deposits found on JET first-wall tiles, as measured by tiles profiling and evaluated by the interpretative tool developed (Part III: Chapter 6), can represent a useful starting point.

Besides the two main effects of ITER harsh environment onto FMs performance and lifetime, i.e. erosion and re-deposition, widely investigated in this Ph.D thesis, another important phenomenon as the damage induced by neutron bombardment needs to be taken into account. However, its priority will be as high as that of erosion and re-deposition processes only in the frame of the DEMOnstration power plant (DEMO), whose first operative phase will be optimistically performed in 2040. DEMO is a proposed nuclear fusion power plant that is intended to build upon the expected success of ITER. The objectives of DEMO are usually understood to lie somewhere between those of ITER and a "first of a kind" commercial station. In particular, the expected DEMO's 2-4 GW of thermal output is on the scale of a modern electric power plant. Since the nuclear fusion reactions power of DEMO will be 4-8 times higher than that of ITER, it is clear that the 14.1 MeV neutron flux onto DEMO first-wall will be significantly higher as well. Evaluating first-wall neutron damage in dpa (displacement per atom), 2 dpa expected for ITER will rise to 50-80 dpa foreseen for DEMO. Waiting for the International Fusion Materials Irradiation Facility (IFMIF), an accelerator-based neutron source that will use deuterium-lithium stripping reactions to simulate 14.1 MeV neutrons from D-T fusion reactions, which potentially will start the operation in 2017, one possible technological solution to simulate 14.1 MeV neutrons damage nowadays could consist in irradiating FMs, and in particular PLD Rh

films, with high-energy heavy ions [134]. This could be another interesting perspective of this Ph.D thesis.

A

Characterization techniques

In this appendix some more technical details on the experimental techniques and methodologies adopted in this thesis work will be reported. Since the most important property of mirror devices is their reflectivity, in section A.1 the concepts of specular, diffuse and total reflectivities will be introduced, together with the techniques employed to measure them. Successively, the other characterization methods and the corresponding technological solutions exploited will be discussed. In particular, for morphologic and topographic studies, scanning electron and atomic force microscopies were used and will be described in sections A.2 and A.3. X-ray diffractometry was employed to investigate the structural properties of the examined specimens and it will be explained in section A.4. Finally, to acquire information about the chemical nature of the samples, X-ray photoelectron spectroscopy was exploited and it will be described in section A.5.

A.1 Some notions about optics

Consider a plane electromagnetic wave travelling from medium 1 to medium 2, characterized by different optical properties. At the interface between them, the electromagnetic wave is divided into a reflected and a transmitted (refracted) part (figure A.1). According to the law of reflection, the angle of reflection θ_r is equal to the angle of incidence θ_i. For the transmission angle, the Snell's law says

$$n_1 \sin\theta_i = n_2 \sin\theta_t \tag{A.1}$$

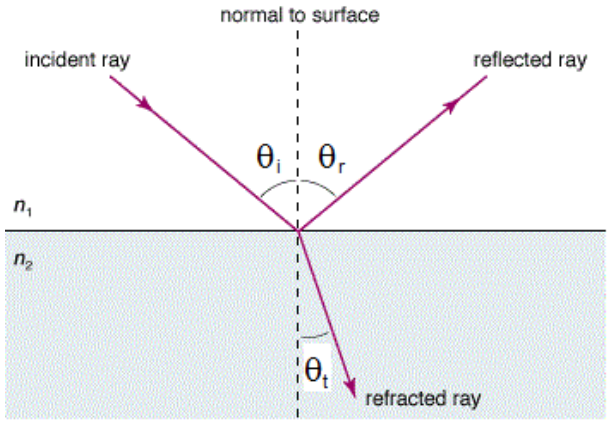

Figure A.1: *Description of the behaviour of an incident plane electromagnetic wave at the interface between two media with absolute refractive index n_1 and n_2, respectively. θ_i, θ_r and θ_t are the angle of incidence, reflection and transmission.*

with n_1 and n_2 the absolute refractive indices of the two media.

The reflectance R is defined as the ratio of the intensity of the reflected light to the intensity of the incident light. Reflectivity is terminologically distinguished from reflectance by the fact that reflectivity is a value that applies to thick reflecting objects. When reflection occurs from thin layers of material, internal reflection effects can cause the reflectance to vary with surface thickness. Reflectivity is the limit value of reflectance as the object becomes thick.

The calculation of the reflectivity R of medium 2 depends on the polarization of the incident light. Two cases are distinguishable:

- the incident light is polarized with its electric field perpendicular to the plane containing incident, reflected and refracted rays (i.e. the plane of figure A.1). The light is said to be s-polarized, from the German word senkrecht which means perpendicular.

- the incident light is polarized with its electric field lied on the plane of figure A.1. The light is said to be p-polarized, from the word parallel.

Assuming that the two media of figure A.1 are linear, homogeneous and isotropic, the application of the Fresnel's equations permits to evaluate the complex reflection coefficients of medium 2, r_s and r_p, and thus the reflectivities, R_s and R_p, for s- and p-polarized light [124]. Finally, the reflectivity R of medium 2 observed for a natural or unpolarized light

(containing an equal mix of s- and p-polarization) is given by

$$R = \frac{R_s + R_p}{2} \tag{A.2}$$

The description made so far is only valid for a perfect surface of the second medium. In the case of a surface that presents a roughness not negligible compared to the wavelength of the light, a fraction of the light bounces of in all directions (figure A.2): this phenomenon is called diffuse reflection. Instead, the reflection described by the Fresnel's equations is known as specular reflection: it denotes the ability of a surface to reflect an image. The angular distribution of the diffuse reflected light strictly

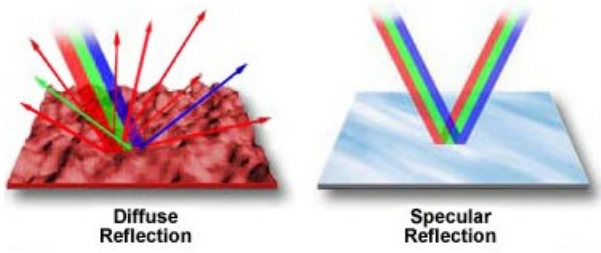

Figure A.2: *Diffuse and specular reflection.*

depends on the structure of medium 2. A common description is the Lambertian reflectivity model in which the surface luminance is considered isotropic. The diffuse (specular) reflectivity is defined as the ratio between the intensity of the light reflected diffusely (specularly) and the intensity of the incident light. The total reflectivity (also called hemispherical reflectivity) is expressed as the sum of both the components:

$$R_{Tot} = R_{Diff} + R_{Spec} \tag{A.3}$$

where R_{Tot}, R_{Diff} and R_{Spec} are the total, diffuse and specular reflectivities, respectively.

A.1.1 UV-vis-NIR Perkin Elmer Lambda 1050 spectrophotometer

Total and diffuse reflectivity measurements were carried out using a UV-vis-NIR Perkin Elmer Lambda 1050 spectrophotometer. A calibrated PolyTetraFluoroEthylene (PTFE) standard plate is exploited as a reference to allow the determination of the absolute values of the sample total

and diffuse reflectivities. The latter are therefore calculated by means of the following expression:

$$R(\lambda) = 100 \times \frac{I_{Sample} - I_{Background}}{I_{Reference} - I_{Background}} \quad (A.4)$$

From this formula it is clear that the measurement of the reflectivity of the sample requires three steps. First, a measurement of the background ($I_{Background}$) is done without the reference plate. Second, the reference plate is measured ($I_{Reference}$). Third, since the spectrophotometer is thus calibrated, the sample can be measured (I_{Sample}).

The spectrophotometer is equipped with a 150 mm diameter integrating sphere (also called Ulbricht's sphere) which permits the measurement of the reflectivity in the wavelength range 180-2500 nm. The sphere is coated with PTFE which has a total reflectivity close to 100% over the whole working λ interval and is assumed to have a perfect Lambertian diffuse reflectivity. As just mentioned, thanks to the geometry of the integrating sphere, this spectrophotometer allows to measure both the total and the diffuse reflectivity. To determine the former, the incident light beam arrives on the sample with an angle of $\sim 8^\circ$ and strikes the inner wall of the sphere after reflection on the sample. The removal of the part of the integrating sphere hit by the specular component of the reflected beam allows the measurement of the diffuse reflectivity. Specular reflectivity is finally estimated by subtracting the diffuse reflectivity from the total reflectivity.

A.1.2 Varian Cary 5 UV-vis-NIR spectrophotometer

Besides the UV-vis-NIR Perkin Elmer Lambda 1050 spectrophotometer, also a Varian Cary 5 UV-vis-NIR spectrophotometer was used to measure total and diffuse reflectivity of the examined specimens. Even in this case a calibrated PTFE standard plate is exploited as a reference to allow the determination of the absolute values of the sample reflectivities. The latter are calculated by means of the following expression:

$$R(\lambda) = 100 \times \frac{I_{Sample} - I_{Background}}{I_{Reference} - I_{Background}} \quad (A.5)$$

Again, from this expression, it is evident that the measurement of the reflectivity of the sample requires three steps. First, a measurement of the background ($I_{Background}$) is done by blocking the incident light. Second, the reference plate is measured ($I_{Reference}$). Third, since the spectrophotometer is thus calibrated, the sample can be measured (I_{Sample}).

The spectrophotometer is equipped with a 110 mm diameter integrating sphere which permits the measurement of the reflectivity in the wavelength range 250-2500 nm. The sphere is coated with PTFE which has a total reflectivity close to 100% over the whole working λ interval and is assumed to have a perfect Lambertian diffuse reflectivity. To determine the total reflectivity, the incident light beam arrives on the sample with an angle of $\sim 3^\circ$ and strikes the inner wall of the sphere after reflection on the sample. To measure the diffuse reflectivity, the incident beam arrives on the surface with a normal incidence so that the direct reflected beam comes out of the sphere without being measured. Specular reflectivity is calculated by subtracting the diffuse reflectivity from the total reflectivity.

A.1.3 SENTECH SE 850 ellipsometer

Ellipsometry is a widely used non-destructive method for the determination of the optical properties of materials and for the assessment of thin films thickness. The first ellipsometer was designed by Rothen in 1945 [135], albeit the study of the polarization of light and its modifications after reflection (or transmission) was started much earlier on. An incident plane-polarized light beam which is reflected at the interface between two media at some oblique angle generally becomes elliptically polarized. Ellipsometry measures the change in the polarization state of the light and interprets it in terms of the physical properties of the media involved [136]. The actual quantity being measured is the complex reflectance ratio of medium 2 of figure A.1

$$\rho_{\text{ref}} = \mathrm{r_p}/\mathrm{r_s} \tag{A.6}$$

which is usually written in terms of two parameters ψ and Δ:

$$\rho_{\text{ref}} = \tan(\psi)\exp(\mathrm{i}\Delta) \tag{A.7}$$

where it was demonstrated that $\tan(\psi)$ and Δ represent the relative attenuation and phase shift of $\mathrm{r_p}$ with respect to $\mathrm{r_s}$ introduced by the reflection on the interface. Ideally, an optical model and an iterative fitting procedure have to be employed after the measurement in order to extract the optical properties of the studied material from ψ and Δ data set.

Spectroscopic ellipsometry measurements were done in variable angle configuration using a SENTECH SE 850 device at incident angles of 45°, 55° and 65°, for a wavelength range of 350-2100 nm.

A.1.4 In-situ reflectometry setup

With the aim of recording the evolution of specular reflectivity of rhodium films during exposure to deuterium plasma (chapter 4), an *in-situ* reflectometry setup was built around the experimental facility at the Physics Department of Basel University [117]. The equipment consists of two identical AVANTES USB spectrometers (1 and 2) with automatic dark current corrections. A white light source (Schott KL1500 Compact) is used and the light beam is split into two beams. The former is collected with spectrometer 1. The second light beam enters the experimental chamber through a glass view port, hits the sample surface and gets reflected, finally it exits from another view port and is collected by spectrometer 2. Impinging and reflected light beams describe an angle of 104°, and therefore the actual measured quantity is the specular reflectivity at 52°. In order to cope with thermomechanical instabilities of the carousel that holds the sample, the reflected beam is collected into a 2″ integrating sphere which is connected to the second spectrometer. The intensity of the deuterium plasma light is negligible in comparison to that of the reflected light. The two spectrometers are connected to a computer through a LabView programme, which records the temporal evolution of the light collected by them. The spectrum acquired by spectrometer 1 is the reference signal, whereas the spectrum collected by the spectrometer 2 is the sampling signal. The reference signal allows the reflected sampling signal to be corrected for changes in the intensity of the light source that may occur during deuterium plasma exposure, which typically takes several hours. The sampling measurement is therefore divided by the reference measurement for each time slice, giving the corrected measurement. The *in-situ* reflectometry system was not absolutely calibrated and is thus used to measure the evolution of the specular reflectivity spectrum relative to the first time slice. The quantity $\tilde{R}(\lambda,t)=I(\lambda,t)/I(\lambda,0)$ is measured. $I(\lambda,t)$ is the intensity of the reflected light beam at time t and wavelength λ measured by the spectrometer sampling the reflected beam. $I(\lambda,0)$ refers to the first time slice, which is actually an average on a number of time slices taken prior plasma switch on, in order to reduce the statistical uncertainty induced by photon noise.

A.2 Scanning electron microscopy

In Scanning Electron Microscopy (SEM), a source of electrons is focused in vacuum into a fine probe that is rastered over the surface of the specimen.

As the electrons penetrate the surface, a number of interactions occur and can result in the emission of electrons or photons from the surface. The principal images acquired in the SEM are of four types: secondary electrons images, (primary) backscattered electrons images, transmission electrons images and elemental X-ray maps. Secondary and backscattered electrons are conventionally separated according to their energies. These types of radiation are generated by different mechanisms. When a high-energy primary electron interacts with an atom, it undergoes either to inelastic scattering with atomic electrons or to elastic scattering with the atomic nucleus. In an inelastic collision with an atomic electron, some amount of energy is transferred to it. If that energy exceeds the work function of the material, the atomic electron can exit the solid (and it is called secondary electron). Secondary electrons have generally energy less than 50 eV. Most of them are produced within the first few nanometers under the surface. The other electrons, generated much deeper inside the material, are subjected to additional inelastic collisions with atomic electrons, which lower their energy and trap them in the solid. Backscattered electrons are primary electrons that have been scattered elastically by atomic nuclei, albeit these collisions may occur after the primary electrons have already lost some of their energies by inelastic scattering. The probability of elastic scattering increases strongly with the atomic number Z, approximately as Z^2, and decreases as the impinged electron energy increases, approximately as E^{-2}. Therefore, the higher the atomic number of a material, the more likely backscattering will occur. An additional electron interaction in the SEM takes place when a primary electron collides inelastically with an atom which ejects a core electron. The atom is thus excited and will decay to its ground state emitting either a characteristic X-ray photon or an Auger electron. The X-ray emission signal can be sorted by energy in an Energy Dispersive X-ray Spectrometer (EDXS) or by wavelength with a Wavelength Dispersive X-ray Spectrometer (WDXS). These distributions well characterize the elements they belong to and these signals can be used to produce elemental images that show the spatial distribution of particular elements in the field of view. The primary electrons can travel considerable distances before losing enough energy through collisions to be no longer able to determine X-ray emission. This means that a large volume of the sample will produce X-ray radiation for any position of the small primary beam (1 nm diameter), and consequently the spatial resolution is about 0.5 μm. The energies used are those relative to the K, L and M electron shells.

A.2.1 Zeiss Supra 40 field emission SEM

The SEM used during this work was a high resolution Field Emission-SEM (FE-SEM) Zeiss Supra 40 based on Gemini column, equipped with an Oxford EDXS. The photograph of the apparatus and the scheme of the column with all the detectors are shown in figures A.3a and b, respectively. The main features of the instrument are: the electron column containing

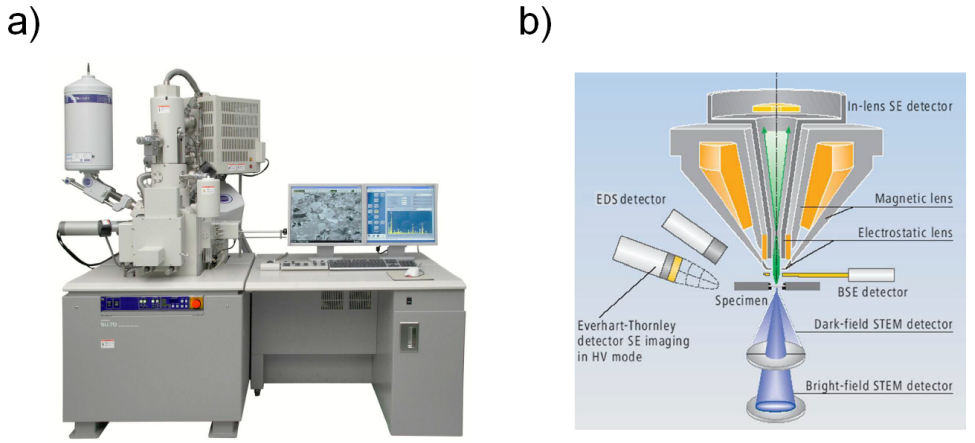

Figure A.3: *Overview of the SEM and EDXS apparatus (a). Detailed scheme of the components inside the SEM column (b).*

the electron source (i.e. the gun), the magnetic and electrostatic focusing lenses, the sample vacuum chamber at the bottom of the column and the electronics console. The Gemini column utilizes the Schottky thermal field emission source, that is a ZrO/W<100> filament operating at 1800 K. The acceleration voltage is in the range 0.1-30 kV, the specified resolution is 1.3 nm at 15 kV and the specimen stage is connected to five motors (x, y, z, tilt, rotation). The detectors present in the chamber are five. The former four provide different kind of sample imaging, while the last one acquires spectra of the X-ray radiation emitted after inelastic collisions of electrons. In particular:

- BackScattered Electrons (BSE) detector for primary electrons: to enhance compositional contrast and crystal orientation (in the considered case it is an Angle Selective Backscattered, ASB, detector); it is placed at the bottom of the gun;

- In-lens detector for secondary electrons: electrons emerged from the sample surface are attracted and accelerated by the positively biased electrode of the beam booster; it produces high resolution morphological images and it is placed in the gun;
- Everhart-Thornley chamber detector for secondary electrons: it collects remaining electrons that are not captured by the beam booster (especially at large working distances) or second generation secondary electrons; it typically depicts compositionally enhanced contrast combined with some surface information and it is placed in the chamber;
- Scanning Transmission Electron Microscopy (STEM) detection system: it comprises two parallel diode detector surfaces (Bright Field, BF, and Dark Field, DF); it provides High-Resolution (HR) information concerning the elementary constituents of the sample;
- EDXS detector: it is a silicon lithium, Si(Li), detector protected by a beryllium window; it can work in two modes: "PointID" mode provides measurements on points chosen by the user on a given sample area; "Analyzer" mode allows the user to select an area on a sample, of any size, and to record the mean X-ray signal given by an excitation scan over the selected area; Its energy resolution is on the order of 10 eV.

In this Ph.D thesis only the In-lens and Everhart-Thornley chamber detectors were exploited for morphological and thickness studies.

A.3 Atomic force microscopy

Atomic Force Microscopy (AFM) is a scanning probe technique which allows to characterize the surface of the specimen at the nanoscale. This technique integrates the information about the morphology of the sample acquired by SEM analysis. In particular, AFM owns a fine resolution along the vertical axis (i.e. perpendicular to the surface of the specimen) not achievable by SEM. For this reason, a quantitative evaluation of the surface roughness of the sample can be obtained from AFM images.

The AFM consists of a cantilever with a sharp tip (probe) at its end that is used to scan the specimen surface. The cantilever is typically silicon or silicon nitride with a tip radius of curvature on the order of nanometers. When the tip is brought into the proximity of the surface of the specimen, forces between the tip and the sample lead to a deflection of the cantilever

according to the Hooke's law [137]. Typically, the deflection is measured using a laser beam reflected from the top surface of the cantilever into an array of photodiodes. The sample is mounted onto a suitable holder whose movements are controlled by a piezoelectric scanner with sub-nanometric accuracy. The scheme of the AFM technique is shown in figure A.4a.

The AFM can be performed in a number of modes, depending on the application. In general, possible AFM imaging modes are divided into static (also called contact) modes and a variety of dynamic (non-contact or "tapping") modes. In static modes, the cantilever is "dragged" across the surface of the sample and the contours of the surface are measured directly through the deflection of the cantilever. In dynamic modes, the cantilever is externally oscillated at or close to its fundamental resonance frequency or a harmonic. The oscillation amplitude, phase and resonance frequency are modified by tip-sample interaction forces. These changes in oscillation with respect to the external reference oscillation provide information about the characteristics of the analyzed sample.

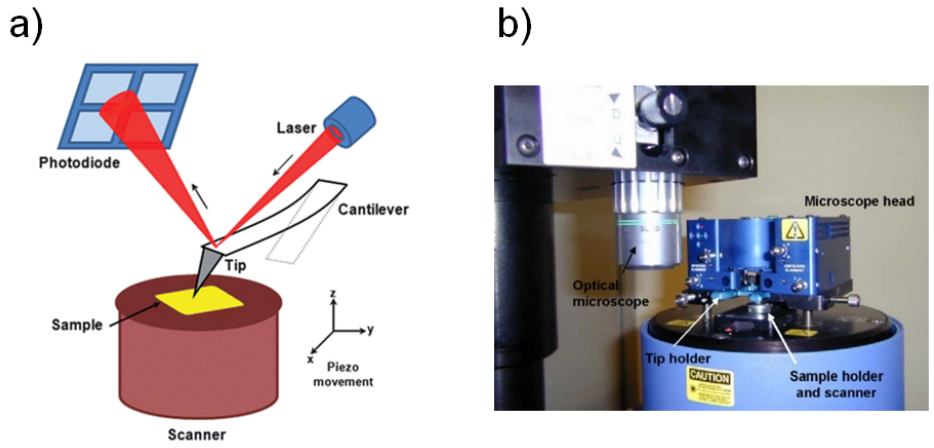

Figure A.4: *Schematic representation of the AFM (a). Photograph of the Veeco Thermomicroscope CP Research AFM (b).*

A.3.1 Veeco Thermomicroscope CP Research AFM

The Veeco Thermomicroscope CP Research AFM (figure A.4b) foresees a magnetic support to accommodate the sample onto the piezoelectric scanner. The scanner moves in the three space directions and permits to analyze surfaces with maximum and minimum dimensions of 100×100 μm^2 and hundreds of nm^2, respectively. The vertical displacements are

limited to ∼7.5 μm. An optical microscope is used to focus the semiconductor laser onto the top surface of the silicon cantilever and to select the investigated region of the sample. It is mounted onto an anti vibration support. Despite the accuracy of the scanner is on the order of a fraction of ångström, the longitudinal resolution of the AFM is limited by the tip radius of curvature of ∼10 nm. The vertical resolution reaches instead the atomic scale.

A.4 X-ray diffractometry

X-Ray Diffraction (XRD) is a powerful non-destructive technique to identify the different phases present in the analyzed specimen together with its structural properties, such as mean crystallites size, preferential growth orientations, etc. This method is based on the determination of the effects on an X-ray beam consequently to the interaction with the considered sample. It is well-known that the X-ray radiation is diffracted by the crystalline planes of the material. Constructive interference occurs if the path length difference between X-ray beams scattered from successive crystal planes is an integer of the wavelength λ of the incident radiation. This is the statement of the Bragg's law [138]:

$$n\lambda = 2d_{hkl} \sin \theta_{hkl} \tag{A.8}$$

where d_{hkl} is the distance between crystal planes with Miller indices (hkl) and θ_{hkl} is the angle described by these planes and the incident X-ray beam. The Bragg's law is represented by the sketch reported in figure A.5a. From equation A.8, it is clear that the detector of the diffracted X-rays needs to be placed at $2\theta_{hkl}$ with respect to the direction of incidence of the X-ray beam.

A.4.1 Panalytical X'Pert Pro X-ray diffractometer

The Panalytical X'Pert Pro X-ray diffractometer exploits a monochromatic copper (Cu) Kα radiation ($\lambda = 1.54$ Å). It works in Bragg-Bretano $\theta/2\theta$ configuration. In particular, the X-ray source and the detector rotate with the same velocity in opposite directions and the analyzed sample is fixed onto its holder (figure A.5b). In this way, the Bragg's law relative to the crystal planes parallel to the surface of the sample is always satisfied and the investigation of different inter-planar distances is therefore possible changing θ.

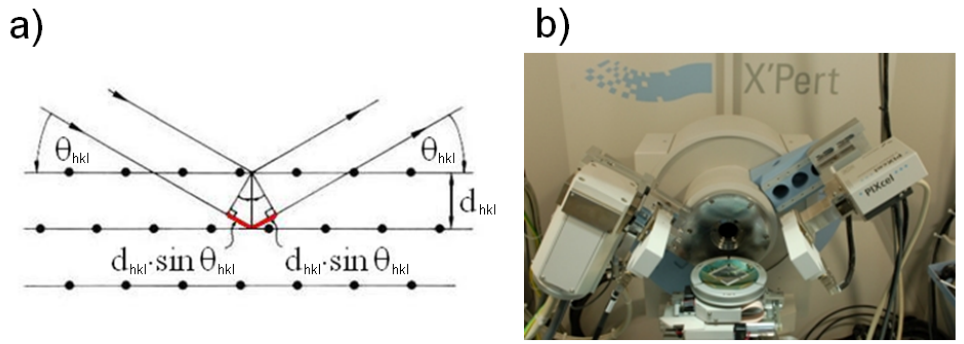

Figure A.5: *Schematic representation of the Bragg's law (a). Photograph of the Panalytical X'Pert Pro X-ray diffractometer (b).*

A.4.2 SIEMENS D5000 X-ray diffractometer

As the Panalytical X'Pert Pro X-ray diffractometer, also the SIEMENS D5000 device employs the Cu Kα radiation. However, in this case the X-ray source is placed at grazing incidence with respect to the sample surface. Within this configuration the X-ray source and the specimen are fixed while the detector moves around the latter. Grazing incidence geometry is especially exploited for thin films when it is desired to avoid the contribution from the substrate and eventually from the buffer layer deposited to improve the adhesion of the coating.

A.5 X-ray photoelectron spectroscopy

The interaction of an X-ray photon with a material sample leads to the ejection of electrons due to the well-known photoelectric effect. The measurement of the kinetic energy of the outgoing electrons is the cornerstone of X-ray Photoelectron Spectroscopy (XPS). Roughly speaking, the energy of the impinged photon hν, the kinetic energy of the photoelectron E_K and the original binging energy BE of the photoelectron are linked by the expression

$$BE = h\nu - E_K \tag{A.9}$$

Because the binding energies of the electron orbitals in atoms are known, the positions of the peaks in the acquired XPS spectrum allow to identify the chemical elements of the sample surface. Moreover, measurement of the relative areas of the photoelectron peaks permits the composition of

the sample to be determined quantitatively. Chemical bonding frequently affects the binding energy of electron orbitals giving rise to observable chemical shifts in the kinetic energy of the photoelectrons. These binding energy shifts can be used to extract information relative to the chemical nature (e.g. the atomic oxidation state) from the sample surface. For this reason, XPS is also known as Electron Spectroscopy for Chemical Analysis (ESCA).

XPS is a surface-sensitive technique. The emission of photoelectrons as a function of the depth from the sample surface, d, is predicted by the Beer-Lambert's equation [139]

$$I_d = I_\infty \left[1 - e^{-d/(IMFP \sin\theta)}\right] \tag{A.10}$$

where I_d and I_∞ are the intensities of photoelectron emission from a layer of thickness d at the surface and from an infinitely thick layer, respectively. IMFP is the Inelastic Mean Free Path (i.e. the mean distance travelled by an electron without energy loss) and θ is the take-off angle relative to the sample surface. Form equation A.10 it follows that 63% of the total XPS signal originates in the outer 1IMFP of the specimen, and 95% from within 3IMFP. While naturally no absolute cut-off can be given, it is reasonable to consider that most of the photoelectrons are emitted from within a layer thickness of 3IMFP. This is considered as the information depth of the XPS method and it is generally quoted as being in the range of 2-5 nm [139].

A.5.1 In-situ X-ray photoelectron spectroscopy measurements

The experimental facility at the Physics Department of Basel University (see also section 4.1) foresees an ultrahigh-vacuum chamber housing a photoelectron spectrometer for *in-situ* XPS (and also Ultraviolet Photoelectron Spectroscopy, UPS) measurements, linked without breaking the vacuum to the high-vacuum chamber for deuterium plasma exposure. The electron spectrometer is equipped with a hemispherical analyzer (Leybold EA10/100 MCD) and a magnesium (Mg) Kα X-ray source is used (hν = 1253.6 eV) for core level spectroscopy. The typical resolution for the XPS measurements is 0.8 eV at 30 eV pass energy. The binding energy scale is calibrated using the Au $4f_{7/2}$ line of a clean gold sample at 84.0 eV.

B

Pulsed Laser Deposition - PLD

In this appendix a general overview of the Pulsed Laser Deposition (PLD), technique widely used in the frame of this Ph.D thesis, will be given.

In PLD a target of the material to be deposited is placed in a vacuum chamber and is exposed to energetic laser pulses. After the interaction with a laser pulse, the surface of the target firstly melts and then ablates. The vaporized particles (molecules, atoms, ions, electrons and small aggregates) expand in the vacuum chamber, assuming the classical shape called "plume", towards a substrate placed in front of the target, finally determining the growth of a film onto it. The process can occur in vacuum or in presence of an inert or reactive background gas. Films properties may be other than those of the target and they strictly depend on PLD process parameters, such as buffer gas type and pressure, substrate temperature, laser wavelength, laser fluence (i.e. the ratio between the energy per pulse and the laser spot area), laser repetition rate, chemical composition and structure of target and substrate, and target to substrate distance (d_{T-S}). The principal drawbacks of this technique are the non uniform and heterogeneous nature of the deposit on areas of some mm^2, the particulate and droplets production onto its surface and the stress relaxation issue for thick films. PLD is widely used in basic research fields because it allows to study many classes of materials (metals and dielectrics, high- and low-melting, with complex stoichiometry, etc.) changing deposition parameters within large ranges [73]. In the following the principal phenomena that occur in PLD process, namely laser-target interaction, plasma formation and expansion, and film deposition, will be

briefly described. The laser pulse penetration depth in a material is:

$$l_a = \frac{1}{\mu} \tag{B.1}$$

where μ is the material absorption coefficient which depends on the laser wavelength. The interaction between laser and target induces thermal and non-thermal processes being characterized by different time scales. In particular, non-thermal processes (such as electron and phonon excitations) occur in the first stages of interaction. The equilibrium is restored in the material through electron-electron and electron-phonon collisions. Time scale of the former phenomenon is on the order of 1-100 fs, while for the latter it is few order of magnitude longer. When a nanosecond laser is used, these processes take place during pulse duration: it is possible to describe the laser-matter interaction by means of a one temperature model and the state of the system exploiting the temperature distribution of the material. Assuming that the material is homogeneous and isotropic, the corresponding heat diffusion depth l_τ is:

$$l_\tau = 2\sqrt{D \cdot \tau_L} \tag{B.2}$$

where D is the diffusion coefficient of the material and τ_L is the pulse duration. If $l_a > l_\tau$ the heating interests the superficial layer l_a thick, while if $l_a < l_\tau$, such as in the case of metals, the laser energy is transported over the penetration depth through thermal diffusion. In general, for low laser fluences, the constituents of the material are only excited, while for values greater than a threshold (which depends on the material) plasma formation occurs. The expanding plasma can absorb an amount of laser pulse energy (phenomenon also known as plasma shielding) mainly due to inverse Bremsstrahlung. In this process a photon is absorbed by a free electron under the field of an atom or ion (in order to satisfy the momentum conservation law). Plasma ionization degree can be evaluated using Saha's equation. From melted region of the target liquid droplets of various geometrical shapes and dimensions, typically with a diameter lower than 0.5 μm or in the range 1-3 μm [107], may be ejected due to the recoil pressure of the plasma plume. Plume expansion in vacuum is almost linear (vs. time) and depends only on the velocity of the ablated particles when they escape from the target. The observed fluorescence is weak and it originates from plume inner core. The spatial distribution is strongly forward directed and does not change during plasma plume expansion (see figure B.1a).

The presence in the deposition chamber of a chemically inert gas at a given pressure affects the plume expansion and modifies important process

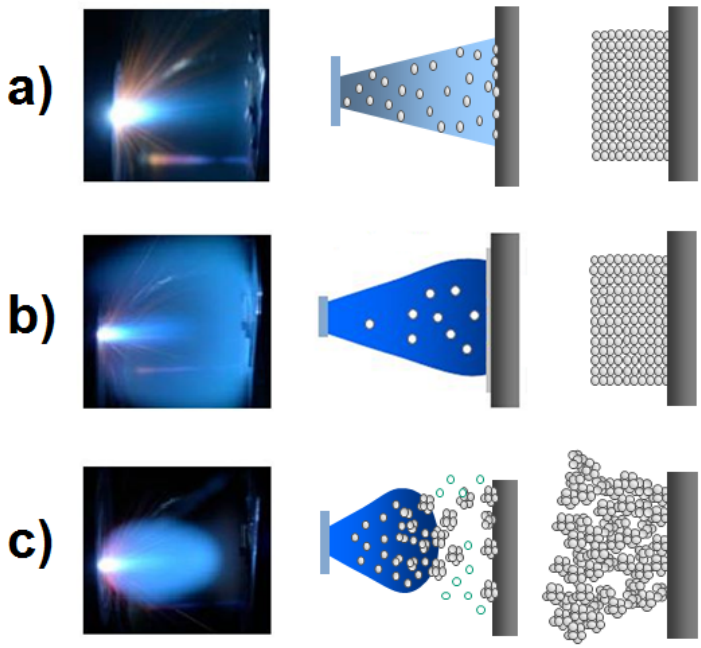

Figure B.1: *Typical ablation plumes of tungsten either in vacuum (a) or in helium at low (b) and high (c) pressure.*

features such as the spatial distribution of the ablated species, the deposition rate and the kinetic energy distribution of the depositing particles. The fraction α of energy loss in a collision between an ablated particle and a background gas atom or molecule depends on their masses m_1 and m_2, respectively:

$$\alpha = \frac{2m_1 m_2}{(m_1 + m_2)^2} \tag{B.3}$$

Chemically reactive gases, such as oxygen, nitrogen and hydrogen, are employed to deposit oxides, nitrides and hydrides starting from metallic or dielectric targets.

In general, increasing gas pressure: plume fluorescence raises due to particles collisions both in the expansion front and in the body, plume edge is better defined as a result of the presence of a shockwave front, and the plume is slowed down and spatially confined. Three distinct pressure regimes have been identified, each of which is characterized by a specific behaviour of the plume [140]:

1. a low-pressure "vacuum-like" regime with a forward directed flow and a reduced scattering of the ablated particles (figure B.1b),
2. a transition regime with strong momentum transfer to the background gas and formation of a shockwave, and
3. a regime characterized by diffusion of the ablated particles at high pressure (figure B.1c).

Depending on the collisional phenomena that occur during plasma expansion, film growth mechanisms can be sorted in two classes: atom by atom and cluster assembling. For the former, the physical models are those valid for the other deposition techniques, such as thermal evaporation and chemical vapour deposition (even if kinetic energy regimes could be different and other phenomena could take place, like implantation and sputtering). Otherwise, at sufficiently high gas pressure, collisions can lead to cluster aggregation inside the plume. In this case, film formation is determined by the kinetic energy per atom in the cluster. As a consequence, it is possible to deposit films with different morphologies, from compact to highly porous.

In addition to buffer gas nature and pressure, the most important process parameters are laser wavelength, fluence per pulse, laser spot size and substrate temperature. Short wavelength pulses deposit larger energy per unit volume in the target. High values of fluence per pulse induce high ionization degree and energy of the ablated species, but also, in general, high ejection of particulate and droplets, due to the high recoil pressure of the plasma plume and to hydrodynamic instabilities at the target surface. Increasing the spot dimension the plume has better directionality, normal to the target, and the expulsion of particulate and droplets is reduced, as a consequence of the smaller boundary effect. The angle of incidence of the laser beam to the target is generally 45°: it constitutes a good compromise between laser spot size onto the target and plasma shielding process. In this case the plume is not perfectly perpendicular to the target but it is slightly tilted towards the laser direction. Substrate temperature influences film growth mechanism, given that high temperatures can favour the diffusion of the species on the substrate. Moreover, substrate heating can lead to the formation of crystalline films, due to the re-organization of the deposited atoms in a more stable configuration. An excessive temperature can bring to the re-evaporation of the film or of the more volatile constituents: this process parameter can be thus exploited to select the deposited compounds.

C

Complements on tiles profiling at JET

With the goal of acquiring information about the overall JET divertor erosion and re-deposition pattern after the first ILW campaign of 2011-2012, the interpretative tool for tiles profiling measurements introduced in chapter 6, and specifically in section 6.3, was applied to inner divertor tiles 1, 3, 4 and to outer divertor tiles 6, 7, 8. The results relative to tiles 1 and 6 were just reported in section 6.4. In this appendix the evaluated erosion and re-deposition pattern of the remnant tiles will be presented.

Figures C.1a-C.4a show the appearance of each tile after 2011-2012 JET-ILW campaign, together with the grid employed to perform the profiling measurements. The results of the MatLab routine are reported in figures C.1b-C.4b. For each tile, it is clear that the standard deviation bars associated to the average erosion/re-deposition pattern keep within the order of the profiling system accuracy of some microns. The bi-dimensional hypothesis of the symmetry of divertor tiles erosion and re-deposition along JET toroidal direction was thus well satisfied. All the tiles examined here were measured with the stylus bent, both before and after their exposure to the JET plasma. Therefore, the average poloidal shift $\overline{\Delta x}$ was within $\sim$50 μm in every case. This very low value underlines the high re-positioning accuracy of the tile after its exposure.

Considering inner divertor tile 3, the absence of any feature in figure C.1a agrees with the evaluated erosion/re-deposition pattern of figure C.1b, which maintains on the order of the profiling system accuracy along the poloidal direction of the tile.

The photograph of inner divertor tile 4 after its exposure is shown in

figure C.2a. The left part of the tile, which coincides with the shadowed region under tile 3 (see figure 6.8), is iridescent. This feature suggests the presence of some kind of contaminant with a non-uniform thickness. Re-deposition in divertor shadowed zones was reported in the literature related to previous JET experimental campaigns with an all-C first-wall [51]. However, the estimated erosion/re-deposition pattern of figure C.2b maintains on the order of the profiler accuracy along all tile 4. The discrepancy between this result and the appearance of the left part of the tile could be explained in terms of a re-deposition background not revealed by the MatLab routine or, alteratively, by the presence of re-deposits with a thickness lower than some microns on the shadowed region of tile 4. From figure C.2a it is also visible a dark stripe where the tile starts to slope and a light blue zone on the right flat part of the tile. Albeit the average erosion/re-deposition pattern is within the profiling system accuracy for every poloidal coordinate, the standard deviation bars for these two regions extend to $\sim$10 μm. Erosion or re-deposition could thus be occurred for some toroidal coordinate.

The situation for outer divertor tile 7 is analogous to that of its counterpart in the inner divertor, tile 3. No features are detectable from the photograph C.3a of tile 7 after its exposure to JET plasma. Moreover, the evaluated erosion/re-deposition pattern C.3b maintains below the profiler accuracy along all the tile.

Also the appearance of tile 8 after the experimental campaign does not present any peculiarity (figure C.4a). Despite visual inspection, its erosion/re-deposition pattern evaluated by the MatLab code (figure C.4b) shows an erosion zone with maximum depth $\sim$12 μm in correspondence of the top of the tile and a re-deposit with a thickness up to $\sim$15 μm on its right sloped part. Cross-section microscopy measurements are therefore necessary to confirm the goodness of these results.

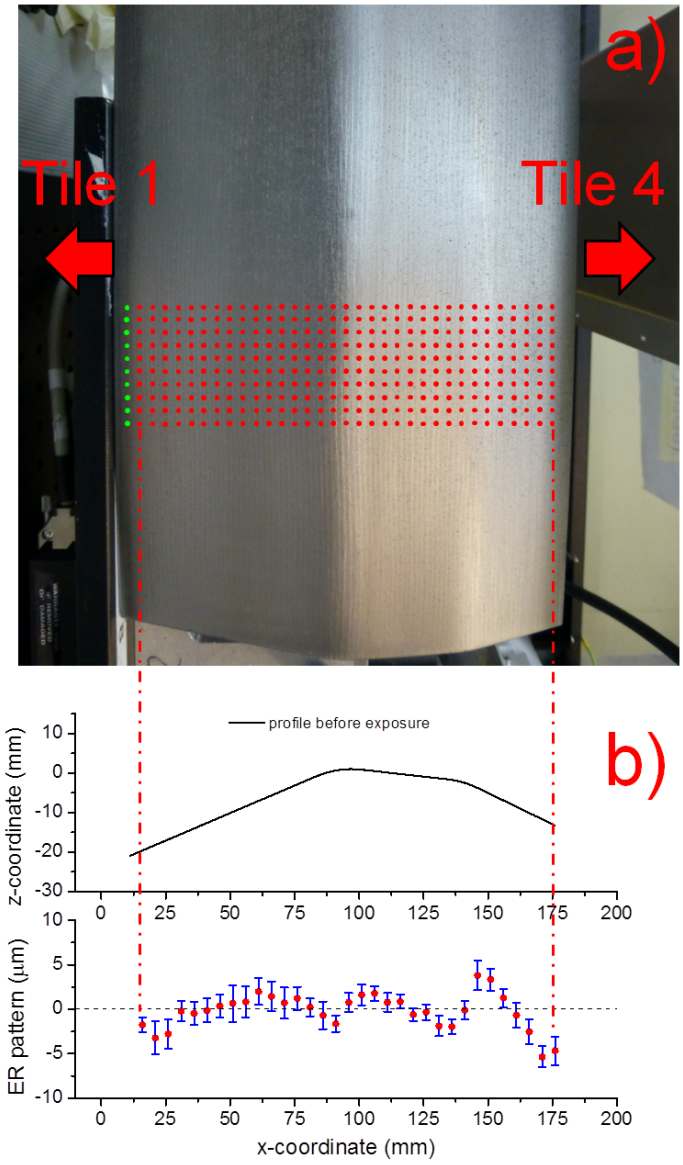

Figure C.1: *A photograph of inner divertor tile 3 after its exposure, together with the grid used for the profiling measurements (red and green dots; the latter indicate the grid points excluded by the alignment procedure) and a hint of the location of the neighbouring tiles (a). The outcome of the numerical approach (b). The average misalignment triplet is (30.8±5.2µm, -53.9±0.88µm, -0.0081°±0.0012°).*

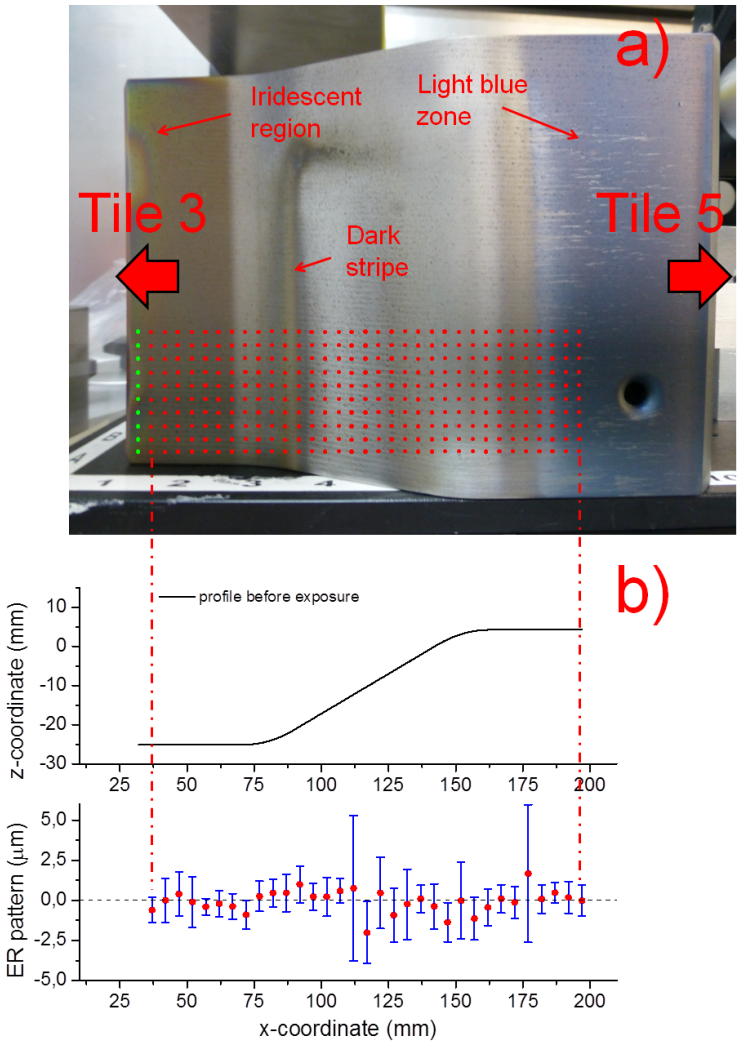

Figure C.2: *A photograph of inner divertor tile 4 after its exposure, together with the grid used for the profiling measurements (a). The outcome of the numerical approach (b). The average shift triplet is (5.3±1.7µm, -33.8±0.63µm, -0.0023°±0.0005°).*

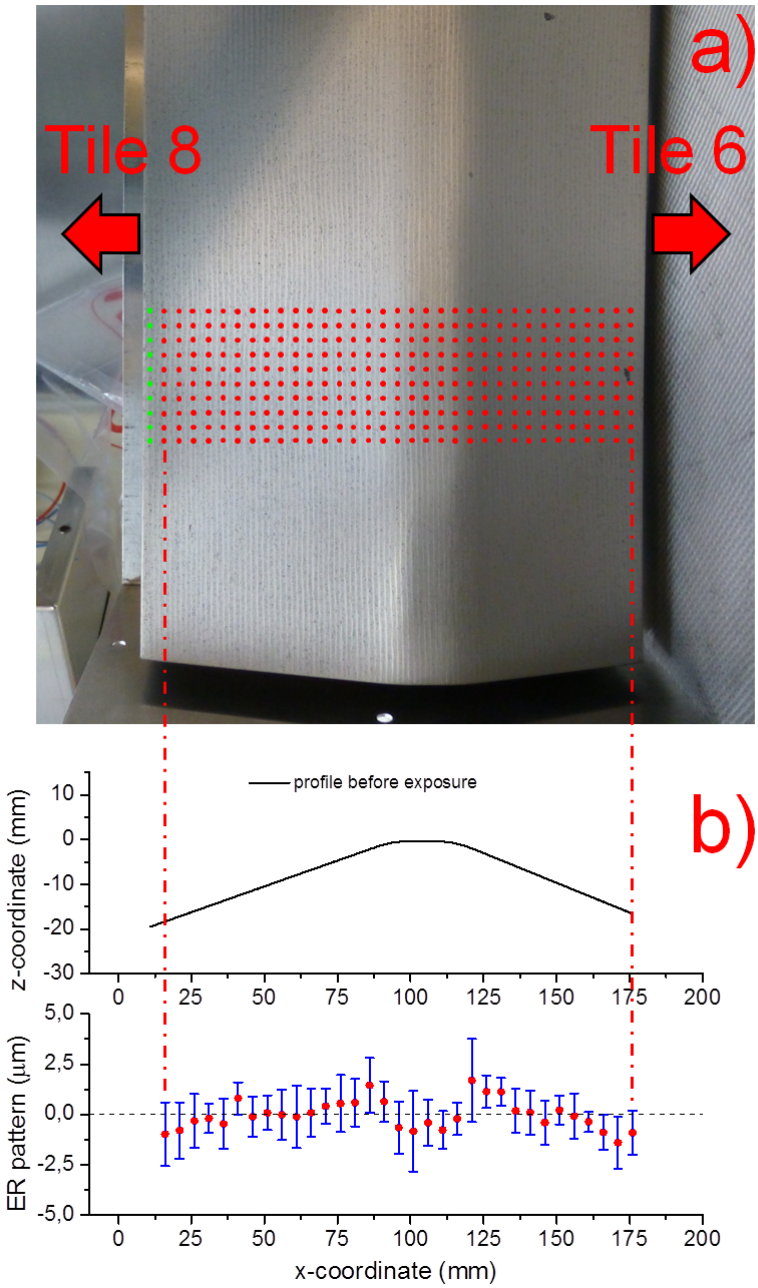

Figure C.3: *A photograph of outer divertor tile 7 after its exposure, together with the grid used for the profiling measurements (a). The outcome of the numerical approach (b). The average re-positioning error is (21.3±2.9µm, -44±0.47µm, 0.0003°±0.0008°).*

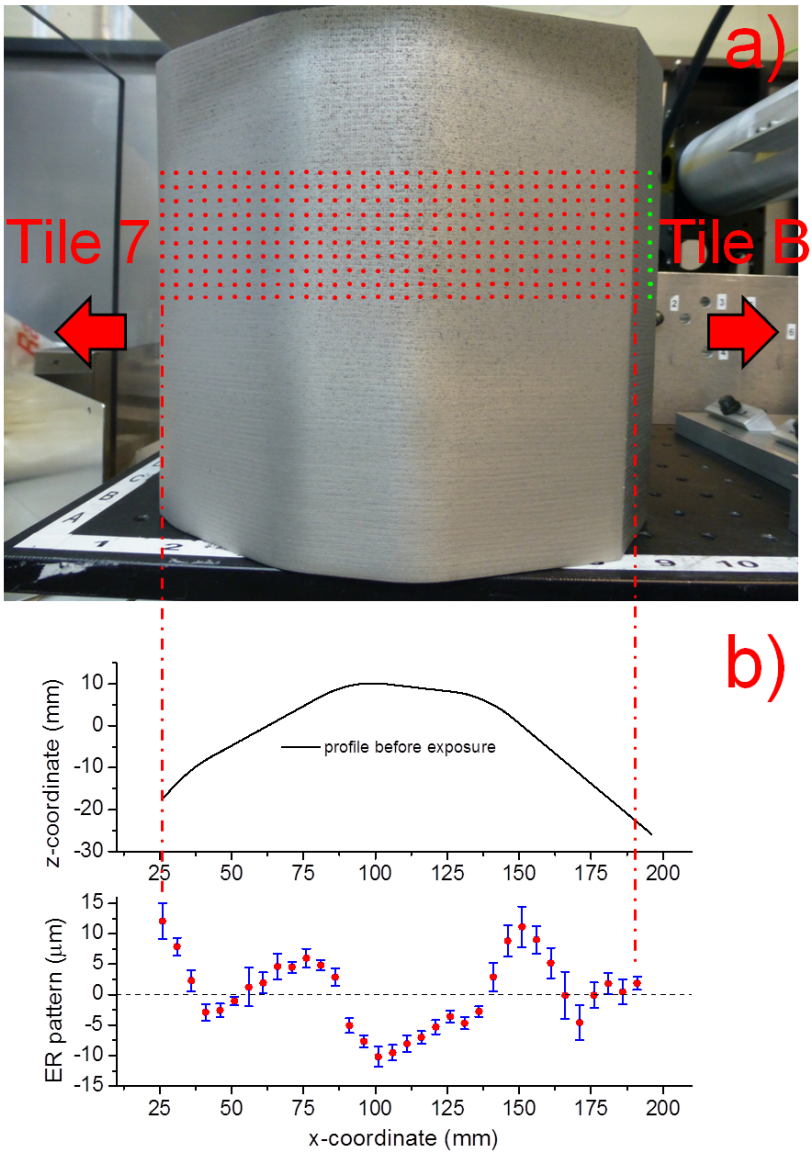

Figure C.4: *A photograph of outer divertor tile 8 after its exposure, together with the grid used for the profiling measurements (a). The outcome of the numerical approach (b). The average misalignment is (-53.8±3.8μm, -38.6±12μm, 0.0354°±0.00096°).*

Bibliography

[1] B.D. Bondarenko. Role played by O A Lavrent'ev in the formulation of the problem and the initiation of research into controlled nuclear fusion in the USSR. *Physics-Uspekhi*, 44(8):844–851, 2001.

[2] Web page of ITER: `http://www.iter.org`.

[3] T. Sugie, A. Costley, A. Litnovsky, and Participant Teams. Update of First Mirror Table. 12th Meeting of the ITPA Topical Group on Diagnostics, PPPL, Princeton, USA, 26-30 March 2007.

[4] A.E. Costley, T. Sugie, G. Vayakis, and C.I. Walker. Technological challenges of ITER diagnostics. *Fusion Engineering and Design*, 74(1-4):109–119, 2005.

[5] E.E. Mukhin, V.V. Semenov, A.G. Razdobarin, et al. First mirrors in ITER: material choice and deposition prevention/cleaning techniques. *Nuclear Fusion*, 52(1):013017–013026, 2012.

[6] E.D. Palik. *Handbook of Optical Constants of Solids*. Number v. 1. Elsevier Science, 1985.

[7] C. Lombardi. *Impianti nucleari*. Polipress, Milano, 2009.

[8] P. Stangeby. *The plasma Boundary of Magnetic Fusion Devices*. Taylor & Francis Group, New York, 2000.

[9] R.J. Hawryluk. Results from deuterium-tritium tokamak confinement experiments. *Reviews of Modern Physics*, 70(2):537–587, 1998.

[10] Michael D.W. D-T operation on TFTR. In C. VARANDAS and F. SERRA, editors, *Fusion Technology 1996*, pages 135–142. Elsevier, Oxford, 1997.

[11] A.S. Kaye. Results of recent deuterium/tritium experiments in JET. *Fusion Technology*, 34(3 pt 2):308–316, 1998.

[12] ITER Physics Basis Editors, ITER Physics Expert Group Chairs, Co-Chairs, ITER Joint Central Team, and Physics Integration Unit. Chapter 1: Overview and summary. *Nuclear Fusion*, 39(12):2137–2174, 1999.

[13] K. Tomabechi. International thermonuclear experimental reactor, ITER. *Fusion Engineering and Design*, 8(0):43–49, 1989.

[14] ITER Team and K. Tomabechi. ITER: design overview. *Journal of Nuclear Materials*, 179-181, Part 2(0):1173–1178, 1991.

[15] R. Aymar, V.A. Chuyanov, M. Huguet, et al. Overview of ITER-FEAT - The future international burning plasma experiment. *Nuclear Fusion*, 41(10):1301–1310, 2001.

[16] ITER Technical Basis, ITER EDA Documentation Series No 24, IAEA, Vienna 2002.

[17] J. Winter. Wall conditioning in fusion devices and its influence on plasma performance. *Plasma Physics and Controlled Fusion*, 38:1503–1542, 1996.

[18] T. Burchell. Radiation Damage in Carbon-Carbon Composites: Structure and Property Effects. *Physica Scripta*, T64:17–25, 1996.

[19] M. Walsh, P. Andrew, R. Barnsley, et al. ITER DIAGNOSTIC CHALLENGES. *2011 IEEE/NPSS 24th Symposium on Fusion Engineering*, pages 1–8, 2011.

[20] V.S. Udintsev. Measurements of temperature and density in magnetic confinement fusion devices. *Nuclear Instruments and Methods in Physics Research Section A: Accelerators, Spectrometers, Detectors and Associated Equipment*, 623(2):649–652, 2010.

[21] A. Encheva, L. Bertalot, B. Macklin, G. Vayakis, and C. Walker. Integration of ITER in-vessel diagnostic components in the vacuum vessel. *Fusion Engineering and Design*, 84(2-6):736–742, 2009.

[22] M.J. Walsh, M. Beurskens, P.G. Carolan, et al. Design challenges and analysis of the ITER core LIDAR Thomson scattering system. *Review of Scientific Instruments*, 77(10):10E525–10E528, 2006.

[23] V.S. Udintsev, G. Vayakis, A.E. Costley, et al. Progress in the development of the ITER ECE diagnostic. *Fusion Science and Technology*, 59(4):678–683, 2011.

[24] F. Le Guern, S. Ciattaglia, G. Counsell, et al. R&D on in-vessel dust and tritium management in ITER. In *Fusion Engineering (SOFE), 2011 IEEE/NPSS 24th Symposium on*, pages 1–5, 2011.

[25] M. Sasao, L. Bertalot, M. Ishikawa, and S. Popovichev. Strategy for the absolute neutron emission measurement on ITER. *Review of Scientific Instruments*, 81(10):10D329–10D331, 2010.

[26] M.H. Aumeunier, M. Firdaouss, J.-M. Travère, et al. Modeling of the ITER-like wide-angle infrared thermography view of JET. *Review of Scientific Instruments*, 83(10):10D522–10D524, 2012.

[27] G.F. Matthews. Plasma operation with an all metal first-wall: Comparison of an ITER-like wall with a carbon wall in JET. *Journal of Nuclear Materials*, 438, Supplement(0):S2–S10, 2013.

[28] G.A. Naylor, R. Scannell, M. Beurskens, et al. The ITER Thomson scattering core LIDAR diagnostic. *Journal of Instrumentation*, 7(03):C03043–C03052, 2012.

[29] ITER Physics Expert Group on Diagnostics and ITER Physics Basis Editors. Chapter 7: Measurement of plasma parameters. *Nuclear Fusion*, 39(12):2541–2575, 1999.

[30] M.N.A. Beurskens, L. Giudicotti, M. Kempenaars, R. Scannell, and M.J. Walsh. ITER LIDAR performance analysis. *Review of Scientific Instruments*, 79(10):10E727–10E731, 2008.

[31] I. Pastor, J. Guasp, R.F. Álvarez Estrada, and F. Castejón. Monte Carlo approach to Thomson scattering in relativistic fusion plasmas with allowance for ultraintense laser radiation. *Nuclear Fusion*, 51(4):043011–043027, 2011.

[32] R. Scannell, M.J. Walsh, P.G. Carolan, et al. Design of a new Nd:YAG Thomson scattering system for MAST. *Review of Scientific Instruments*, 79(10):10E730–10E733, 2008.

[33] K. Ebisawa, A.E. Costley, A.J.H. Donne, et al. Plasma diagnostics for ITER-FEAT. *Review of Scientific Instruments*, 72(1):545–550, 2001.

[34] T. Kakuta, T. Shikama, T. Nishitani, et al. Round-robin irradiation test of radiation resistant optical fibers for ITER diagnostic application. *Journal of Nuclear Materials*, 307-311, Part 2(0):1277–1281, 2002.

[35] M. Decreton, T. Shikama, and E. Hodgson. Performance of functional materials and components in a fusion reactor: the issue of radiation effects in ceramics and glass materials for diagnostics. *Journal of Nuclear Materials*, 329-333, Part A(0):125–132, 2004.

[36] S. Sheludyakov, G. Shatalov, and K. Vukolov. Calculations of neutron and gamma transport in ITER H-alpha and CXRS diagnostic channels. *Plasma Devices and Operations*, 13(2):111–122, 2005.

[37] A. Litnovsky, V.S. Voitsenya, A. Costley, A.J.H. Donné, and for the SWG on First Mirrors of the ITPA Topical Group on Diagnostics. First mirrors for diagnostic systems of ITER. *Nuclear Fusion*, 47(8):833–838, 2007.

[38] R.E.H. Clark and D. Reiter. *Nuclear Fusion Research: Understanding Plasma-Surface Interactions*. Springer Series in Chemical Physics. Springer, 2006.

[39] G.F. Matthews. Material migration in divertor tokamaks. *Journal of Nuclear Materials*, 337-339(0):1–9, 2005.

[40] Y. Yamamura and J. Bohdansky. Few collisions approach for threshold sputtering. *Vacuum*, 35(12):561–571, 1985.

[41] M. Küstner, W. Eckstein, V. Dose, and J. Roth. The influence of surface roughness on the angular dependence of the sputter yield. *Nuclear Instruments and Methods in Physics Research Section B: Beam Interactions with Materials and Atoms*, 145(3):320–331, 1998.

[42] M. Balden, A.F. Bardamid, A.I. Belyaeva, et al. Surface roughening and grain orientation dependence of the erosion of polycrystalline stainless steel by hydrogen irradiation. *Journal of Nuclear Materials*, 329-333, Part B(0):1515–1519, 2004.

[43] M. Mayer, R. Behrisch, P. Andrew, and A.T. Peacock. Erosion at the vessel walls of JET. *Journal of Nuclear Materials*, 241-243(0):469–475, 1997.

[44] H. Verbeek, J. Stober, D.P. Coster, W. Eckstein, and R. Schneider. Interaction of charge exchange neutrals with the main chamber walls of plasma machines. *Nuclear Fusion*, 38(12):1789–1803, 1998.

[45] R. Behrisch, G. Federici, A. Kukushkin, and D. Reiter. Material erosion at the vessel walls of future fusion devices. *Journal of Nuclear Materials*, 313-316(0):388–392, 2003.

[46] J. Roth. Chemical erosion of carbon based materials in fusion devices. *Journal of Nuclear Materials*, 266-269(0):51–57, 1999.

[47] D. Naujoks, J. Roth, K. Krieger, G. Lieder, and M. Laux. Erosion and redeposition in the ASDEX Upgrade divertor. *Journal of Nuclear Materials*, 210(1-2):43–50, 1994.

[48] G. Federici, C.H. Skinner, J.N. Brooks, et al. Plasma-material interactions in current tokamaks and their implications for next step fusion reactors. *Nuclear Fusion*, 41(12):1967–2137, 2001.

[49] A. Widdowson, S. Brezinsek, J.P. Coad, et al. An overview of erosion-deposition studies for the JET Mk II high delta divertor. *Physica Scripta*, 2009(T138):014005–014012, 2009.

[50] R.A. Pitts, J.P. Coad, D.P. Coster, et al. Material erosion and migration in tokamaks. *Plasma Physics and Controlled Fusion*, 47(12B):B303–B322, 2005.

[51] J.P. Coad, N. Bekris, J.D. Elder, et al. Erosion/deposition issues at JET. *Journal of Nuclear Materials*, 290-293(0):224–230, 2001.

[52] H.E. Bennett and J.O. Porteus. Relation Between Surface Roughness and Specular Reflectance at Normal Incidence. *Journal of the Optical Society of America*, 51(2):123–129, 1961.

[53] V. Voitsenya, A.E. Costley, V. Bandourko, et al. Diagnostic first mirrors for burning plasma experiments (invited). *Review of Scientific Instruments*, 72(1 II):475–482, 2001.

[54] G. De Temmerman, R.A. Pitts, V.S. Voitsenya, et al. First mirror tests for ITER: Influence of material choice on the erosion/deposition mechanisms affecting optical reflectivity. *Journal of Nuclear Materials*, 363-365(0):259–263, 2007.

[55] A.J.H. Donné, R. Boivin, A.E. Costley, et al. Physics R&D in Support of ITER/BPX Diagnostic Development. 19th IAEA Fusion Energy Conference, CT/P-10, 2002.

[56] A. Litnovsky, G. De Temmerman, K. Vukolov, et al. Investigations of single crystal and polycrystalline metal mirrors under erosion conditions in TEXTOR. *Fusion Engineering and Design*, 82(2):123–132, 2007.

[57] A. Litnovsky, P. Wienhold, V. Philipps, et al. Diagnostic mirrors for ITER: A material choice and the impact of erosion and deposition on their performance. *Journal of Nuclear Materials*, 363-365(0):1395–1402, 2007.

[58] V.S. Voitsenya, A.F. Bardamid, A.I. Belyaeva, et al. Interpretation of tore supra in-vessel mirror experiments. *Plasma Devices and Operations*, 16(1):1–10, 2008.

[59] M. Rubel, G.D. Temmerman, P. Sundelin, et al. An overview of a comprehensive First Mirror Test for ITER at JET. *Journal of Nuclear Materials*, 390-391(1):1066–1069, 2009.

[60] M. Rubel, J.P. Coad, G. De Temmerman, et al. First Mirrors Test in JET for ITER: An overview of optical performance and surface morphology. *Nuclear Instruments and Methods in Physics Research, Section A: Accelerators, Spectrometers, Detectors and Associated Equipment*, 623(2):818–822, 2010.

[61] M. Rubel, D. Ivanova, J.P. Coad, et al. Overview of the second stage in the comprehensive mirrors test in JET. *Physica Scripta*, 2011(T145):014070–014075, 2011.

[62] L. Marot, E. Meyer, M. Rubel, et al. Performances of Rh and Mo mirrors under JET exposure. *Journal of Nuclear Materials*, 438(SUPPL):S1187–S1191, 2013.

[63] A. Litnovsky, M. Matveeva, A. Herrmann, et al. First studies of ITER-diagnostic mirrors in a tokamak with an all-metal interior: results of the first mirror test in ASDEX Upgrade. *Nuclear Fusion*, 53(7):073033–073039, 2013.

[64] B. Eren, M. Wisse, L. Marot, R. Steiner, and E. Meyer. Deuterium plasma exposure on rhodium: Reflectivity monitoring and evidence of subsurface deuteride formation. *Applied Surface Science*, 273(0):94–100, 2013.

[65] A. Litnovsky, V. Voitsenya, T. Sugie, et al. Progress in research and development of mirrors for ITER diagnostics. *Nuclear Fusion*, 49(7):075014–075021, 2009.

[66] D. Orlinski, A.F. Bardamid, V. Konovalov, et al. Rhodium as the promising material for the first mirrors of laser and spectroscopy methods of plasma diagnostics in a fusion reactor. *Problems of Atomic Science and Tecnology, Series Plasma Physics (5)*, (3):67–69, 2000.

[67] F.P. Orsitto, D. Del Bugaro, M. DiFino, et al. Optical characterization of plasma facing mirrors for a Thomson scattering system of a burning plasma experiment. *Review of Scientific Instruments*, 72(1 II):540–544, 2001.

[68] G. Maddaluno, M. Di Fino, F. Orsitto, et al. Tests of rhodium - coated molybdenum first mirrors for ITER diagnostics. *34th EPS Conference on Plasma Physics 2007, EPS 2007 - Europhysics Conference Abstracts*, 31(1):379–382, 2007.

[69] B. Eren, L. Marot, A. Litnovsky, et al. Reflective metallic coatings for first mirrors on ITER. *Fusion Engineering and Design*, 86(9-11):2593–2596, 2011.

[70] L. Marot, G. De Temmerman, P. Oelhafen, G. Covarel, and A. Litnovsky. Rhodium coated mirrors deposited by magnetron sputtering for fusion applications. *Review of Scientific Instruments*, 78(10):103507–103513, 2007.

[71] L. Marot, G. De Temmerman, V. Thommen, D. Mathys, and P. Oelhafen. Characterization of magnetron sputtered rhodium films for reflective coatings. *Surface and Coatings Technology*, 202(13):2837–2843, 2008.

[72] M. Passoni, D. Dellasega, G. Grosso, et al. Nanostructured rhodium films produced by pulsed laser deposition for nuclear fusion applications. *Journal of Nuclear Materials*, 404(1):1–5, 2010.

[73] D.B. Chrisey and G.K. Hubler. *Pulsed laser deposition of thin films*, volume 1. Wiley-VCH, 2003.

[74] D. Dellasega, A. Facibeni, F. Di Fonzo, et al. Nanostructured high valence silver oxide produced by pulsed laser deposition. *Applied Surface Science*, 255(10):5248–5251, 2009.

[75] P. Gondoni, M. Ghidelli, F. Di Fonzo, et al. Structural and functional properties of Al:ZnO thin films grown by Pulsed Laser Deposition at room temperature. *Thin Solid Films*, 520(14):4707–4711, 2012.

[76] H. Bergsåker, P. Petersson, I. Bykov, et al. Microanalysis of deposited layers in the divertor of JET following operations with carbon wall. *Journal of Nuclear Materials*, 438, Supplement(0):S668–S672, 2013.

[77] J. Von Seggern, M. Rubel, P. Karduck, et al. Properties of thick layers deposited on plasma facing wall components of TEXTOR-94. volume 81, pages 31–34, 1999.

[78] R. Reichle, D. Guilhem, R. Mitteau, et al. Status of power balance monitoring for long pulse operation at Tore Supra. *Nuclear Fusion*, 43(9):797–804, 2003.

[79] P. Ramanlal and L.M. Sander. Theory of Ballistic Aggregation. *Physical Review Letters*, 54:1828–1831, 1985.

[80] M. Mayer, M. Andrzejczuk, R. Dux, et al. Tungsten erosion and redeposition in the all-tungsten divertor of ASDEX Upgrade. *Physica Scripta*, 2009(T138):014039–014045, 2009.

[81] J.P Sharpe, D.A Petti, and H.-W Bartels. A review of dust in fusion devices: Implications for safety and operational performance. *Fusion Engineering and Design*, 63-64(0):153–163, 2002.

[82] A. Bouchoule. *Dusty plasmas: physics, chemistry, and technological impacts in plasma processing*. Wiley, 1999.

[83] S.I. Krasheninnikov, R.D. Smirnov, and D.L. Rudakov. Dust in magnetic fusion devices. *Plasma Physics and Controlled Fusion*, 53(8):083001–083054, 2011.

[84] E. Mukhin, K. Vukolov, V. Semenov, et al. Progress in the development of deposition prevention and cleaning techniques of in-vessel optics in ITER. *Nuclear Fusion*, 49(8):085032–085040, 2009.

[85] E. Gubbini, G. Kommol, M. Schnürer, et al. "On-line" cleaning of optical components in a multi-TW-Ti:Sa laser system. *Vacuum*, 76(1):45–49, 2004.

[86] A. Widdowson, J.P. Coad, G. De Temmerman, et al. Removal of beryllium-containing films deposited in JET from mirror surfaces by laser cleaning. *Journal of Nuclear Materials*, 415(1, Supplement):S1199–S1202, 2011.

[87] Y. Zhou, L. Zheng, Y.G. Li, et al. Development of carbon deposits cleaning technique for metallic mirrors in HL-2A. *Journal of Nuclear Materials*, 415(1, Supplement):S1206–S1209, 2011.

[88] A. Leontyev, A. Semerok, D. Farcage, et al. Theoretical and experimental studies on molybdenum and stainless steel mirrors cleaning by high repetition rate laser beam. *Fusion Engineering and Design*, 86(9-11):1728–1731, 2011.

[89] M. Wisse, L. Marot, B. Eren, et al. Laser damage thresholds of ITER mirror materials and first results on in situ laser cleaning of stainless steel mirrors. *Fusion Engineering and Design*, 88(5):388–399, 2013.

[90] S. Siano, J. Agresti, I. Cacciari, et al. Laser cleaning in conservation of stone, metal, and painted artifacts: state of the art and new insights on the use of the Nd:YAG lasers. *Applied Physics A*, 106(2):419–446, 2012.

[91] D. Kane. *Laser Cleaning 2*. World Scientific, 2006.

[92] A. Kumar, J.P. Nilaya, D.J. Biswas, et al. CO_2 laser assisted removal of UO_2 and ThO_2 particulates from metal surface. *Applied Surface Science*, 257(16):7263–7267, 2011.

[93] F. Le Guern, C. Hubert, S. Mousset, et al. Laser ablation tests performed on TORE-SUPRA graphite samples. *Journal of Nuclear Materials*, 335(3):410–416, 2004.

[94] C.H. Skinner, C.A. Gentile, A. Carpe, et al. Tritium removal from codeposits on carbon tiles by a scanning laser. *Journal of Nuclear Materials*, 301(2-3):98–107, 2002.

[95] H. Roche, C. Grisolia, C. Hernandez, et al. Measurement methods associated to laser ablation technique in layer removal process on Plasma Facing Components. In *Advancements in Nuclear Instrumentation Measurement Methods and their Applications (ANIMMA), 2009 First International Conference on*, pages 1–5, 2009.

[96] H. Roche, C. Grisolia, C. Hernandez, et al. Deposited layer removal by laser ablation: from laboratory to Tore Supra integration. *Physica Scripta*, 2009(T138):014028–014031, 2009.

[97] C. Hernandez, H. Roche, C. Pocheau, et al. Development of a Laser Ablation System Kit (LASK) for Tokamak in vessel tritium and dust inventory control. *Fusion Engineering and Design*, 84(2-6):939–942, 2009.

[98] C. Hernandez, H. Roche, C. Pocheau, et al. Integration of Laser Techniques in a Remote-Handled System for Tokamak Using and Dust Management. *Plasma Science, IEEE Transactions on*, 38(3):237–241, 2010.

[99] A. Vatry, M. Naiim Habib, Ph. Delaporte, et al. Experimental investigation on laser removal of carbon and tungsten particles. *Applied Surface Science*, 255(10):5569–5573, 2009.

[100] A. Vatry, M. Naiim Habib, Ph. Delaporte, et al. Characterization of carbon and tungsten micro-particles mobilized by laser irradiation in order to develop an ITER dust removal technique. *Journal of Nuclear Materials*, 390-391(0):144–147, 2009.

[101] A. Vatry, A. Marchand, Ph. Delaporte, et al. Studies of laser-induced removal mechanisms for tokamak-like particles. *Applied Surface Science*, 257(12):5384–5388, 2011.

[102] A. Vatry, A. Marchand, Ph. Delaporte, et al. Tokamak-like dust removal induced by laser irradiation. *Journal of Nuclear Materials*, 415(1, Supplement):S1115–S1118, 2011.

[103] A. Vatry, C. Grisolia, Ph. Delaporte, and M. Sentis. Removal of in vessel Tokamak dust by laser techniques. *Fusion Engineering and Design*, 86(9-11):2717–2721, 2011.

[104] Y. Zhou, L. Zheng, H. Gao, et al. Cleaning of the first mirrors and diagnostic windows by YAG laser on HL-2A. *Physica Scripta*, 2009(T138):014066–014069, 2009.

[105] A. Alfier, S. Barison, A. Fassina, et al. Impurities removal by laser blow-off from in-vacuum optical surfaces on RFX-mod experiment. *Review of Scientific Instruments*, 81(12):123509–123518, 2010.

[106] A. Alfier, R. Pasqualotto, L. Giudicotti, V. Cervaro, and L. Franchin. Optimized in-situ window cleaning system by laser blow-off through

optical fiber. *Journal of Physics: Conference Series*, 227(1):012036–012039, 2010.

[107] R. Eason. *Pulsed Laser Deposition of Thin Films: Applications-Led Growth of Functional Materials*. Wiley, 2007.

[108] A.L. Patterson. The scherrer formula for x-ray particle size determination. *Physical Review*, 56(10):978–982, 1939.

[109] A.S. Kuzanyan, V.A. Petrosyan, S.Kh. Pilosyan, and V.M. Nesterov. Laser deposition of large-area thin films. *Quantum Electronics*, 41(3):253–256, 2011.

[110] L. Cultrera, M.I. Zeifman, and A. Perrone. Strong emission of particulates towards the incident beam direction in pulsed-laser ablation experiments. *Applied Surface Science*, 253(15):6322–6325, 2007.

[111] A. Lorusso, V. Fasano, A. Perrone, and K. Lovchinov. Y thin films grown by pulsed laser ablation. *Journal of Vacuum Science Technology A: Vacuum, Surfaces, and Films*, 29(3):031502–031506, 2011.

[112] W.O. Siew, S.S. Yapl, T.K. Yong, C.H. Nee, and T.Y. Tou. Effects of phase explosion in pulsed laser deposition of nickel thin film and submicron droplets. *Applied Surface Science*, 257(7):2775–2778, 2011.

[113] L. Marot, G. Covarel, M.-H. Tuilier, R. Steiner, and P. Oelhafen. Adhesion of rhodium films on metallic substrates. *Thin Solid Films*, 516(21):7604–7608, 2008.

[114] M. Joanny, J.-M. Travère, S. Salasca, et al. Engineering and manufacturing of ITER first mirror mock-ups[a)]. *Review of Scientific Instruments*, 81(10):10E108–10E110, 2010.

[115] M. Joanny, J.-M. Travère, S. Salasca, et al. Achievements on engineering and manufacturing of ITER first-mirror mock-ups. *IEEE Transactions on Plasma Science*, 40(3 PART 1):692–696, 2012.

[116] B. Eren, L. Marot, M. Langer, et al. The effect of low temperature deuterium plasma on molybdenum reflectivity. *Nuclear Fusion*, 51(10):103025–103034, 2011.

[117] M. Wisse, B. Eren, L. Marot, R. Steiner, and E. Meyer. Spectroscopic reflectometry of mirror surfaces during plasma exposure. *Review of Scientific Instruments*, 83(1):013509–13514, 2012.

[118] B. Eren, L. Marot, M. Wisse, et al. In situ evaluation of the reflectivity of molybdenum and rhodium coatings in an ITER-like mixed environment. *Journal of Nuclear Materials*, 438, Supplement(0):S852–S855, 2013.

[119] V.S. Voitsenya, A.F. Bardamid, V.N. Bondarenko, et al. Some problems arising due to plasma-surface interaction for operation of the in-vessel mirrors in a fusion reactor. *Journal of Nuclear Materials*, 290-293(0):336–340, 2001.

[120] B. Eren and L. Marot. Private communication, 2013.

[121] L. Marot, D. Mathys, G. De Temmerman, and P. Oelhafen. Characterization of sub-stoichiometric rhodium oxide deposited by magnetron sputtering. *Surface Science*, 602(21):3375–3380, 2008.

[122] L. Marot, R. Steiner, G. De Temmerman, and P. Oelhafen. Reactivity of rhodium during co-deposition of rhodium and carbon. *Journal of Nuclear Materials*, 390-391(0):1135–1137, 2009.

[123] M. Matveeva, A. Litnovsky, L. Marot, et al. Mirrors for ITER diagnostics: new R&D developments, assessment of the mirror lifetime and impact of the mirror failure on ITER performance. 37th EPS Conference on Plasma Physics, Dublin, Ireland, 21-25 June 2010, P2.105.

[124] J.D. Jackson. *Classical electrodynamics*. Wiley, 1975.

[125] E. Vesselli, M. Campaniello, A. Baraldi, et al. A Surface Core Level Shift Study of Hydrogen-Induced Ordered Structures on Rh(110). *The Journal of Physical Chemistry C*, 112(37):14475–14480, 2008.

[126] D. Mei, V.M. Lebarbier, R. Rousseau, et al. Comparative Investigation of Benzene Steam Reforming over Spinel Supported Rh and Ir Catalysts. *ACS Catalysis*, 3(6):1133–1143, 2013.

[127] A. Zani, D. Dellasega, V. Russo, and M. Passoni. Ultra-low density carbon foams produced by pulsed laser deposition. *Carbon*, 56(0):358–365, 2013.

[128] P. Batistoni, D. Barbier, and J. Likonen. Fusion technology activities at JET in support of the ITER program. *Fusion Engineering and Design*, 88(6-8):733–737, 2013.

[129] J.P. Coad, S. Gruenhagen, D.E. Hole, et al. Overview of JET post-mortem results following the 2007-9 operational period, and comparisons with previous campaigns. *Physica Scripta*, 2011(T145):014003–014008, 2011.

[130] A. Widdowson, C.F. Ayres, S. Booth, et al. Comparison of JET main chamber erosion with dust collected in the divertor. *Journal of Nuclear Materials*, 438, Supplement(0):S827–S832, 2013.

[131] K. Heinola, C.F. Ayres, A. Baron-Wiechec, et al. Tile profiling analysis of samples from JET ITER-like wall and carbon wall. *Physica Scripta*, 2014. Accepted.

[132] J.M. Lackner, W. Waldhauser, and R. Ebner. Large-area high-rate pulsed laser deposition of smooth TiC_xN_{1-x} coatings at room temperature-mechanical and tribological properties. *Surface and Coatings Technology*, 188-189(0):519–524, 2004.

[133] L. Marot, G. De Temmerman, R.P. Doerner, et al. Synergistic effects of hydrogen plasma exposure, pulsed laser heating and temperature on rhodium surfaces. *Journal of Nuclear Materials*, 432(1-3):388–394, 2013.

[134] D.V. Orlinski, V.S. Voitsenya, and K.YU. Vukolov. First mirrors for diagnostic systems of an experimental fusion reactor I. Simulation mirror tests under neutron and ion bombardment. *Plasma Devices and Operations*, 15(1):33–75, 2007.

[135] A. Rothen. The Ellipsometer, an Apparatus to Measure Thicknesses of Thin Surface Films. *Review of Scientific Instruments*, 16(2):26–30, 1945.

[136] R.M.A. Azzam and N.M. Bashara. *Ellipsometry and polarized light*. North-Holland personal library. North-Holland Pub. Co., 1977.

[137] B. Cappella and G. Dietler. Force-distance curves by atomic force microscopy. *Surface Science Reports*, 34(1-3):1–104, 1999.

[138] N.W. Ashcroft and N.D. Mermin. *Solid state physics*. Science: Physics. Saunders College, 1976.

[139] J.F. Watts and J. Wolstenholme. *An Introduction to Surface Analysis by XPS and AES*. Wiley, 2003.

[140] S. Amoruso, B. Toftmann, and J. Schou. Thermalization of a UV laser ablation plume in a background gas: From a directed to a diffusionlike flow. *Physical Review E - Statistical, Nonlinear, and Soft Matter Physics*, 69(5 1):056403–056408, 2004.